Rotational Quantum Superposition Tests

Der Fakultät für Physik der Universität Duisburg-Essen
vorgelegte Dissertation

von

Birthe Schrinski, geb. Papendell
aus
Düsseldorf

zum Erwerb des
Doktors der Naturwissenschafen (Dr. rer. nat.)

Duisburg, den 21. Dezember 2022

Datum der Disputation: 28. April 2023
Erstgutachter: Prof. Dr. Klaus Hornberger, Universität Duisburg-Essen
Zweitgutachter: Prof. Dr. Hendrik Ulbricht, University of Southampton

Zusammenfassung

In dieser Arbeit untersuche ich die quantenmechanische Rotationbewegung von symmetrischen Nanorotoren und insbesondere wie die Nichtlinearität der Dynamik für Quantenexperimente in den Orientierungsfreiheitsgraden verwendet werden kann. In Abwesenheit äußerer Drehmomente führt die Quantisierung des Drehimpulses zu bestimmten Zeiten, ganzzahligen Vielfachen einer Quantenrevivalzeit, zu einer vollständigen Wiederkehr des Anfangszustandes. Im ersten Teil der Arbeit schlage ich ein experimentelles Schema vor, mit dem diese Revivals für Nanoteilchen beobachtet werden können. Am Beispiel von Kohlenstoffnanoröhren und Silikonstäbchen diskutiere ich die Realisierbarkeit eines solchen Experiments und das erwartete Revivalsignal an Hand von numerischen und semiklassischen Methoden. Im Anschluss wird die Auswirkung eines permanenten Drehmoments auf das Revivalsignal für planare und lineare Rotoren mit Hilfe von Störungstheorie und semiklassischen Näherungen untersucht, da eine exakte numerische Berechnung der Rotationsdynamik hier an ihre Grenzen stößt. Im letzen Teil stehen Interferenzeffekte zu Bruchteilen der Revivalzeit im Fokus. Das kurzzeitige Auftauchen von lokalisierten Superpositionszuständen ermöglicht eine interferometrische Kontrolle des Rotationszustandes durch kurze schwache Laserpulse.

Abstract

In this work, I study the quantum rotational motion of symmetric nanorotors and in particular how the non-linearity of the dynamics can be exploited for quantum experiments with orientational degrees of freedom. In absence of external torques the quantization of the angular momentum leads to a complete reappearance of the initial state at integer multiples of a quantum revival time. In the first part of the thesis, I propose an experimental scheme to observe these revivals for nanoparticles. Taking carbon nanotubes and silicone nanorods as examples, I discuss the experimental requirements for this set up and use numerical as well as semiclassical methods to simulate the expected revival signal. Subsequently, the effect of a permanent torque on the revival signal is investigated for planar and linear rotors using perturbation theory and semiclassical approximations, since an exact numerical calculation of the rotational dynamics becomes intractable. The last part focuses on interference effects at fractions of the revival time. The brief emergence of well-localized superposition states allows for an interferometric control of the rotational state by short weak laser pulses.

Publications

1. B. Papendell, B. A. Stickler, and K. Hornberger, *Quantum Angular Momentum Diffusion of Rigid Bodies*, New. J. Phys. **20**, 122001 (2017)
2. B. A. Stickler, B. Papendell, S. Kuhn, B. Schrinski, J. Millen, M. Arndt, and K. Hornberger, *Probing Macroscopic Quantum Superpositions with Nanorotors*, New J. Phys. **20**, 122001 (2018)
3. B. Schrinski, B. A. Stickler, and K. Hornberger, *Interferometric Control of Nanorotor Alignment*, Phys. Rev. A **105**, L021502 (2022)
4. B. Schrinski, Y. J. Chan, and B. Schrinski, *Thermalization of the Quantum Planar Rotor with external potential*, arXiv preprint arXiv:2207.04810

Contents

1. Introduction

While quantum theory is fundamental for our understanding of microscopic systems like atoms or molecules, its predictions and consequences differ from classical mechanics and observations in our macroscopic everyday life. One of these consequences is the wave nature of matter and with this the superposition principle, which follows directly from the linear nature of Schrödinger's equation, $i\hbar\partial_t|\psi\rangle = \mathsf{H}|\psi\rangle$. As time progresses a quantum state, represented by the wave function $|\psi\rangle$, accumulates an energy depending complex phase. In a superposition of coherent wave functions this accumulated phase leads to constructive or destructive interference. This phenomenon is well known in classical physics for electromagnetic and mechanical waves.

Since the birth of quantum mechanics in the 1920s the superposition principle is the focus of numerous experiments for the validation of quantum theory on more and more macroscopic scales. The wave nature of matter particles was experimentally confirmed by the observation of interference pattern due to diffraction of electrons [1,2] and neutrons [3] at the surface of crystals in the 1920s until 1930s. In 1960 an analogue to Young's double slit experiment for light was implemented successfully for electrons. From this time onward interferometric matter-wave experiments were done with objects much larger than microscopic electrons and neutrons, starting with single atoms [4–6] large molecules like fullerenes [7,8], organic molecules with a mass up to 10^4 amu [9] and a current record with molecules with masses beyond 2.5×10^5 amu including up to 2000 atoms [10].

All these experiments address the question whether quantum mechanics is valid on all scales or whether it breaks down at a certain boundary between quantum mechanical and macroscopic world for example beyond a certain mass, length or time scale [11] as it is predicted by models of wave-function collapse [12]. There are different proposals for interference experiments with massive nanometer-sized particles with masses beyond 10^6 amu [13,14] to push this boundary forward to and test the superposition principle on more macroscopic scales.

For such high masses the preparation of quantum states and in particular quantum superposition states is challenging due to decoherence effects. This refers to the loss or destruction of quantum coherence, which is indispensable for interferences, due to the interaction with the environment. Thus, the experimental set up in both proposals mentionend above [13, 14] is based on techniques from levitated quantum optomechanics to reduce the interaction with the environment. The nanospheres are optically trapped and laser cooled using feedback [15] or cavity cooling [16]. Then the trapping laser is turned off and after a period of free fall an optical grating prepares the spatial superposition. Subsequent to a second period of free fall the measurement of the center of mass leads to an interference pattern. While in [13] the spatial superposition is created by postselection after a homodyne measurement of the squared position operator in Ref. [14] the superposition is prepared by diffraction off a standing laser wave.

All these experiments for testing spatial superpositions have in common that they need gratings and with this nonlinear interactions to prepare superposition states. In contrast to that, the non-linearity and anharmonicity of the free rotational dynamics provides quantum effects [17, 18] that have no analogue in the free center of mass motion. Additionally, there are quantum effects of the rotational quantum dynamics like the Einsten-de Haas [19] or the Barnett [20] effect, which are based on the relation between the mechanical angular momentum and magnetization or intrinsic spin.

The quantum persistent tennis racket effect [18] is a quantum effect of the free rotational dynamics of asymmetric rotors. For linear rigid rotors one observes rotational quantum revivals [17]. An arbitrary initial linear rigid rotor state evolves freely and at integer multiples of a revival time T_{rev} the collective interference of all occupied angular momentum states leads to a periodic reappearance of the initial state. This effect is a direct consequence of the quantization of angular momentum. At the revival time the dynamically accumulated phase is an integer multiple of 2π for every single occupied angular momentum state. Thus, an initially tightly aligned rotor disperses and at the revival time the initial alignment recurs. Orientational revivals have been successfully observed in the rotational dynamics of molecules [21–24]. These quantum effects of the free rotational dynamics make the orientational degrees of freedom interesting for quantum tests with massive nanoscale particles.

In the recent years there was strong progress in levitated optomechanics with aspherical and anisotropic particles. One can optically control the alignment of a nanoparticle and manipulate its rotational motion [25–29]. The prospect of rotranslational cavity cooling [30], feedback-cooling [31], and 6D-cooling of nanorotors by elliptic coherent scattering [32, 33] as well as first experimental demonstrations of rotational cooling [34–36] and groundstate cooling of the center of mass motion [37–39] make levitated optomechanics with aspherical particles promising for rotational quantum tests.

Further, in the last years there was a large progress in describing the effect of the environment on the classical [40] and quantum rotational dynamics of nanoscale particles. The interaction with the environment leads to orientational decoherence [41, 42], angular momentum diffusion [43] and friction [44]. Accounting for these effects is crucial for the understanding and interpretation of experimental results.

The main focus of the present thesis are interference schemes for probing rotational quantum effects based on angular momentum quantization of massive nanoscale particles and their applications. For the quantitative description and discussion of these schemes exact numerical methods becomes intractable because of the large number of involved angular momentum eigenstates. Thus, a second focus is the development and application of semiclassical methods which preserve the quantum effect under investigation.

I propose to test the superposition principle by probing orientational quantum revivals of nanoscale rigid rotors [45]. My numerical simulations show that these revivals can be observed for sub-Kelvin temperatures and under realistic experimental conditions taking all relevant sources of environmental orientational decoherence [41–43] into account. This set up is independent of the center of mass temperature but requires cavity- or feedback-cooling of the rotational motion. The proposed experiment provides a new kind of superposition test with massive particles, and the observation of orientational quantum revivals would be the first experimental evidence of angular momentum quantization of massive particles. This interference scheme does not need a diffraction grating and requires only a single recyclable nanorotor. The orientational quantum revivals of nanoscale particles are very sensitive to external torques and are therefore promising candidates for ultra-sensitive gyroscopic torque sensors.

The existence of orientational quantum revivals, and in particular the emergence of orientational superpositions states at fractional revival times, open the door for an interferometric control of the nanorotor alignment. The coherent control of rotational dynamics has been proposed for planar rotations of trapped Bose-Einstein condensates [46] and planar and linear rotations of molecules [47]. Here, in my thesis I propose a Mach-Zehnder-type interference scheme to control the 3D-nanorotor alignment of symmetric rotors at certain times, for example at the revival time. The scheme exploits the emergence of a superposition of four orientational states at an eighth of the revival time. At this point in time, one can steer the alignment by imprinting a relative phase between these well-localized wave packets with a weak, short laser pulse. I show that the control is feasible for realistic symmetric nanorotors in a realistic experimental environment.

The thesis is structured as follows. In **chapter 2** I give a short summary of the most important concepts of classical and quantum mechanical rigid rotor dynamics, on which I rely subsequently. I start by introducing the Euler angles as a parametrization for the orientation of a rigid body. This is followed by a description of the rotational motion with Lagrange's and Hamilton's formalism. Based on these classical concepts and on the quantization of Euler angles and the corresponding canonical momenta, I present the rotational quantum dynamics in Hilbert space. The Hamiltonian can be expressed in terms of the angular momentum operator whose eigenbasis which will be frequently used in the main part of this thesis. In the end, I give a short introduction into the Wigner-Weyl formalism for planar rotations.

Chapter 3 gives the background for the description of decoherence. It begins with a brief introduction of open quantum systems and Lindbald master equations in general, followed by the description of orientational decoherence and angular momentum diffusion. The derivation of an orientational decoherence Lindblad master equation [41, 42] is presented and the diffusion limit [43] is drawn. We encounter the angular momentum diffusion master equation for asymmetric, linear and planar rotations. The diffusion master equation for a linear rigid rotor is the basis for estimating orientational decoherence in the proposed experiment in chapter 6. Finally, I illustrate angular momentum diffusion with the example of planar rotations.

After these two chapters providing mainly theoretical background I present in **chapter 4** an experimentally viable scheme for testing rotational quantum revivals with nanoparticles. I discuss the important steps of the interference scheme and introduce semiclassical methods for the calculation of the initial state. The feasibility of the set up is shown and discussed for realistic nanoparticles based on numerical simulations. In **chapter 5** the focus is on the effect of a constant external torque on the rotational dynamics. Starting with planar rotations I use the WKB method for the calculations, while for linear rotations I employ the EBK method for two dimensional motions. Finally, I use perturbation theory to estimate the effect of external torques on the experimental set up from chapter 4.

In **chapter 6** I show how to control the alignment of a nanoparticle by applying a short lase pulse at the fractional revival time $T_{\mathrm{rev}}/8$. For the explanation of the interference scheme I start with a semiclassical description of the free rotational dynamics, which gives a better understanding of the quantum states at fractional revival times and motivates a simplified eight state model. Later on, deviations from a perfect initial state and the ideal time evolution are discussed, including environmental decoherence and slight asymmetries of the nanorotor. In the end, I propose a realistic experimental set up for steering symmetric rotors.

2. Theory of the Rigid Rotor

Examining rotational quantum effects of aspherical nanoscale particles and how to exploit them for interferometric experiments we may neglect the vibrational degrees of freedom. Then we can treat the particle as a rigid rotor with three translational degrees of freedom for the center of mass motion and three rotational degrees of freedom for parametrizing rotations around the center of mass.

In the following, I give a short review of the rotational dynamics of rigid rotors. I start with the classical description, where I introduce the basic concepts of the rotational motion, which includes the Euler angle parametrization for rotations and Lagrange's and Hamilton's formalism for rotational dynamics.

Based on the classical theory of the rotational motion, I introduce a quantum description in Hilbert space by quantizing the Euler angles and the corresponding canonical momenta. After formulating the Hamiltonian in terms of the angular momentum operator I present the angular momentum eigenbasis. In the end, we see how to handle the one-dimensional rotational quantum motion of planar rotors in phase space by using the Wigner-Weyl formalism.

2.1. The Classical Rigid Rotor

In the following, I will give a short description of the classical rigid rotor as far as needed subsequently. The presentation is mainly based on the textbooks [48, 49] and the monograph [50].

Euler Angles

The direction of the body-fixed system $\{\mathbf{n}_1, \mathbf{n}_2, \mathbf{n}_3\}$ of orthonormal basis vectors of a rigid rotor in relation to a space-fixed system $\{\mathbf{e}_1, \mathbf{e}_2, \mathbf{e}_3\}$ defines the orientation of the rotor. We can parametrize a rotation around the center of mass, and with this the orientation of a body in space, unambiguously by means of Euler angles $\Omega = (\alpha, \beta, \gamma)$ with the range $\alpha, \gamma \in [0, 2\pi)$ and $\beta \in [0, \pi]$ which serve to decompose the rotation into a sequence of three consecutive rotations (see Fig. 2.1).

Here, and throughout this thesis, I use the z-y'-z'' convention: We begin with a rotation by the angle α about the space-fixed $\mathbf{e}_3$-axis, followed by a rotation

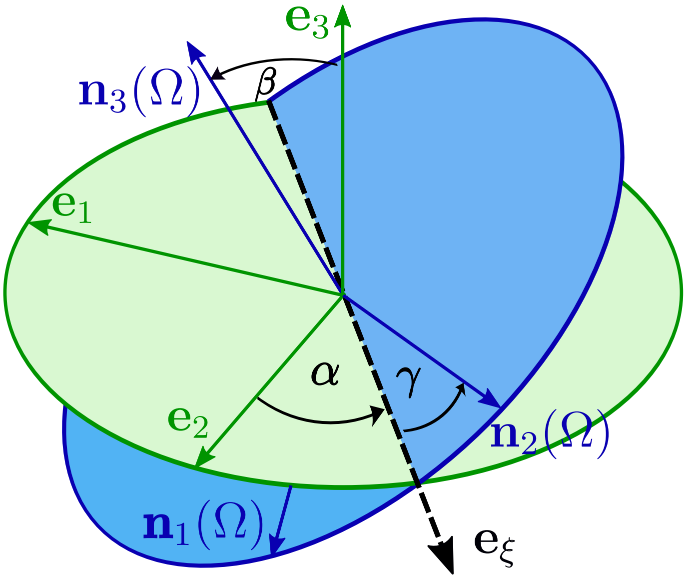

Figure 2.1.: Illustration of the Euler angles in the z-y'-z'' convention. The green axes belong to the space-fixed frame and the blue axes to the body-fixed system. The black axis is the nodal line.

by the angle β about the temporarily y'-axis. This axis points along the intersection of the space- and body-fixed (x, y)-plane which is called the nodal line $\mathbf{e}_\xi = \mathbf{e}_3 \times \mathbf{n}_3 / |\mathbf{e}_3 \times \mathbf{n}_3| = (-\sin\alpha, \cos\alpha, 0)$. We finish with a rotation about the new z''-axis, the body-fixed $\mathbf{n}_3$-axis. We thus obtain the rotation tensor $\mathsf{R}(\Omega)$ for the total rotation

$$\mathsf{R}(\Omega) = \mathsf{R}_{\mathbf{n}_3}(\gamma)\mathsf{R}_{\mathbf{e}_\xi}(\beta)\mathsf{R}_{\mathbf{e}_3}(\alpha). \tag{2.1}$$

We can express the rotation about the body-fixed $\mathbf{n}_3$-axis through rotations around the space-fixed $\mathbf{e}_3$-axis and the nodal line $\mathbf{e}_\xi$, and similarly the rotation about the $\mathbf{e}_\xi$-axis through rotations about only space-fixed axes. With this the rotation matrix (2.1) can be rewritten in terms of rotations only about space-fixed axes [51],

$$\begin{aligned}\mathsf{R}(\Omega) &= \mathsf{R}_{\mathbf{e}_3}(\alpha)\mathsf{R}_{\mathbf{e}_2}(\beta)\mathsf{R}_{\mathbf{e}_3}(\gamma)\\ &= \begin{pmatrix}\cos\alpha & -\sin\alpha & 0\\ \sin\alpha & \cos\alpha & 0\\ 0 & 0 & 1\end{pmatrix}\begin{pmatrix}\cos\beta & 0 & \sin\beta\\ 0 & 1 & 0\\ -\sin\beta & 0 & \cos\beta\end{pmatrix}\begin{pmatrix}\cos\gamma & -\sin\gamma & 0\\ \sin\gamma & \cos\gamma & 0\\ 0 & 0 & 1\end{pmatrix}.\end{aligned} \tag{2.2}$$

Hamilton's Formalism for the Rigid Rotor

Based on the definition of the orientation of a rigid rotor, and in particular on the parametrization by Euler angles $\Omega = (\alpha, \beta, \gamma)$, we want to describe the rotational dynamics of the rotor by using the Hamilton formalism. The Euler angles act as our canonical coordinates, they form together with the corresponding canonical conjugate momenta $p_\Omega = (p_\alpha, p_\beta, p_\gamma)$ the classical phase space of the rigid rotor.

For the derivation of the canonically conjugate momenta we go one step back and start with the Lagrangian formalism for the rotational motion. For the free rotational dynamics of a rigid rotor the Lagrangian contains only the rotational energy

$$T_{\text{rot}} = \frac{1}{2}\sum_{i=1}^{3} I_i \tilde{\omega}_i^2, \tag{2.3}$$

with principle moments of inertia I_i and $\tilde{\omega}_i$ the angular velocity components in the body-fixed frame. Here and in the following, the tilde denotes quantities in relation to the body-fixed frame. The angular velocities can be expressed in terms of the Euler angles and their time derivatives [50]

$$\tilde{\omega}_1 = \dot{\beta}\sin\gamma - \dot{\alpha}\sin\beta\cos\gamma, \tag{2.4a}$$

$$\tilde{\omega}_2 = \dot{\beta}\cos\gamma + \dot{\alpha}\sin\beta\sin\gamma, \tag{2.4b}$$

$$\tilde{\omega}_3 = \dot{\alpha}\cos\beta + \dot{\gamma}. \tag{2.4c}$$

Inserting (2.4) in the expression (2.3) leads to the Lagrangian $\mathcal{L}\left(\Omega, \dot{\Omega}\right)$ with $\dot{\Omega} = \left(\dot{\alpha}, \dot{\beta}, \dot{\gamma}\right)$,

$$\begin{aligned}\mathcal{L}(\Omega, \dot{\Omega}) =& \frac{1}{2}\Big[\dot{\alpha}^2\left(I_1\sin^2\beta\cos^2\gamma + I_2\sin^2\beta\sin^2\gamma + I_3\cos^2\beta\right) + \dot{\gamma}^2 I_3 \\ &+ \dot{\beta}^2\left(I_1\sin^2\gamma + I_2\cos^2\gamma\right) + 2\dot{\alpha}\dot{\gamma}I_3\cos\beta \\ &+ 2\dot{\alpha}\dot{\beta}(I_2 - I_1)\sin\beta\sin\gamma\cos\gamma\Big].\end{aligned} \tag{2.5}$$

With the Lagrangian (2.5) we can calculate the canonical momenta $p_\alpha = \partial_{\dot{\alpha}}\mathcal{L}(\Omega, \dot{\Omega})$

$$\begin{aligned}p_\alpha =& \dot{\alpha}\left(I_1\sin^2\beta\cos^2\gamma + I_2\sin^2\beta\sin^2\gamma + I_3\cos^2\beta\right) + \dot{\gamma}I_3\cos\beta \\ &+ \dot{\beta}(I_2 - I_1)\sin\beta\sin\gamma\cos\gamma = \mathbf{J}\cdot\mathbf{e}_3,\end{aligned} \tag{2.6a}$$

$$p_\beta = \dot{\alpha}(I_2 - I_1)\sin\beta\sin\gamma\cos\gamma + \dot{\beta}(I_1\sin^2\gamma + I_2\cos^2\gamma) = \mathbf{J}\cdot\mathbf{e}_\xi, \tag{2.6b}$$

$$p_\gamma = I_3(\dot{\alpha}\cos\beta + \dot{\gamma}) = \mathbf{J}\cdot\mathbf{n}_3. \tag{2.6c}$$

As shown by the second equalities the canonical momenta are projections of the angular momentum vector $\mathbf{J}$ on the corresponding rotation axis. From the equations (2.6), combined with the equations (2.4), following expressions for the components of the angular momentum vector in the space-fixed frame (J_1, J_2, J_3) are obtained [48]

$$\begin{aligned} J_1 =& -\cos\alpha\cot\beta\, p_\alpha - \sin\alpha p_\beta + \frac{\cos\alpha}{\sin\beta} p_\gamma, && \text{(2.7a)} \\ J_2 =& -\sin\alpha\cot\beta\, p_\alpha + \cos\alpha p_\beta + \frac{\sin\alpha}{\sin\beta} p_\gamma, && \text{(2.7b)} \\ J_3 =& p_\alpha, && \text{(2.7c)} \end{aligned}$$

while the components $(\tilde{J}_1, \tilde{J}_2, \tilde{J}_3)$ in the body-fixed frame read

$$\begin{aligned} \tilde{J}_1 &= -\frac{\cos\gamma}{\sin\beta} p_\alpha + \sin\gamma\, p_\beta + \cot\beta\cos\gamma\, p_\gamma, && \text{(2.8a)} \\ \tilde{J}_2 &= \frac{\sin\gamma}{\sin\beta} p_\alpha + \cos\gamma\, p_\beta - \cot\beta\sin\gamma\, p_\gamma, && \text{(2.8b)} \\ \tilde{J}_3 &= p_\gamma. && \text{(2.8c)} \end{aligned}$$

We can express the rotational energy in terms of the components in the body-fixed system [48], $T = (\tilde{J}_1^2/2I_1 + \tilde{J}_2^2/2I_2 + \tilde{J}_3^2/2I_3)$, and thus obtain the Hamiltonian function

$$\begin{aligned} H(\Omega, p_\Omega) =& \frac{1}{2I_1\sin^2\beta}\left[(p_\alpha - p_\gamma\cos\beta)\cos\gamma - p_\beta\sin\beta\sin\gamma\right]^2 \\ &+ \frac{1}{2I_2\sin^2\beta}\left[(p_\alpha - p_\gamma\cos\beta)\sin\gamma + p_\beta\sin\beta\cos\gamma\right]^2 \\ &+ \frac{p_\gamma^2}{2I_3}. \end{aligned} \tag{2.9}$$

This Hamiltonian function simplifies for a symmetric rigid rotor with moments of inertia $I_1 = I_2 = I$ and I_3 to

$$H_\mathrm{S}(\Omega, p_\Omega) = \frac{1}{2I}\left[\frac{p_\alpha^2}{\sin^2\beta} + p_\beta^2 + \left(\cot^2\beta + \frac{I}{I_3}\right)p_\gamma^2 - \frac{2\cot\beta}{\sin\beta}p_\alpha p_\gamma\right]. \tag{2.10}$$

For a linear rigid rotor the moment of inertia I_3 vanishes. Rotations about the symmetry axis $\mathbf{n}_3$ are prohibited and γ is not a dynamic variable anymore. The Hamiltonian function $H_\mathrm{L}(\Omega, p_\Omega)$ of the linear rigid rotor follows from the one of a symmetric top (2.10), by setting $\gamma = 0$ and $p_\gamma = 0$,

$$H_\mathrm{L}(\Omega, p_\Omega) = \frac{1}{2I}\left(\frac{p_\alpha^2}{\sin^2\beta} + p_\beta^2\right). \tag{2.11}$$

The Hamiltonian function determines the time evolution of the system via Hamilton's equations. Further, the classical Hamilton formalism serves as a starting point for a quantum mechanical treatment.

2.2. The Quantum Rigid Rotor

In the following section, I give a short review of the quantum rotational dynamics of the rigid rotor on the basis of the monographs [50, 52].

Based on the classical description of the rotational dynamics with Euler angles and canonical momenta we introduce corresponding angle and canonical momentum operators in the quantum mechanical case. Throughout this thesis, I use sans-serif latin or bold greek letters to denote operators. We will see that one difficulty in quantizing the Euler angles and canonical momenta lies in the curved configuration space. Following De Witt's quantization rules [53, 54], I begin with an introduction of the angle operators and their eigenstates and later introduce the canonical momentum operators.
The angle operators $(\boldsymbol{\alpha}, \boldsymbol{\beta}, \boldsymbol{\gamma})$ have a continuous spectrum of eigenvalues and the improper eigenstates $|\Omega\rangle \equiv |\alpha, \beta, \gamma\rangle$. These eigenstates form a complete basis [50]

$$\int_0^{2\pi} \mathrm{d}\alpha \int_0^{\pi} \mathrm{d}\beta \, \sin\beta \int_0^{2\pi} \mathrm{d}\gamma \, |\alpha, \beta, \gamma\rangle\langle\alpha, \beta, \gamma| = \mathbb{1}. \tag{2.12}$$

This way every quantum state $|\psi\rangle$ can be expanded in the angle eigenstates

$$|\psi\rangle = \int_0^{2\pi} \mathrm{d}\alpha \int_0^{\pi} \mathrm{d}\beta \, \sin\beta \int_0^{2\pi} \mathrm{d}\gamma \, |\alpha, \beta, \gamma\rangle\langle\alpha, \beta, \gamma|\psi\rangle. \tag{2.13}$$

The factor $\sin\beta$ is here the square root of the determinant of the metric tensor [53,54]

$$g(\Omega) = \sin^2\beta \tag{2.14}$$

of the curved coordinate system. Further, these eigenstates satisfy the orthogonal relation [53, 54]

$$\langle\Omega|\,\Omega'\rangle = \frac{\delta_{2\pi}(\alpha - \alpha')\delta_{\pi}(\beta - \beta')\delta_{2\pi}(\gamma - \gamma')}{\sin\beta}, \tag{2.15}$$

with the φ-periodic delta-distributions $\delta_\varphi(\alpha) = \delta(\alpha \bmod \varphi)$.

Canonical Momentum Operators

To quantize the canonical momenta we use the formula of DeWitt involving the determinant of the metric tensor $g(\Omega)$ [53, 54]

$$p_\lambda \to \mathsf{p}_\lambda = -i\hbar\left(\frac{\partial}{\partial\lambda} + \frac{1}{4}\frac{\partial \ln g(\Omega)}{\partial\lambda}\right), \tag{2.16}$$

with $\lambda = \{\alpha, \beta, \gamma\}$. By inserting the determinant of the metric tensor (2.14) in the quantization (2.16) we obtain the conjugate canonical momentum operators to the Euler angles in the Euler angle representation

$$\mathsf{p}_\alpha = -i\hbar\frac{\partial}{\partial\alpha}, \tag{2.17a}$$

$$\mathsf{p}_\beta = -i\hbar\left(\frac{\partial}{\partial\beta} + \frac{1}{2}\cot \upbeta\right), \tag{2.17b}$$

$$\mathsf{p}_\gamma = -i\hbar\frac{\partial}{\partial\gamma}. \tag{2.17c}$$

The eigenfunctions of the canonical momentum operators (2.17) are given by [50]

$$\langle\Omega|m_\Omega\rangle = \frac{e^{im_\alpha\alpha}}{\sqrt{2\pi}}\frac{e^{i2m_\beta\beta}}{\sqrt{\pi\sin\beta}}\frac{e^{im_\gamma\gamma}}{\sqrt{2\pi}}. \tag{2.18}$$

The corresponding eigenvalues $m_\Omega = (m_\alpha, m_\beta, m_\gamma) \in \mathbb{Z}^3$ with [50]

$$\mathsf{p}_\alpha|m_\Omega\rangle = \hbar m_\alpha|m_\Omega\rangle, \tag{2.19a}$$

$$\mathsf{p}_\beta|m_\Omega\rangle = 2\hbar m_\beta|m_\Omega\rangle, \tag{2.19b}$$

$$\mathsf{p}_\gamma|m_\Omega\rangle = \hbar m_\gamma|m_\Omega\rangle, \tag{2.19c}$$

are discrete due to the single-valuedness of the wave function in the compact configuration space.

Angular Momentum Operator

In the following, the angular momentum representation of operators will be frequently used. I therefore introduce now the angular momentum operator in terms of its components in the body- and space-fixed frame, and the eigenstates of the free-flight Hamiltonian.

To obtain components of the angular momentum operator one inserts the angle operators $(\upalpha, \upbeta, \upgamma)$ and the canonical momentum operators $(\mathsf{p}_\alpha, \mathsf{p}_\beta, \mathsf{p}_\gamma)$ into the expressions of the classical angular momentum components in (2.8) and (2.7) and takes the Weyl-ordering for angular and momentum operators [52] into account. From this follow the components of the angular momentum operator in the space-fixed system $(\mathsf{J}_1, \mathsf{J}_2, \mathsf{J}_3)$ [52]

$$\mathsf{J}_1 = -\left(\frac{\cot \beta}{2} \{\mathsf{p}_\alpha, \cos \alpha\} + \sin \alpha \, \mathsf{p}_\beta - \frac{\cos \alpha}{\sin \beta} \mathsf{p}_\gamma \right), \tag{2.20a}$$

$$\mathsf{J}_2 = -\left(\frac{\cot \beta}{2} \{\mathsf{p}_\alpha, \sin \alpha\} - \cos \alpha \, \mathsf{p}_\beta - \frac{\sin \alpha}{\sin \beta} \mathsf{p}_\gamma \right), \tag{2.20b}$$

$$\mathsf{J}_3 = \mathsf{p}_\alpha. \tag{2.20c}$$

We see that the J_3-component is identical to the p_α operator, which we can expect from the classical equations, where we have seen that the canonical momentum p_α is the projection onto the space-fixed $\mathbf{e}_3$-axis. The components $\tilde{\mathsf{J}}_1, \tilde{\mathsf{J}}_2, \tilde{\mathsf{J}}_3$ in the body-fixed frame read [52]

$$\tilde{\mathsf{J}}_1 = i\hbar \left(\frac{\cos \gamma}{\sin \beta} \frac{\partial}{\partial \alpha} - \sin \gamma \frac{\partial}{\partial \beta} - \cos \gamma \cot \beta \frac{\partial}{\partial \gamma} \right), \tag{2.21a}$$

$$\tilde{\mathsf{J}}_2 = i\hbar \left(-\frac{\sin \gamma}{\sin \beta} \frac{\partial}{\partial \alpha} - \cos \gamma \frac{\partial}{\partial \beta} + \sin \gamma \cot \beta \frac{\partial}{\partial \gamma} \right), \tag{2.21b}$$

$$\tilde{\mathsf{J}}_3 = -i\hbar \frac{\partial}{\partial \gamma}. \tag{2.21c}$$

Similar to the space-fixed components, the body-fixed $\tilde{\mathsf{J}}_3$ component is the p_γ operator, as one may expect since it describes rotations around the body-fixed $\mathbf{n}_3$-axis.

The space-fixed components J_i obey the commutator relations $[\mathsf{J}_i, \mathsf{J}_j] = i\hbar\epsilon_{ijk}\mathsf{J}_k$ [50], which are identical with the commutator relations for the orbital angular momentum operator of a point-like particle. In contrast, the body-fixed components fulfill the relations $\left[\tilde{\mathsf{J}}_i, \tilde{\mathsf{J}}_j\right] = -i\hbar\epsilon_{ijk}\tilde{\mathsf{J}}_k$. Further, all components commute with the squared angular momentum vector [52], $[\mathsf{J}^2, \mathsf{J}_i] = 0$ and $\left[\tilde{\mathsf{J}}^2, \tilde{\mathsf{J}}_i\right] = 0$. Note that the squared angular momentum J^2 is invariant under rotations of the reference frame and $\mathsf{J}^2 = \tilde{\mathsf{J}}^2$. Choosing J^2, J_3 and $\tilde{\mathsf{J}}_3$, we have a complete set of mutually commuting operators with simultaneous eigenstates $|jmk\rangle$. Here, $j \in \mathbb{N}_0$ is the corresponding quantum number to the squared angular momentum operator J^2, $m \in \{-j, -j+1, ..., j\}$ the quantum number to the projection onto the space-fixed $\mathbf{e}_3$-axis J_3 and $k \in \{-j, -j+1, ..., j\}$ the one corresponding the projection onto the body-fixed $\mathbf{n}_3$-axis $\tilde{\mathsf{J}}_3$. The eigenvalue equations read [50, 52]

$$\mathsf{J}^2|jmk\rangle = \hbar^2 j(j+1)|jmk\rangle, \tag{2.22a}$$

$$\mathsf{J}_3|jmk\rangle = \hbar m|jmk\rangle, \tag{2.22b}$$

$$\tilde{\mathsf{J}}_3|jmk\rangle = \hbar k|jmk\rangle. \tag{2.22c}$$

The eigenstates $|jmk\rangle$ fulfill the orthogonal relation and are complete

$$\langle jmk|j'm'k'\rangle = \delta_{jj'}\delta_{mm'}\delta_{kk'}, \tag{2.23a}$$

$$\sum_{j\in\mathbb{N}_0}\sum_{m=-j}^{j}\sum_{k=-j}^{j}|jmk\rangle\langle jmk| = \mathbb{1}. \tag{2.23b}$$

They provide an orthogonal basis of the rigid rotor Hilbert space.

The Hamiltonian

Analogous to the classical Hamiltonian, we insert the body-fixed components of the angular momentum operator to obtain the free flight Hamiltonian,

$$\mathsf{H} = \frac{\tilde{\mathsf{J}}_1^2}{2I_1} + \frac{\tilde{\mathsf{J}}_2^2}{2I_2} + \frac{\tilde{\mathsf{J}}_3^2}{2I_3}. \tag{2.24}$$

In the general case of an asymmetric rotor with $I_1 \neq I_2 \neq I_3$ it is not possible to derive a simple analytical expression for the energy eigenvalues. But in special cases we can give the eigenstates and eigenvalues.

First, we look at a symmetric rotor, with $I_1 = I_2 = I \neq I_3$. In this case the Hamiltonian (2.24) reduces to [55]

$$\mathsf{H} = \frac{\mathsf{J}^2}{2I} + \frac{1}{2}\left(\frac{1}{I_3} - \frac{1}{I}\right)\tilde{\mathsf{J}}_3^2. \tag{2.25}$$

Depending only on the squared angular momentum operator and its component $\tilde{\mathsf{J}}_3$ in the body-fixed frame the states (2.22) are eigenstates of the Hamiltonian. The corresponding eigenenergies read

$$E_{jk} = \frac{\hbar^2}{2I}j(j+1) + \frac{\hbar^2}{2}\left(\frac{1}{I_3} - \frac{1}{I}\right)k^2. \tag{2.26}$$

They are independent of the projection on the space-fixed $\mathbf{e}_3$-axis, therefore $2j+1$-fold degenerate in the quantum number m. In k they are two-fold degenerate because of the dependence on k^2. So in total we obtain a degeneracy of $2(2j+1)$.

For later calculations with orientation-dependent operators we need the eigenstates $|jmk\rangle$ in the Euler angle representation. This is given by Wigner D-matrices [50],

$$\langle\Omega|jmk\rangle = \sqrt{\frac{2j+1}{8\pi^2}}D_{mk}^{j*}(\Omega) = \sqrt{\frac{2j+1}{8\pi^2}}e^{im\alpha}d_{mk}^{j}(\beta)e^{ik\gamma}. \tag{2.27}$$

The Wigner D-matrices, $D_{mk}^{j}(\Omega) = \langle jm|\mathsf{R}(\Omega)|jk\rangle$, are the matrix elements of the rotation operator $\mathsf{R}(\Omega)$. In the second equality I used (2.2) and introduced Wigner's small d-matrices, given by the matrix elements of the rotation induced by the J_2 operator $\langle jm|e^{-i\beta\mathsf{J}_y}|jk\rangle = d^j_{km}(\beta)$.

As discussed in section 2.1 for the classical top, the limit $I_3 \to 0$ turns the symmetric rotor into the linear rigid rotor. In this limit no rotations around the symmetry axis $\mathbf{n}_3$ occur and γ is no longer a dynamic variable. From this it follows that the quantum number k vanishes and only $k = 0$ is occupied. The state of the linear rotor can thus be described only by two quantum numbers j and m, and the Hamiltonian simplifies to

$$\mathsf{H}_L = \frac{1}{2I}\mathsf{J}^2. \tag{2.28}$$

The eigenstates of the linear rigid rotor Hamiltonian H_L are then given by $|jm\rangle = |jm0\rangle$ with the corresponding energy eigenvalues

$$E_j = \frac{\hbar^2}{2I}j(j+1). \tag{2.29}$$

Since the energy eigenvalues (2.29) are independent of m they are $2j+1$-fold degenerate.

By setting $k = 0$ in the equation (2.27) and using the relation $D^j_{m0} = \sqrt{4\pi/(2j+1)}Y^{m*}_j(\beta,\alpha)$ [52] we can write the eigenstates $|jm\rangle$ of the Hamiltonian (2.28) in the Euler angle representation in terms of spherical harmonics $Y^m_j(\alpha,\beta)$,

$$\langle\alpha,\beta|jm\rangle = \frac{1}{\sqrt{2\pi}}Y^m_j(\beta,\alpha). \tag{2.30}$$

In a third step we can confine the motion to a plane around the space-fixed $\mathbf{e}_3$-axis. This leads to a planar rotor with $\mathsf{J}_1 = \mathsf{J}_2 = 0$ and $\mathsf{J}^2 = \mathsf{J}_3^2$ and the free flight Hamiltonian,

$$\mathsf{H}_{\mathrm{p}} = \frac{\mathsf{J}_3^2}{2I} = \frac{\mathsf{p}_\alpha^2}{2I}. \tag{2.31}$$

Here, we inserted (2.20c) for J_3. The eigenstates $|m\rangle$ of p_α and H_{p} are two-fold degenerate with energy eigenvalues and the Euler angle representation

$$E_m = \frac{\hbar^2 m^2}{2I}, \tag{2.32a}$$

$$\langle\alpha|m\rangle = \frac{1}{\sqrt{2\pi}}e^{im\alpha}. \tag{2.32b}$$

2.3. Wigner-Weyl Formalism for Planar Rotations

In the previous section, we have seen how to work with quantum rotation states in Hilbert space. While this Hilbert space representation is the most common choice to work with in quantum mechanics, we can also present a quantum state as a distribution function in phase space, similar to the classical Hamilton formalism. This representation has some advantages. On the one hand, one works with a formalism well known from classical mechanics and benefits from the intuition in classical terms, but on the other hand it emphasizes the quantum nature of the state.

In the following, I present one possibility to map quantum states and observables to phase space functions. This Wigner-Weyl formalism [56,57], which was originally formulated in flat space, was extended to curved configuration spaces [58, 59] and also to planar rotations [60]. Here, the state operator ρ is mapped to a real quasi probability distribution, the Wigner function $w(\alpha, p_\alpha)$ and operators are represented by Weyl symbols. In contrast to the classical probability distributions, the Wigner function can have negative values. The configuration space of the planar rotor is parametrized by a single angle $\alpha \in [0, 2\pi)$. This angle α forms the phase space together with the corresponding canonical momentum p_α, parametrized by the discrete eigenvalues $m \in \mathbb{Z}$. The Wigner function for a planar rotor state ρ reads in the angular representation [60]

$$W(\alpha, m) = \frac{1}{\pi} \int_{-\pi/2}^{\pi/2} \mathrm{d}\alpha' \, e^{-2im\alpha'} \langle \alpha + \alpha' | \rho | \alpha - \alpha' \rangle. \tag{2.33}$$

The Wigner function (2.33) is 2π-periodic in the angle α and obeys the following requirements of a quasi probability distribution [60]

$$\sum_{m \in \mathbb{Z}} \int_{-\pi}^{\pi} \mathrm{d}\alpha \, W(\alpha, m) = 1, \tag{2.34a}$$

$$\sum_{m \in \mathbb{Z}} W(\alpha, m) = \langle \alpha | \rho | \alpha \rangle, \tag{2.34b}$$

$$\int_{-\pi}^{\pi} \mathrm{d}\alpha \, W(\alpha, m) = \langle m | \rho | m \rangle. \tag{2.34c}$$

Here, in (2.34a) we see the normalization of the Wigner function and in (2.34b) and (2.34c) the marginal distribution for angle and angular momentum of the Wigner function, which are probability density functions and a discrete probability distribution, respectively.

For a complete formulation of quantum mechanics in phase space we have to map an arbitrary operator A on a phase space function, the so-called Weyl symbol $W_A(\alpha, m)$ [60],

$$W_A(\alpha, m) = \int_{-\pi/2}^{\pi/2} \mathrm{d}\alpha'\, e^{-2im\alpha'} \langle \alpha + \alpha' | \mathsf{A} | \alpha - \alpha' \rangle. \tag{2.35}$$

The transformation of an operator in its Weyl symbol is identical to that of the Wigner function apart from the normalization factor.

A Fourier transformation of (2.33) leads to the Wigner function in the momentum representation,

$$\begin{aligned} W(\alpha, m) =& \frac{1}{2\pi} \sum_{m_1 \in \mathbb{Z}} \sum_{m_2 \in \mathbb{Z}} \operatorname{sinc}\left[\left(m - \frac{m_1 + m_2}{2}\right)\pi\right] \\ & \times e^{i(m_1 - m_2)\alpha} \langle m_1 | \rho | m_2 \rangle. \end{aligned} \tag{2.36}$$

This equation can be written in a different form by decomposing the Wigner function into integer and half-integer distributions. This representation has later great advantages when we come to equations of motions for the Wigner function and reads [60, 61]

$$W(\alpha, m) = w_m(\alpha) + \sum_{m'} \operatorname{sinc}\left[\left(m - m' - \frac{1}{2}\right)\pi\right] w_{m+1/2}(\alpha), \tag{2.37}$$

with an auxiliary function definend by

$$w_{m+\mu/2}(\alpha) = \frac{1}{2\pi} \int_{-\pi}^{\pi} \mathrm{d}\alpha'\, e^{-2i\alpha'(m+\mu/2)} \langle \alpha + \alpha' | \rho | \alpha - \alpha' \rangle \tag{2.38}$$

for $\mu \in \{0, 1\}$. The function with integer indices are π-periodic, while the half-integer distributions are 2π-periodic. For this auxiliary function the angular momentum representation reads [60, 61]

$$w_{m+\mu/2}(\alpha) = \frac{1}{2\pi} \sum_{m' \in \mathbb{Z}} e^{-2i(m'+\mu/2)\alpha} \langle m - m' | \rho | m + m' + \mu \rangle. \tag{2.39}$$

It is much easier to handle than the momentum representation (2.36) of the complete Wigner function.

2.4. Semiclassical Description of Rotation Dynamics

The focus of this thesis is the description and examination of rotational quantum dynamics of macroscopic particles with thousands of angular momentum states involved. In this case exact quantum dynamics is not expedient and numerical simulations based on the exact dynamics become intractable while in this limit semiclassical approximation methods are promising. The here presented approximation methods are based on Bohr-Sommerfeld quantized action-angle variables. Thus, I start with an introduction of action-angle variables for the free rotation of linear rotors followed by the WKB approximation for planar and the EBK approximation for linear rotors. In the end, the semiclassical approximation of matrix elements is shown. This section is based on the textbooks [62, 63].

2.4.1. Bohr-Sommerfeld-Quantization

For the here presented approximation methods the classical action integral along a closed path, $I = 1/(2\pi) \oint \mathrm{d}q\, p(q)$, with the canonical variables p and q, plays an important role. Thus, we start with an introduction of the action-angle variables for angular momentum and the quantization of action.

Action-Angle Variables for Angular Momentum

We know from Hamilton-Jacobi mechanics that the canonical transformation into action-angle variable simplifies the resulting Hamiltonian. The new action variables, $I_k = 1/2\pi \oint \mathrm{d}q_k\, p_k$ are constants of motion while the corresponding angles α_k vary linear in time. The generating function for the transformation of the "old" coordinates q_k and canonical momenta p_k into the action-angle variables I_k, α_k is the function $S(\mathbf{q}, \mathbf{I})$ with

$$p_k(q_k, I_k) = \partial S(q_k, I_k)/\partial q_k, \quad \alpha_k(q_k, I_k) = \partial S(q_k, I_k)/\partial I_k. \tag{2.40}$$

For the transformation onto action-angle variable we start with the effective Hamiltonian (2.11), $H_\mathrm{L}(\alpha, \beta, p_\alpha, p_\beta) = \mathbf{J}^2/2I$, and its connection with the angular momentum $\mathbf{J}$. From this follows the corresponding Hamilton-Jacobi equation for the generating function $S(\alpha, \beta, I_\alpha, I_\beta)$

$$J^2 = \left(\frac{\partial S}{\partial \beta}\right)^2 + \frac{1}{\sin\beta}\left(\frac{\partial S}{\partial \alpha}\right)^2. \tag{2.41}$$

The generating function separates in the form $S(\alpha, \beta, I_\alpha, I_\beta) = S_\alpha(\alpha, I_\alpha, I_\beta) + S_\beta(\beta, I_\alpha, I_\beta)$ and with this the Hamilton-Jacobi equation (2.41) separates into [62]

$$p_\alpha = \frac{\partial S}{\partial \alpha} = M, \tag{2.42a}$$

$$p_\beta = \frac{\partial S}{\partial \beta} = \left(J^2 - \frac{M^2}{\sin^2\beta}\right)^{1/2}, \tag{2.42b}$$

with the constant of motion M. The motion in α has no turning points and thus the action I_α reads

$$I_\alpha = \frac{1}{2\pi}\int_0^{2\pi} \mathrm{d}\alpha\, p_\alpha = M. \tag{2.43}$$

The β-motion hast two turning points, $\beta_{\min} = \arcsin(M/J)$ and $\beta_{\max} = \pi - \beta_{\min}$. With this the we obtain [62]

$$I_\beta = \frac{1}{\pi}\int_{\beta_{\min}}^{\pi-\beta_{\min}} \mathrm{d}\beta \left(J^2 - \frac{M^2}{\sin^2\beta}\right)^{1/2} = J - |M|. \tag{2.44}$$

We take the constants of motion J and M as the action variables and from equations (2.40) and (2.42b) follow for the conjugate angulars

$$\alpha_J = \int_{\beta_{\min}}^{\beta} \mathrm{d}\beta' \frac{J\sin\beta'}{(J^2\sin^2\beta' - M^2)^{1/2}} = \arccos\left(\frac{J\cos\beta}{(J^2 - M^2)^{1/2}}\right), \tag{2.45a}$$

$$\begin{aligned}\alpha_M &= \int_{-\pi}^{\alpha} \mathrm{d}\alpha' + \int_{\beta_{\min}}^{\beta} \mathrm{d}\beta' \frac{M}{\sin\beta'(J^2\sin^2\beta - M^2)^{1/2}} \\ &= \alpha + \pi - \arctan\left(\frac{\sqrt{J^2\sin^2\beta - M^2}}{M\cos\beta}\right)\end{aligned}. \tag{2.45b}$$

Bohr-Sommerfeld-Quantisation of angular momentum

A semiclassical method for the quantization of the system is the quantization of the classical actions I_k via the Bohr-Sommerfeld quantization rule

$$I_k = \frac{1}{2\pi}\oint \mathrm{d}q_k\, p_k = \hbar(n + \delta), \tag{2.46}$$

with the quantum number $n \in \mathbb{Z}$ and the Maslov index δ. The Maslov index depends on the number and kind of turning points of the motion, $\delta = \nu_h/2 + \nu_s/4$. Here, ν_h is the number of "hard" turning points x_i with$|V'(x_i)| = \infty$ and ν_s the number of soft turning points x_i with $|V'(x_i)| < \infty$.

Thus, the quantized values of I_α and I_β read

$$I_\alpha = \hbar m, \tag{2.47a}$$

$$I_\beta = \hbar\left(n + \frac{1}{2}\right). \tag{2.47b}$$

Together with (2.44) we obtain

$$J = \hbar \left(n + |m| + \frac{1}{2} \right) = \hbar \left(j + \frac{1}{2} \right) \tag{2.48}$$

for the quantization of the angular momentum J, with $m \in \mathbb{Z}$ and $j \in \mathbb{N}_0$. A comparison with the exact eigenvalues $\hbar^2 j(j+1)$ of the angular momentum operator J^2 shows a difference of $\hbar^2/4$ which is negligible for $j \gg 0$.

2.4.2. WKB Approximation Method for Planar Rotations

The WKB approximation method is named after Gregor **W**entzel, Hendrik Anthony **K**ramers, and Léon **B**rillouin, who developed this method in 1926. In general it can be applied to any kind of one dimensional linear differential equations where the highest derivative is multiplied with a small coefficient. In case of Schrödinger's equation this is equivalent to the estimation that a potential varies only slowly in space compared to the de Broglie wavelength.

For planar rotations with a single degree of freedom $\alpha \in [0, 2\pi)$ and a potential $V(\alpha)$ the Schrödinger equation reads

$$\hbar^2 \frac{\mathrm{d}^2 \psi_{E_m}(\alpha)}{\mathrm{d}\alpha^2} + p_\alpha^2(\alpha) \psi_{E_m}(\alpha) = 0, \tag{2.49}$$

with the local momentum $p_\alpha(\alpha) = \sqrt{2I[E_m - V(\alpha)]}$. For an orientation independent potential $V(\alpha) = V$ equation (2.49) is solved by a plane wave

$$\psi_{E_m}(\alpha) = A e^{\pm i m \alpha}. \tag{2.50}$$

For a potential varying slowly in α we extend the ansatz (2.50) to [62]

$$\psi_{E_m}(\alpha) = A \exp \left[\pm \frac{i}{\hbar} S(\alpha) \right], \tag{2.51}$$

and expand the function $S(\alpha)$ in powers of $\hbar$,

$$S(\alpha) = S_0(\alpha) + \hbar S_1(\alpha) + \hbar^2 S_2(\alpha) + \mathcal{O}(\hbar^3). \tag{2.52}$$

Inserting ansatz (2.51) into the Schrödinger equation (2.49) yields

$$\begin{aligned} &\left[-[S_0'(\alpha)]^2 + p_\alpha^2(\alpha) \right] + \hbar[-2S_0'(\alpha)S_1'(\alpha) + iS_0''(\alpha)] \\ &+ \hbar^2 \left[-2S_0'(\alpha)S_2'(\alpha) - [S_1'(\alpha)]^2 + iS_1''(\alpha) \right] + \mathcal{O}(\hbar^3) = 0. \end{aligned} \tag{2.53}$$

From the terms in zero and first order in $\hbar$ it follows that

$$S_0(\alpha) = \pm \int_{\alpha_0}^{\alpha} \mathrm{d}\alpha' \; p_\alpha(\alpha'), \tag{2.54a}$$

$$S_1(\alpha) = \frac{i}{2} \ln\left[p_\alpha(\alpha)\right]. \tag{2.54b}$$

Here, the first expression represents the classical action integral. With both expressions we obtain

$$\psi_{E_m}(\alpha) \approx \frac{A}{\sqrt{p_\alpha(\alpha)}} \exp\left(\pm\frac{i}{\hbar}\int_{\alpha_0}^{\alpha} \mathrm{d}\alpha' p_\alpha(\alpha')\right). \tag{2.55}$$

The probability, $|\psi_{\mathrm{E_m}}(\alpha)|^2 = |A|^2/p_\alpha(\alpha)$, for finding a particle in the orientation α is as expected anti proportional to the classical orientation depending momentum $p_\alpha(\alpha)$. The smaller the momentum the longer the particle remains in this area.

The WKB approximation is valid for [62]

$$\hbar S_1'(\alpha) \ll S_0'(\alpha). \tag{2.56}$$

Around turning points, where $p_\alpha(\alpha) = 0$ applies, the WKB wave function diverges and the WKB approximation breaks down.

In the case of free flight without any potential and $p_\alpha(\alpha) = \sqrt{2IE_m}$ the eigenstate simplifies to

$$\psi_{E_m}(\alpha) \propto \frac{1}{\sqrt[4]{2IE_m}} \exp\left[\pm\sqrt{2IE_m}(\alpha - \alpha_0)\right]. \tag{2.57}$$

The periodic boundary condition $\psi_{E_m}(\alpha) = \psi_{E_m}(\alpha + 2\pi)$ leads to the quantized energy eigenvalues,

$$2\pi\frac{\sqrt{2IE_m}}{\hbar} = 2\pi m \Rightarrow E_m = \frac{\hbar^2 m^2}{2I}, \tag{2.58}$$

which are identical with the exact energy eigenvalues for the free flight. We see that from the periodic boundary condition follows the Bohr-Sommerfeld quantization rule for the action.

2.4.3. EBK Approximation Method for Linear Rotations

For integrable systems the WKB approximation can be extended to several dimensions. Analogue to the WKB method the energy eigenvalues are approximated by the quantization of the classical actions as in the Bohr-Sommerfeld quantization. This method is called EBK approximation, named after **E**instein, **B**rillouin and

Keller.

In the following we consider the motion of a linear rigid rotor in the presence of a potential depending on β which results in the Hamilton function

$$H(\alpha, \beta, p_\alpha, p_\beta) = \frac{1}{2I} \left(\frac{p_\alpha^2}{\sin^2 \beta} + p_\beta^2 \right) + V(\beta). \tag{2.59}$$

Here, the canonical momentum p_α and the total energy $E = H(\alpha, \beta, p_\alpha, p_\beta)$ are constants of motion. The action I_α is the same as the one for the free flight and we obtain

$$I_\alpha = p_\alpha = \hbar m. \tag{2.60}$$

For the action of the β-motion we have to take the external potential $V(\beta)$ into account yielding an effective β-depending potential

$$V_{\text{eff}}(\beta) = \frac{p_\alpha^2}{\sin^2 \beta} + V(\beta). \tag{2.61}$$

This potential diverges at $\beta = 0$ and $\beta = \pi$ and thus the β-motion has two turning points with $\cot \beta = 0$ which obey the equation

$$\frac{2}{I} \left[E - V(\beta_{\text{min,max}}) \right] - \frac{p_\alpha^2}{I^2 \sin^2 \beta} = 0. \tag{2.62}$$

With help of the turning points the quantization of I_β can be written as

$$I_\beta = \frac{1}{\pi} \int_{\beta_{\text{min}}(E, p_\alpha)}^{\beta_{\text{max}}(E, p_\alpha)} \mathrm{d}\beta \, \sqrt{2I[E - V(\beta)] - \frac{\hbar^2 m^2}{\sin^2 \beta}} = \hbar(n + 1/2), \tag{2.63}$$

where two Maslov indices $\nu_s = 1/4$ for the two turning points are taken into account. With $I_\beta = J - |M|$, see Eq. (2.44), and the quantization rules (2.47a), (2.48) for J and M we obtain

$$I_\beta = \hbar(j - |m| + 1/2). \tag{2.64}$$

2.4.4. Semiclassical Matrix Elements

For a semiclassical approximation of the matrix elements of an arbitrary operator we start with classical action-angle variables (I, α) and associate the classical action I with a semiclassical action operator I given by

$$\mathsf{I} = -i\hbar \frac{\partial}{\partial \alpha} + \delta \hbar, \tag{2.65}$$

with the Maslov index δ. The eigenfunctions and eigenvalue equation of this operator are [62]

$$\phi_n(\alpha) = (2\pi)^{-1/2} e^{in\alpha}, \tag{2.66a}$$

$$\mathsf{I}\phi_n(\alpha) = (n+\delta)\hbar\phi_n(\alpha). \tag{2.66b}$$

To obtain the matrix elements of an operator A we have to approximate it in action-angle variables. According to the correspondence principle one may associate the classical function $A(I,\alpha)$ with a semiclassical equivalent $A(\mathsf{I},\alpha)$ depending on the action operator I. The eigenfunctions of this semiclassical function are the action-angle wave functions with

$$A(\mathsf{I},\alpha)\phi_n(\alpha) = A[(n+\delta)\hbar, \alpha]\phi_n(\alpha). \tag{2.67}$$

The matrix elements of the operator A are then approximated by [62]

$$\begin{aligned}\langle n'|A(\mathsf{I},\alpha)|n\rangle &= \int_0^{2\pi} \mathrm{d}\alpha \phi_{n'}^*(\alpha) A(\mathsf{I},\alpha)\phi_n(\alpha) \\ &\approx \frac{1}{2\pi}\int_0^{2\pi} \mathrm{d}\alpha A[(\bar{n}+\delta)\hbar, \alpha] e^{i(n-n')\alpha}.\end{aligned} \tag{2.68}$$

Here, $\bar{n} = (n'+n)/2$ is introduced to ensure that the matrix elements describe a hermitian operator.

In the Hilbert space of the linear rigid rotor we are often confronted with operators $A(\mathsf{\alpha}, \mathsf{\beta}, p_\alpha, p_\beta)$ depending on the Euler angle operators $\mathsf{\alpha}$ and $\mathsf{\beta}$ and the corresponding canonical momentum operators. We replace these operators with the action-angle variables $(J, M, \alpha_J, \alpha_M)$ via [62]

$$\alpha = \alpha_M + \arctan(\zeta \tan\alpha_J) - \pi, \tag{2.69a}$$

$$\cos\beta = \cos\alpha_J \sqrt{1-\zeta^2}, \tag{2.69b}$$

$$\sin\beta = \sqrt{\sin^2\alpha_J + \zeta^2\cos^2\alpha_J}, \tag{2.69c}$$

$$p_\beta = J\frac{\sin\alpha_J\sqrt{1-\zeta^2}}{\sqrt{\sin^2\alpha_J + \zeta^2\cos^2\alpha_J}}, \tag{2.69d}$$

$$p_\alpha = M, \tag{2.69e}$$

with $\zeta = M/J$ and associate the actions M and J with semiclassical operators M and J yielding $A(\mathsf{J}, \mathsf{M}, \alpha_J, \alpha_M)$. The eigenfunction of this operator is the product of the eigenfunctions of the action operators M and J

$$\psi_{jm}(\alpha_j, \alpha_m) = \frac{1}{2\pi} e^{i(j\alpha_j + m\alpha_m)}, \tag{2.70}$$

and the eigenvalue equation reads

$$A(\mathsf{J}, \mathsf{M}, \alpha_j, \alpha_m)\psi_{jm}(\alpha_j, \alpha_m) = A[(j + 1/2)\hbar, m\hbar, \alpha_j, \alpha_m]\psi_{jm}(\alpha_j, \alpha_m). \tag{2.71}$$

Thus, the matrix elements are given by

$$\langle jm|\mathsf{A}|j'm'\rangle = \frac{1}{4\pi^2} \int_0^{2\pi} \mathrm{d}\alpha_j \int_0^{2\pi} \mathrm{d}\alpha_m \; e^{i\alpha_j(j-j')} e^{i\alpha_m(m-m')} A\left(\alpha_m, \alpha_j, \bar{m}, \bar{j}\right), \tag{2.72}$$

with $\bar{m} = (m+m')/2$ and $\bar{j} = (j+j')/2$. Note that this semiclassical approximation ignores the operator order.

3. Orientational Decoherence

A large part of my thesis is concerned with quantum experiments like superposition tests which exploit quantum effects in the rotational dynamics of aspherical nanoparticles. In chapter 2 I introduced the classical and quantum description of the rotational dynamics of a freely unitary evolving particle. But for the estimation of the viability of such experiments it is crucial to take interactions with the environment into account which may lead to orientational decoherence and could destroy the quantum behaviour.

The rotational dynamics of a nanoparticle in the presence of pure environmental decoherence is described by an orientational decoherence master equation [42]. In the diffusion limit, this equation turns into a simplified but general angular momentum diffusion master equation [43], which I will use later in this thesis. Both equations were derived during my master thesis, and here I briefly summarize the most important steps to gain an understanding of orientational decoherence and quantum angular momentum diffusion.

In the first part of this chapter, I give a short review about open quantum systems in general, mainly based on the works [64] and [65], followed by the master equation for orientational decoherence [42]. In the last part of this chapter I draw the diffusion limit [43] and discuss exemplary the time evolution for the planar rotor.

3.1. Open Quantum Systems

An open quantum system is a system S which interacts with a large, uncontrolled environment E. This interaction with the environment has a critical effect on the dynamics of our state operator ρ describing the state of the system S, in particular it leads to decoherence of the state: a decay of the coherences and localization of the state, meaning that the state operator ρ turns into a classical mixture and contains no longer superpositions.

In the following, the state of the system of interest, for example a nanorotor, is denoted ρ and the state of the environment ρ_{E}. The state of the total system is ρ_{tot}. The Hilbert space of the total system $\mathcal{H}_{\mathrm{tot}}$ is the tensor product of the Hilbert space $\mathcal{H}_{\mathrm{S}}$ and the Hilbert space of the environment $\mathcal{H}_{\mathrm{E}}$, $\mathcal{H}_{\mathrm{tot}} = \mathcal{H}_{\mathrm{S}} \otimes \mathcal{H}_{\mathrm{E}}$. The complete

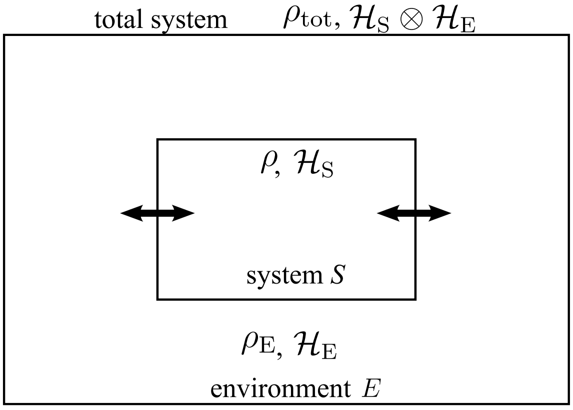

Figure 3.1.: Sketch of an open system S described by the state operator ρ interacting with an environment E with state operator ρ_{E}. The total system is described by the state operator ρ_{tot}. The Hilbert space of this total system is the tensor product of the system Hilbert space $\mathcal{H}_{\mathrm{S}}$ and the environmental Hilbert space $\mathcal{H}_{\mathrm{E}}$, $\mathcal{H}_{\mathrm{tot}} = \mathcal{H}_{\mathrm{E}} \otimes \mathcal{H}_{\mathrm{S}}$. Figure taken from [66].

system, however, is once again a closed, unitary system.

Time Evolution

The time evolution of the complete system is unitary and can be described by the von-Neumann equation

$$\partial_t \rho_{\mathrm{tot}} = -\frac{i}{\hbar} \left[\mathsf{H}_{\mathrm{tot}}, \rho_{\mathrm{tot}} \right], \tag{3.1}$$

where we use the total Hamiltonian

$$\mathsf{H}_{\mathrm{tot}} = \mathsf{H}_{\mathrm{S}} \otimes \mathbb{1}_{\mathrm{E}} + \mathbb{1}_{\mathrm{S}} \otimes \mathsf{H}_{\mathrm{E}} + \mathsf{H}_{\mathrm{int}}. \tag{3.2}$$

It is the sum of Hamiltonian H_{S} acting on the Hilbert space $\mathcal{H}_{\mathrm{S}}$ of the system, the Hamiltonian H_{E} acting on $\mathcal{H}_{\mathrm{E}}$ and the interaction Hamiltonian $\mathsf{H}_{\mathrm{int}}$ acting on the total Hilbert space.

We are interested in the time evolution of our system. By tracing out the environmental degrees of freedom we obtain the density operator $\rho = \mathrm{tr}_E(\rho_{\mathrm{tot}})$ from the density operator ρ_{tot} of the complete closed system. This partial trace of an operator A_{SE} acting on the Hilbert space $\mathcal{H}_{\mathrm{tot}}$ is defined as

$$\mathrm{tr}_E(\mathsf{A}_{\mathrm{SE}}) = \sum_i = \langle k_i | \mathsf{A}_{\mathrm{SE}} | k_i \rangle, \tag{3.3}$$

with $|k_i\rangle$ the orthogonal basis vectors of $\mathcal{H}_E$. With this partial trace we can describe the time evolution of the density operator ρ by

$$\partial_t \rho = -\frac{i}{\hbar} \mathrm{tr}_{\mathrm{E}} \left([\mathsf{H}_{\mathrm{tot}}, \rho_{\mathrm{tot}}] \right), \tag{3.4}$$

which is not a closed time evolution. In the following, I show how to derive a closed equation for ρ with the Markov approximation.

Markov Master Equation in Lindblad Form

We assume that the initial state of the system is uncorrelated with the environment. Thus, we can write the initial total state $\rho_{\mathrm{tot}}(0)$ as a product state of the initial state of the system and the environment, $\rho_{\mathrm{tot}}(0) = \rho(0) \otimes \rho_E$. Due to the interaction of the system with the environment the states become correlated for $t > 0$. From the correlations follow that the change of a state at each time depends not only on the actual state at this point in time, but on the complete time evolution up until this instant. The time evolution of the system depends on the history of the whole state, one can say that the environment has a memory.

In the Markov approximation we assume that we can neglect these memory effects on time scales much greater than the correlation time scale. In this case the change of ρ depends only on the current state of the system and can be described by a Liouville superoperator $\tilde{\mathcal{L}}$ [65],

$$\partial_t \rho = \tilde{\mathcal{L}} \rho. \tag{3.5}$$

This type of master equation is called a Markovian master equation.

The Liouville superoperator is a generator of a dynamical map $\mathcal{W}_t = \exp(\tilde{\mathcal{L}} t)$ for times $t > 0$. It maps the initial state $\rho(0)$ onto states $\rho(t)$ at later points in time t [65]

$$\mathcal{W}_t : \rho(0) \to \rho(t) \qquad t > 0. \tag{3.6}$$

To preserve the properties of a quantum state the dynamical map has to obey three requirements. It has to be trace-preserving, convex linear and completely positive. Preserving of the trace ensures the normalization of the state $\rho(t)$ for each time, $\mathrm{tr}[\rho(t)] = 1$. The convex linearity is given by

$$\mathcal{W}_t[\lambda \rho_1 + (1-\lambda)\rho_2] = \lambda \mathcal{W}_t(\rho_1) + (1-\lambda)\mathcal{W}_t(\rho_2) \;\; 0 \leq \lambda \leq 1. \tag{3.7}$$

And finally the complete positivity

$$\mathcal{W}_t \otimes \mathbb{1}_{\text{ext}} > 0 \tag{3.8}$$

guarantees that the map $\mathcal{W}_t$ itself and further all tensor product extensions of $\mathcal{W}_t$ to higher dimensions are positive.

If the $\mathcal{W}_t$ fulfil the additional requirement

$$\mathcal{W}_{t_2}(\mathcal{W}_{t_1}(.)) = \mathcal{W}_{t_1+t_2}(.) \quad \text{for all } t_1, t_2 > 0 \tag{3.9}$$

the $\mathcal{W}_t$ form a dynamical semigroup [65]. This property is corresponding to the Markov assumption that the change of a state depends only on the actual state and not on the interaction history.

A general generator of such a dynamical semigroup is given by a master equation in Lindblad form [64, 65]

$$\partial_t \rho = -\frac{i}{\hbar}\left[\tilde{\mathsf{H}}, \rho\right] + \sum_k \gamma_k \left(\mathsf{L}_k \rho \mathsf{L}_k^\dagger - \frac{1}{2}\left\{\mathsf{L}_k^\dagger \mathsf{L}_k, \rho\right\}\right), \tag{3.10}$$

with the rates $\gamma_k > 0$ and the dimensionless Lindblad operators L_k. The first part of equation (3.10) describes the unitary part of the time evolution. Note that the operator $\tilde{\mathsf{H}}$ is hermitian but is not necessarily the Hamiltonian of the system. The second part of equation (3.10) describes the incoherent part of the time evolution. One method to derive this master equation microscopically is to assume only a weak interaction Hamiltonian H_{int}. In the following, I use the Monitoring Approach [65, 67], a non-perturbative method, to derive the master equation of orientational decoherence.

Monitoring Approach

In the Monitoring Approach the interaction with the environment is imagined as consisting of single scattering processes of environmental particles with our particle of interest. Additionally, we assume that the correlation between system and environment induced by the scattering event disperses quickly on a timescale much smaller than the scattering timescale. Thus, the total density operator prior to each collision can be written as a product state, $\rho_{\text{tot}} = \rho \otimes \rho_{\text{E}}$.

The two important operators describing the interaction with the environment are the rate operator Γ and the scattering operator S, both acting on the total Hilbert space $\mathcal{H}_{\text{tot}}$. The expectation values of the rate operator as well as of the scattering operator depend on the total state $\rho \otimes \rho_{\text{E}}$. In order to derive the master equation

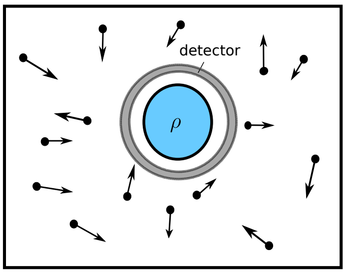

Figure 3.2.: The system interacts with environmental gas particles. In the monitoring approach we assume an imaginary detector which detects a gas particle before the scattering event to include the state-dependent scattering operator into the dynamical description.

we assume an imaginary transit detector which monitors the system and detects, whether an environmental particle is passing it and will be scattered at the system. The rate operator yields the probability for a collision in the time interval Δt [65]

$$\mathrm{Prob}\left(C_{\Delta t}|\rho\otimes\rho_{\mathrm{E}}\right)=\Delta t\ \mathrm{tr}(\mathsf{\Gamma}\rho_{\mathrm{tot}}). \tag{3.11}$$

Both the information of the detector that there will be a collision and the collision itself affects the state, yielding the state after the collision

$$\mathcal{M}(\rho_{\mathrm{tot}}|C_{\Delta t})=\frac{\mathsf{S}\mathsf{\Gamma}^{1/2}\rho_{\mathrm{tot}}\mathsf{\Gamma}^{1/2}\mathsf{S}^{\dagger}}{\mathrm{tr}(\mathsf{\Gamma}\rho_{\mathrm{tot}})}. \tag{3.12}$$

The total state ρ_{tot} after a time interval Δt is then given by the state after the collision (3.12) multiplied with the probability $\mathrm{Prob}(C_{\Delta t})$ that there is a collision in the time interval plus the state ρ_{tot} without any changes multiplied with the probability $\mathrm{Prob}(\overline{C}_{\Delta t})=1-\mathrm{Prob}(C_{\Delta t})$ of no collision. After tracing out the environment and drawing the limit $\Delta t\to 0$ of a continuous monitoring we obtain the master equation

$$\partial_t\rho=-\frac{i}{\hbar}[\mathsf{H},\rho]+\mathcal{R}\rho+\mathcal{L}\rho, \tag{3.13}$$

with the two superoperators $\mathcal{R}$ and $\mathcal{L}$.

The first term $\mathcal{R}\rho$ is unitary and reads [65]

$$\mathcal{R}\rho=i\mathrm{tr}_{\mathrm{E}}\left(\left[\mathrm{Re}(\mathsf{T}),\mathsf{\Gamma}^{1/2}(\rho\otimes\rho_{\mathrm{E}})\mathsf{\Gamma}^{1/2}\right]\right), \tag{3.14}$$

where I introduced the operator T connected to the scattering operator via $\mathsf{S}=\mathbb{1}+i\mathsf{T}$. It describes a renormalization of the energy due to the interaction with the environment. The second term $\mathcal{L}\rho$ describes the incoherent part of the time evolution with [65]

$$\begin{aligned}\mathcal{L}\rho = &+ \mathrm{tr}_{\mathrm{E}}\left(\mathsf{T}\Gamma^{1/2}[\rho\otimes\rho_{\mathrm{E}}]\Gamma^{1/2}\mathsf{T}^{\dagger}\right)\\ &-\frac{1}{2}\mathrm{tr}_{\mathrm{E}}\left(\Gamma^{1/2}\mathsf{T}^{\dagger}\mathsf{T}\Gamma^{1/2}[\rho\otimes\rho_{\mathrm{E}}]\right)\\ &-\frac{1}{2}\mathrm{tr}_{\mathrm{E}}\left([\rho\otimes\rho_{\mathrm{E}}]\Gamma^{1/2}\mathsf{T}^{\dagger}\mathsf{T}\Gamma^{1/2}\right).\end{aligned} \tag{3.15}$$

The Monitoring Approach was for example used for a non-perturbative derivation of the quantum linear Boltzmann equation [68]. In a similar way the master equation for orientational decoherence can be derived [42].

3.2. Orientational Decoherence Master Equation

With the general knowledge about open quantum systems and in particular the Monitoring Approach we can now derive a master equation which describes decoherence of the orientational degrees of freedom of an aspherical nanoparticle interacting with a gaseous environment.

3.2.1. Monitoring Master Equation

In order to derive the master equation we have to specify the rate and scattering operators used in the Monitoring Approach. With this we can write down the master equation (3.15). The master equation shall describe the dynamics of an aspherical anisotropic nanoparticle with mass M and state ρ_{N}, interacting with a homogeneous gaseous environment with gas particle mass $m_{\mathrm{g}} \ll M$ and particle density n_{g}. The high mass of the nanoparticle in comparison to the mass of the gas particles implies that typreally its rotation period is long in comparison to the interaction timescale. Thus, we can assume that the orientation does not change during one scattering event and that the rate and scattering operators are diagonal in the orientational degress of freedom Ω [42].

Since the orientation Ω of the particle enters the scattering amplitudes $f(\mathbf{p}_f, \mathbf{p}_i, \Omega)$ only in a parametric fashion the superoperators $\mathcal{R}\rho$ and $\mathcal{L}\rho$ can be derived in a same way as for the quantum linear Boltzmann equation [68]. Therefore, I will give only the main idea of the derivation with important steps and assumptions to obtain the equations relevant for this thesis. A derivation of the ro-translational master equation describing orientational decoherence can be found in Ref. [42].

We can write the total Hilbert space $\mathcal{H}_{\mathrm{tot}}$ as a tensor product of the Hilbert space of the center of mass coordinates $\mathcal{H}_{\mathrm{cm}}$ and the Hilbert space $\mathcal{H}_{\mathrm{rel}}$ of the relative coordinates, $\mathcal{H}_{\mathrm{tot}} = \mathcal{H}_{\mathrm{cm}} \otimes \mathcal{H}_{\mathrm{rel}}$. The scattering operator T as well as the rate operator $\mathsf{\Gamma}$ act only on the Hilbert space $\mathcal{H}_{\mathrm{rel}}$ of the relative coordinates. So, we introduce the relative momentum vector $\mathbf{p}_r(\mathbf{p},\mathbf{P}) = m_r\mathbf{p}/m - m_r\mathbf{P}/M$, depending on the momentum $\mathbf{p}$ of the gas particle and $\mathbf{P}$ of the nanoparticle. Here, m_r denotes the reduced mass $m_r = mM/(m+M)$. We can now write the scattering and the rate operator in terms of a scattering amplitude $f(\mathbf{p}_f, \mathbf{p}_i; \Omega)$ which describes a scattering event with incoming relative momentum $\mathbf{p}_i$ and outgoing relative momentum $\mathbf{p}_f$ for a fixed orientation Ω.

The rate operator $\mathsf{\Gamma}$ is the product of the particle flux $\mathsf{j}(\mathbf{p},\mathbf{P}) = n_g|\mathbf{p}_r(\mathbf{p},\mathbf{P})|/m_r$ and the total scattering cross section $\sigma_{\mathrm{tot}}(\mathbf{p}_i;\Omega) = \int_{S_2} \mathrm{d}^2\,|f(p_i\mathbf{n},\mathbf{p}_i;\Omega)|$

$$\mathsf{\Gamma} = \mathbb{1}_{\mathrm{cm}} \otimes \frac{n_g}{m_r}|\mathbf{p}_r(\mathbf{p},\mathbf{P})| \int_{S_2} \mathrm{d}^2\mathbf{n}\,|f(p_i(\mathbf{p},\mathbf{P})\mathbf{n}, \mathbf{p}_i(\mathbf{p},\mathbf{P});\Omega)|. \tag{3.16}$$

Note that the momentum $\mathbf{P}$ and the orientation Ω of the nanoparticle enter here as operator valued quantities. The non-trivial part T_0 of the scattering operator $\mathsf{T} = \mathbb{1}_{\mathrm{cm}} \otimes \mathsf{T}_0$ reads

$$\langle \mathbf{p}_f|\mathsf{T}_0|\mathbf{p}_i\rangle = \frac{1}{2\pi\hbar}\delta\left(\frac{p_f^2 - p_i^2}{2}\right) f(\mathbf{p}_f, \mathbf{p}_i; \Omega). \tag{3.17}$$

Since the environmental gas is homogeneous and stationary, its state operator ρ_{E} is diagonal in the momentum operator p with the matrix elements $\langle \mathbf{p}|\rho_{\mathrm{E}}|\mathbf{p}\rangle = \mu(\mathbf{p})$.

The Renormalization of the Energy

The superoperator $\mathcal{R}\rho_{\mathrm{N}}$ leads to a momentum and orientation dependent energy shift H_{g}, $\mathcal{R}\rho_{\mathrm{N}} = -i[\mathsf{H}_g, \rho_{\mathrm{N}}]/\hbar$. In the limit $m \ll M$ the relative momentum $\mathbf{p}_r$ is approximately given by the momentum $\mathbf{p}$ of the gas particle. When we additionaly assume an isotropic gas with $\mu(\mathbf{p}) = \mu(p)$ the matrix elements of $\mathcal{R}\rho$ vanish, so that the energy shift is constant and does not affect the time evolution [42].

The Incoherent Time Evolution

The superoperator $\mathcal{L}\rho_{\mathrm{N}}$ describes the incoherent time evolution. Calculating it in the limit $m \ll M$ one obtains [42]

$$\mathcal{L}\rho_{\mathrm{N}} = \frac{n_{\mathrm{g}}}{m}\int \mathrm{d}^3\mathbf{p} \int \mathrm{d}^2\mathbf{n}'\, p\mu(\mathbf{p}) \left[\mathsf{L}_{p\mathbf{n}'}\rho_{\mathrm{N}}\mathsf{L}_{p\mathbf{n}'}^{\dagger} - \frac{1}{2}\left\{\rho_{\mathrm{N}}, \mathsf{L}_{p\mathbf{n}'}^{\dagger}\mathsf{L}_{p\mathbf{n}'}\right\}\right], \tag{3.18}$$

with the initial momentum $\mathbf{p} = p\mathbf{n}$ and the final momentum $\mathbf{p}' = p\mathbf{n}'$. The Lindblad operators can be written in terms of the scattering amplitude,

$$\mathsf{L}_{p\mathbf{n}'} = e^{\mathbf{R}\cdot(\mathbf{p}-p\mathbf{n}')/\hbar} f(p\mathbf{n}', \mathbf{p}; \Omega). \tag{3.19}$$

The Lindblad operator (3.19) depends on the operator-valued orientation Ω and the center of mass position $\mathbf{R}$ of the nanoparticle.

The total ro-translational master equation,

$$\partial_t \rho_\mathrm{N} = -\frac{i}{\hbar}[\mathsf{H} + \mathsf{H}_\mathrm{g}, \rho_\mathrm{N}] + \mathcal{L}\rho_\mathrm{N}, \tag{3.20}$$

describes the ro-translation motion of the particle including the interaction with the environment. The incoherent part $\mathcal{L}\rho_\mathrm{N}$ leads to decoherence both in the center of mass and in the orientational degrees of freedom of the nanoparticle.

In order to obtain the master equation for only the rotational state $\rho_\mathrm{rot} = \mathrm{tr}_\mathrm{CM}(\rho_\mathrm{N})$, in the following denoted by ρ, we have to trace out the center of mass degrees of freedom, yielding [42]

$$\begin{aligned} \partial_t \rho = & -\frac{i}{\hbar}[\mathsf{H}_\mathrm{rot} + \mathsf{H}_\mathrm{g}, \rho] + \int_0^\infty \mathrm{d}p \, p^3 \int_{S_2} \mathrm{d}\mathbf{n} \int_{S_2} \mathrm{d}\mathbf{n}' \, \mu(p) \\ & \times \left[f(p\mathbf{n}', p\mathbf{n}; \Omega)\rho f^*(p\mathbf{n}', p\mathbf{n}; \Omega) - \frac{1}{2}\left\{\rho, |f(p\mathbf{n}', p\mathbf{n}; \Omega)|^2\right\}\right]. \end{aligned} \tag{3.21}$$

We can now calculate the orientational localization rate $F(\Omega, \Omega') = \langle \Omega | \mathcal{L}\rho | \Omega' \rangle$ and see that the superoperator $\mathcal{L}$ indeed leads to a decay of the coherences in the orientation representation, i.e. a localization of the orientation [42]

$$F(\Omega, \Omega') = \frac{n_g}{2m} \int_0^\infty \mathrm{d}p \, p^3 \mu(p) \int_{S_2} \mathrm{d}^2\mathbf{n}' \int_{S_2} \mathrm{d}^2\mathbf{n} \, |f(p\mathbf{n}', p\mathbf{n}; \Omega) - f(p\mathbf{n}', p\mathbf{n}; \Omega')|^2. \tag{3.22}$$

The localization rate is always positive and vanishes for a completely localized particle with $\Omega = \Omega'$.

3.2.2. Angular Momentum Diffusion Master Equation

We have seen that the collisional interaction with the environment leads to decoherence in the orientation. From the decoherence master equations for the center of mass degrees of freedom we know that they describe diffusion in the momentum for small momentum transfers during the scattering event [64,68–70], so one can assume that the orientational decoherence master equation gives rise to angular momentum

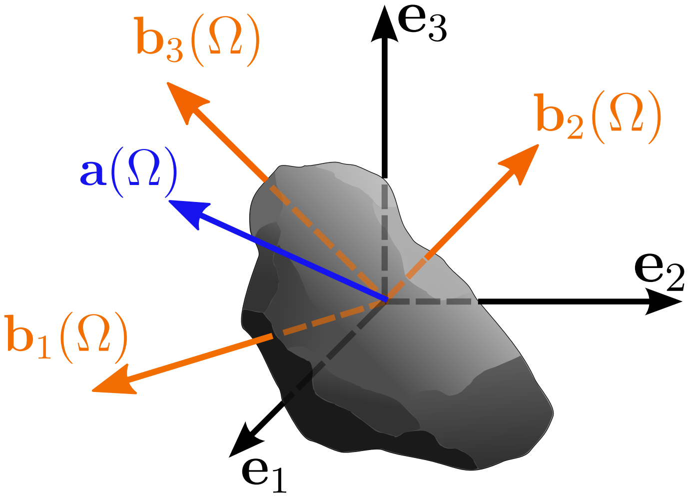

Figure 3.3.: Illustration of the orientation of an arbitrarily shaped asymmetric particle. The black axes $\{\mathbf{e}_1, \mathbf{e}_2, \mathbf{e}_3\}$ define the space-fixed frame. In blue we see the orientation dependent vector $\mathbf{a}(\Omega)$ and in orange the orientation dependent eigenvectors $\mathbf{b}_i$ of the tensor $\mathsf{B}(\Omega)$.(Figure taken from [66])

diffusion in the limit of small anisotropies [43].

Later in this thesis, I will use the angular momentum diffusion equation for symmetric particles. In the following, I give a short idea of the concepts [43] to derive this equation and discuss and illustrate the result for planar rotations using the Wigner-Weyl formalism.

In order to derive the angular momentum diffusion master equation we start with the orientational decoherence master equation (3.21) and approximate the scattering amplitudes $f(p\mathbf{n}', p\mathbf{n}; \Omega)$ for small anisotropies by the sum of a scattering amplitude $f_{\text{sph}}(p\mathbf{n}', p\mathbf{n})$ for an isotropic potential and a second part $g(p\mathbf{n}', p\mathbf{n}, \Omega)$ which takes the anisotropy in leading order into account. This is equivalent to an interaction potential which depends only weakly on the orientation. The isotropic potential does not affect the incoherent rotational dynamics so that we focus on the anisotropic part of the the scattering amplitude. We first exploit the isotropy of the momentum distribution and rotate the coordinate system so that we have $g(p\mathbf{n}', p\mathbf{n}; \Omega) = g(p\mathsf{R}^T\mathbf{n}', p\mathsf{R}^T\mathbf{n}; 0)$. Then we expand the momentum dependencies of the scattering amplitude $g(p\mathsf{R}^T\mathbf{n}', p\mathsf{R}^T\mathbf{n}; 0)$ in spherical harmonics until $\ell = \ell' = 2$,

$$g(p\mathsf{R}^T(\Omega)\mathbf{n}', p\mathsf{R}^T(\Omega)\mathbf{n}; 0) = \sum_{\ell,\ell'=0}^{2} \sum_{m=-\ell}^{\ell} \sum_{m'=-\ell'}^{\ell'} f_{\ell\ell'}^{mm'} Y_\ell^m[\mathsf{R}^T(\Omega)\mathbf{n}] Y_{\ell'}^{m'}[\mathsf{R}^T(\Omega)\mathbf{n}']. \quad (3.23)$$

This way we ensure to take only the lowest order which accounts for the anistropy into account. From the time-reversal invariance of the scattering amplitude [71],

$f(p\mathbf{n}', p\mathbf{n}; \Omega) = f(-p\mathbf{n}, -p\mathbf{n}'; \Omega)$, follows for the expansion coefficients

$$f_{\ell\ell'}^{mm'}(p) = (-1)^{\ell+\ell'} f_{\ell\ell'}^{mm'}. \tag{3.24}$$

With this we obtain a scattering amplitude approximated for small anisotropies in the potential [43]

$$\begin{aligned} f(p\mathbf{n}', p\mathbf{n}; \Omega) \approx & f_{\mathrm{sph}}(p\mathbf{n}', p\mathbf{n}) + f_{00}^{00}(p) + \mathbf{A}(p, \Omega) \cdot (\mathbf{n} - \mathbf{n}') + \mathbf{n} \cdot \mathsf{B}(p, \Omega)\mathbf{n} \\ & + \mathbf{n}' \cdot \mathsf{B}(p, \Omega)\mathbf{n}' + \mathbf{n} \cdot \mathsf{C}(p, \Omega)\mathbf{n}'. \end{aligned} \tag{3.25}$$

The expansion coefficients $f_{\ell\ell'}^{mm'}$ are included in the complex vector $\mathbf{A}(p, \Omega) = \mathsf{R}(\Omega)\mathsf{A}_0(p)$ and the symmetric tensors $\mathsf{B}(p, \Omega) = \mathsf{R}(\Omega)\mathsf{B}_0(p)\mathsf{R}^T(\Omega)$ and $\mathsf{C}(p, \Omega) = \mathsf{R}(\Omega)\mathsf{C}_0(p)\mathsf{R}^T(\Omega)$. For inversion symmetric scattering amplitudes, $f(-p\mathbf{n}', -p\mathbf{n}; \Omega) = f(p\mathbf{n}', p\mathbf{n}; \Omega)$, the vector $\mathbf{A}(p; \Omega)$ must vanish.

Now I insert this expression (3.25) in the orientational decoherence master equation (3.21). The term $f_{00}^{00}(p)$ does not depend on the orientation of the particle and vanishes as well as the spherical part $f_{\mathrm{sph}}(p\mathbf{n}', p\mathbf{n})$. The mixed terms between $\mathsf{B}(p, \Omega)$ and $\mathsf{C}(p, \Omega)$ are linear in either the unit vector $\mathbf{n}$ or $\mathbf{n}'$ and thus the corresponding integration vanishes. The mixed terms between $\mathbf{A}(p, \Omega)$ and $\mathsf{B}(p, \Omega)$ respectively $\mathsf{C}(p, \Omega)$ vanish partly as well because of the linearity in $\mathbf{n}$ or $\mathbf{n}'$. The other parts cancel each other because of the factors $\mathbf{n}$ and $-\mathbf{n}'$. And even the mixed term involving the tensor $\mathbf{B}(p, \Omega)$ with primed and unprimed unit vector $\mathbf{n}$ cancel. From this follows that the superoperator $\mathcal{L}\rho$ splits into two terms, one linear in the orientation and another one which depends quadratically on the orientation Ω [43],

$$\partial_t \rho = -\frac{i}{\hbar}[\mathbf{H}_{\mathrm{rot}}, \rho] + \mathcal{L}_1\rho + \mathcal{L}_2\rho, \tag{3.26}$$

with

$$\begin{aligned} \mathcal{L}_1\rho = & \frac{4\pi n_g}{m} \int_0^\infty \mathrm{d}p\, p^3 \mu(p) \int_{S_2} \mathrm{d}^2\mathbf{n} \Big[[\mathbf{n} \cdot \mathbf{A}(p, \Omega)]\rho[\mathbf{n} \cdot \mathbf{A}^*(p; \Omega)] \\ & - \frac{1}{2}\left\{ |\mathbf{n} \cdot \mathbf{A}(p; \Omega)|^2, \rho \right\} \Big], \end{aligned} \tag{3.27a}$$

$$\begin{aligned} \mathcal{L}_2\rho = & \frac{8\pi n_g}{m} \int_0^\infty \mathrm{d}p\, p^3 \mu(p) \int_{S_2} \mathrm{d}^2\mathbf{n} \Big[[\mathbf{n} \cdot \mathsf{B}(p; \Omega)\mathbf{n}]\rho[\mathbf{n} \cdot \mathsf{B}^*(p; \Omega)\mathbf{n}] \\ & - \frac{1}{2}\left\{ |\mathbf{n} \cdot \mathsf{B}(p; \Omega)\mathbf{n}|^2, \rho \right\} \Big] \\ & + \frac{n_g}{m} \int_0^\infty \mathrm{d}p\, p^3 \mu(p) \int_{S_2} \mathrm{d}^2\mathbf{n} \int_{S_2} \mathrm{d}^2\mathbf{n}' \Big[[\mathbf{n} \cdot \mathsf{C}(p; \Omega)\mathbf{n}']\rho[\mathbf{n} \cdot \mathsf{C}^*(p; \Omega)\mathbf{n}'] \\ & - \frac{1}{2}\left\{ \mathbf{n} \cdot \mathsf{C}(p; \Omega)\mathbf{n}'|^2, \rho \right\} \Big]. \end{aligned} \tag{3.27b}$$

For the simplest possible version of an angular momentum diffusion master equation we reduce the expressions (3.27a) and (3.27b) to the most elementary form. In a first step, we omit the integral over the momentum p, because the equation (3.21) describes decoherence even for a sharp momentum distribution $\mu(p)$. Further, we assume that the vector $\mathbf{A}$ and the tensors B and $\mathbf{C}$ are real. These assumptions do not have an effect on the decoherence rate because the imaginary part only gives rise to an additional phase oscillation [42]. And in a last step we reduce the two terms in (3.27b) to a single term, because the matrix elements of the two terms differ only by a constant factor. Thus, there cannot be any additional information from the tensor $\mathsf{C}(p;\Omega)$ which is not contained in $\mathsf{B}(p;\Omega)$. After all simplifications we obtain the expressions

$$\mathcal{L}_1\rho = \gamma_1 \int_{S_2} \frac{\mathrm{d}^2\mathbf{n}}{4\pi}\left[[\mathbf{n}\cdot\mathbf{A}(\Omega)]\rho[\mathbf{n}\cdot\mathbf{A}(\Omega)] - \frac{1}{2}\left\{|\mathbf{n}\cdot\mathbf{A}(\Omega)|^2,\rho\right\}\right], \tag{3.28a}$$

$$\mathcal{L}_2\rho = \gamma_2 \int_{S_2} \frac{\mathrm{d}^2\mathbf{n}}{4\pi}\left[[\mathbf{n}\cdot\mathsf{B}(\Omega)\mathbf{n}]\rho[\mathbf{n}\cdot\mathsf{B}(\Omega)\mathbf{n}] - \frac{1}{2}\left\{|\mathbf{n}\cdot\mathsf{B}(\Omega)\mathbf{n}|^2,\rho\right\}\right], \tag{3.28b}$$

with the vector $\mathbf{A}(\Omega) = A\mathbf{a}(\Omega)$, $\mathbf{a}(\Omega) = \mathsf{R}(\Omega)\mathbf{a}_0$ and the tensor $\mathsf{B}(\Omega) = \sum_{i=1}^{3} B_i\mathbf{b}_i(\Omega)\otimes\mathbf{b}_i(\Omega)$.

The corresponding localization rates $F_1(\Omega,\Omega')$ and $F_2(\Omega,\Omega')$ read

$$F_1(\Omega,\Omega') = \frac{2D^{(1)}}{\hbar^2}\left[1 - \mathbf{a}(\Omega)\cdot\mathbf{a}(\Omega')\right], \tag{3.29a}$$

$$F_2(\Omega,\Omega') = \frac{1}{2\hbar^2}\sum_{i=1}^{3}\left(\sum_{j=1}^{3} D_j^{(2)} - 2D_i^{(2)}\right)|\mathbf{b}_i(\Omega)\times\mathbf{b}_i(\Omega')|^2, \tag{3.29b}$$

with the diffusion coefficients

$$D^{(1)} = \frac{\gamma_1\hbar^2}{6}A^2, \tag{3.30a}$$

$$D_i^{(2)} = \frac{2\gamma_2\hbar^2}{15}(B_j - B_k)^2. \tag{3.30b}$$

It can be shown [43] that the sum of localization rates (3.29a) and (3.29b) vanish only when $\Omega = \Omega'$. From this follows that the superoperators (3.28a) and (3.28b) lead to a complete localization of the state. For an inversion symmetric particle the Liouvillian (3.28a) vanishes and with this the localization rate is zero for $b_i(\Omega) = \pm b_i(\Omega')$. Thus, the Liouvillian (3.28b) does not effect superpositions of orientations $b_i(\Omega)$ and $-b_i(\Omega)$ which is not surprising because of the indistinguishability of these orientations for inversion symmetric particles.

The master equation (3.26) describes quantum angular moment diffusion. To demonstrate this I calculate the time evolution of the expectation value of the angular momentum operator J and of its tensor of second moments $\mathsf{J}\otimes\mathsf{J}$. For a diffusive process we expect that the first moment is constant in time and that the tensor of second moments increases linearly with time

$$\partial_t\langle\mathsf{J}\rangle = 0, \qquad \partial_t\langle\mathsf{J}\otimes\mathsf{J}\rangle = 2\langle\mathsf{D}(\Omega)\rangle, \tag{3.31}$$

with the diffusion tensor $\mathsf{D}(\Omega)$. We start with the expectation value $\partial_t\langle\mathsf{J}\rangle = \mathrm{tr}(\mathsf{J}\partial_t\rho)$ and insert the master equation (3.26) for $\partial_t\rho$. The angular momentum operator is a constant of motion and thus commutes with the rotational Hamiltonian $\mathrm{H}_{\mathrm{rot}}$. From this it follows that we only have to calculate the incoherent part $\mathrm{tr}(\mathsf{J}\mathcal{L}\rho)$. A cyclic permutation within the trace leads to $\partial_t\langle\mathsf{J}\rangle = \langle\mathcal{L}\mathsf{J}\rangle$. For the further calculation we use the expression (2.20c) for the components of the angular momentum operator related to the space-fixed frame. With this we obtain $\partial_t\langle\mathsf{J}\rangle = 0$ and in a similar way [43]

$$\partial_t\langle\mathsf{J}\otimes\mathsf{J}\rangle = 2\langle\mathsf{D}^{(1)}(\Omega) + \mathsf{D}^{(2)}(\Omega)\rangle, \tag{3.32}$$

with the diffusion tensors

$$\mathsf{D}^{(1)}(\Omega) = D^{(1)}[\mathbb{1} - \mathbf{a}(\Omega)\otimes\mathbf{a}(\Omega)], \tag{3.33a}$$

$$\mathsf{D}^{(2)}(\Omega) = \sum_{i=1}^{3} D_i^{(2)}\mathbf{b}_i(\Omega)\otimes\mathbf{b}_i(\Omega). \tag{3.33b}$$

From this it follows that the superoperators (3.28a) and (3.28b) induce angular moment diffusion in a way that the second moments of the angular moment operator increases linearly in time.

Angular Momentum Diffusion of the Symmetric Rotor

So far, I discussed the general case of an arbitrarily shaped asymmetric rigid rotor. Throughout my thesis we will often assume the particle to be a symmetric rotor or even a linear rigid rotor. In the following, I discuss these two cases.

The interaction of an azimuthally symmetric particle with the environment depends only on the orientation of its symmetry axis $\mathbf{m}(\Omega) = \mathsf{R}(\Omega)\mathbf{e}_3$. With this only two orientational degrees of freedom can be localized, the α- and the β-rotation, while the rotation around the body-fixed $\mathbf{n}_3$-axis, the symmetry axis, cannot be localized. The superoperators (3.28a) and (3.28b) turn in the limit of a symmetric rotor into the same expression as in the limit of a linear rigid rotor. The master equation then only differs in the rotational Hamiltonian.

For the calculation of the Liouvillian $\mathcal{L}_1$ and $\mathcal{L}_2$ we assume the vector $\mathbf{a}(\Omega)$ in (3.28a) to point along the symmetry axis $\mathbf{m}(\Omega)$ and write also the tensor $\mathsf{B}(\Omega)$ in terms of the vector $\mathbf{m}(\Omega)$,

$$\mathsf{B}(\Omega) = \mathbb{1}B_\perp + (B_\parallel - B_\perp)\mathbf{m}(\Omega) \otimes \mathbf{m}(\Omega). \tag{3.34}$$

With this expressions the Liouvillian read

$$\mathcal{L}_1\rho = \frac{6D^{(1)}}{\hbar^2}\int_{S_2}\frac{\mathrm{d}^2\mathbf{n}}{4\pi}\left[[\mathbf{n}\cdot\mathbf{m}(\Omega)]\rho[\mathbf{n}\cdot\mathbf{m}(\Omega)] - \frac{1}{2}\left\{|\mathbf{n}\cdot\mathbf{m}(\Omega)|^2,\rho\right\}\right], \tag{3.35a}$$

$$\mathcal{L}_2\rho = \frac{15D^{(2)}}{\hbar^2}\int_{S_2}\frac{\mathrm{d}^2\mathbf{n}}{4\pi}\left[[\mathbf{n}\cdot\mathbf{m}(\Omega)]^2\rho[\mathbf{n}\cdot\mathbf{m}(\Omega)]^2 - \frac{1}{2}\left\{|\mathbf{n}\cdot\mathbf{m}(\Omega)|^4,\rho\right\}\right], \tag{3.35b}$$

with the diffusion coefficients

$$D^{(1)} = \frac{\gamma_1\hbar A^2}{6} \quad \text{and} \quad D^{(2)} = \frac{2\gamma\hbar^2}{15}(B_\perp - B_\parallel)^2. \tag{3.36}$$

Carrying out the integration, we obtain a more compact form for the superoperators

$$\mathcal{L}_1 = \frac{2D^{(1)}}{\hbar^2}[\mathbf{m}(\Omega)\cdot\rho\mathbf{m}(\Omega) - \rho], \tag{3.37a}$$

$$\mathcal{L}_2 = \frac{D^{(2)}}{\hbar}\mathrm{tr}\left[\mathbf{m}(\Omega)\otimes\mathbf{m}(\Omega)\rho\mathbf{m}(\Omega)\otimes\mathbf{m}(\Omega) - \frac{1}{2}\{(\mathbf{m}(\Omega)\otimes\mathbf{m}(\Omega))^2,\rho\}\right]. \tag{3.37b}$$

The corresponding localization rates $F_1(\Omega,\Omega')$ and $F_2(\Omega,\Omega')$ read

$$F_1(\Omega,\Omega') = \frac{2D^{(1)}}{\hbar^2}\left[1 - \mathbf{m}(\Omega)\cdot\mathbf{m}(\Omega')\right], \tag{3.38a}$$

$$F_2(\Omega,\Omega') = \frac{D^{(2)}}{\hbar}|\mathbf{m}(\Omega)\times\mathbf{m}(\Omega')|^2. \tag{3.38b}$$

The localization rate (3.38a) increases with increasing angle between the two orientations $\mathbf{m}(\Omega)$ and $\mathbf{m}(\Omega')$ and obtains its maximum at an angle of π between the two vectors, while the localization rate (3.38b) increases with the squared sinus of the angle between the two orientation vectors with a maximum at $\pi/2$.

Angular Momentum Diffusion of Planar Rotations

An even simpler rotor than the linear rigid rotor is the planar rotor. Its motion is restricted to a motion in a plane and so it has only one orientational degree of freedom α. The orientation of the rotor in then characterized by the vector $\mathbf{e}_\rho(\alpha) = (\cos\alpha, \sin\alpha, 0)^T$.

In order to obtain the superoperators $\mathcal{L}_1\rho$ and $\mathcal{L}_2\rho$ we replace the vector $\mathbf{m}(\Omega)$ in the expressions (3.35a) and (3.35b) with the vector $\mathbf{e}_\rho$ and integrate over the polar angle φ,

$$\mathcal{L}_1\rho = \frac{2D^{(1)}}{\pi\hbar^2}\int_0^{2\pi}\mathrm{d}\varphi\left[\cos(\alpha-\varphi)\rho\cos(\alpha-\varphi)-\frac{1}{2}\left\{\cos^2(\alpha-\varphi),\rho\right\}\right], \tag{3.39a}$$

$$\mathcal{L}_2\rho = \frac{2D^{(2)}}{\pi\hbar^2}\int_0^{2\pi}\mathrm{d}\varphi\left[\cos^2(\alpha-\varphi)\rho\cos^2(\alpha-\varphi)-\frac{1}{2}\left\{\cos^4(\alpha-\varphi),\rho\right\}\right]. \tag{3.39b}$$

The corresponding localization rates read

$$F_1(\alpha,\alpha') = \frac{4D^{(1)}}{\hbar^2}\sin^2\left(\frac{\alpha-\alpha'}{2}\right), \tag{3.40a}$$

$$F_2(\alpha,\alpha') = \frac{D^{(2)}}{\hbar^2}\sin^2(\alpha-\alpha'). \tag{3.40b}$$

For an illustration of the rotational quantum dynamics of planar rotors I use the Wigner-Weyl formalism. In the following, I assume $D^{(2)}=0$ and consider only the superoperator $\mathcal{L}_1\rho$ with $D^{(1)}\equiv D$. Thus, the rotational dynamics is described by

$$\partial_t\rho = \frac{1}{i\hbar}\left[\frac{p_\alpha^2}{2I},\rho\right]+\mathcal{L}_1\rho. \tag{3.41}$$

We transform this equation with the Wigner-Weyl formalism in phase space starting with the unitary time evolution. Inserting the unitary part of equation (3.41) into the equation for the auxiliary function (2.39) leads to [61]

$$\begin{aligned}\partial_t^{\mathrm{u}}w_\nu(\alpha,t) =& \frac{1}{2\pi}\frac{1}{2i\hbar I}\sum_{m'=-\infty}^{\infty}e^{-2i(m'+\mu/2)\alpha}\\ &\langle\nu-(m'+\mu/2)|[\mathsf{p}_\alpha^2,\rho]|\nu+m'+\mu/2\rangle,\end{aligned} \tag{3.42}$$

where I replaced $m+\mu/2=\nu$. Due to the commutator the p_α operator acts on the momentum states $\langle\nu-(m'+\mu/2)|$ and $\langle\nu+m'+\mu/2|$ and we obtain [61]

$$\begin{aligned}\partial_t^{\mathrm{u}}w_\nu =& -\frac{2}{2\pi}\frac{\hbar}{iI}\sum_{m'=-\infty}^{\infty}\nu(m'+\mu/2)e^{-2i(m'+\mu/2)\alpha}\\ &\times\langle\nu-(m'+\mu/2)|\rho|\nu+m'+\mu/2\rangle.\end{aligned} \tag{3.43}$$

The term $(m'+\mu/2)$ can be expressed in terms of an α-derivative so that we can identify the auxiliary function $w_\nu(\alpha,t)$

$$\partial_t^{\mathrm{u}}w_\nu(\alpha,t) = \frac{\hbar}{I}\nu\partial_\alpha w_\nu(\alpha,t). \tag{3.44}$$

For the transformation of the incoherent part we use the angle representation of the auxiliary function (2.38) and the expression (3.40a)

$$\partial_t^{\mathrm{i}} w_\nu(\alpha,t) = -\frac{2D}{\hbar^2\pi}\int_{-\pi}^{\pi} \mathrm{d}\alpha'\; e^{-2i\alpha'\nu}\sin^2(\alpha-\alpha)\langle\alpha+\alpha'|\rho|\alpha-\alpha'\rangle. \tag{3.45}$$

After expressing the sine-function in terms of exponential functions we can identify the equation [61]

$$\partial_t^{\mathrm{i}} w_\nu(\alpha,t) = \frac{D}{\hbar^2}[w_{\nu+1}(\alpha,t) - 2w_\nu(\alpha,t) + w_{\nu-1}(\alpha,t)]. \tag{3.46}$$

The superoperator $\mathcal{L}_1$ has the form of a discrete second-order angular momentum derivative in phase space. Combining the equations (3.44) for the unitary time evolution and (3.46) for the incoherent part of the time evolution we obtain an equation of motion for the auxiliary function

$$\partial_t w_\nu(\alpha,t) = -\frac{\nu\hbar}{I}\partial_\alpha w_\nu(\alpha,t) + \frac{D}{\hbar}\left[w_{\nu+1}(\alpha,t) - 2w_\nu(\alpha,t) + w_{\nu-1}(\alpha,t)\right]. \tag{3.47}$$

We can find an analytical solution for this equation. We start with the ansatz

$$w_{m+\mu/2}(\alpha,t) = \frac{1}{2\pi}\sum_{k\in\mathbb{Z}}\int \mathrm{d}\gamma f(k,\gamma,t)\exp\left[i\left(\alpha - \frac{\hbar(m+\mu/2)t}{I}\right)k - im\gamma\right]. \tag{3.48}$$

Setting $t=0$ we see that the function $w_{m+\mu/2}(\alpha,0)$ is the Fourier transformation of the function $f(k,\gamma,0)$. Inserting the ansatz (3.48) in the equation of motion (3.47) leads to an ordinary differential equation for $f(k,\gamma,t)$

$$\partial_t f(k,\gamma,t) = -\frac{4D}{\hbar^2}\sin^2\left(\frac{\gamma}{2} + \frac{\hbar k t}{2}\right) f(k,\gamma,t), \tag{3.49}$$

with the solution

$$f(k,\gamma,t) = f(k,\gamma,0)\exp\left[-\frac{4D}{\hbar}\int_0^t \mathrm{d}t'\;\sin^2\left(\frac{\gamma}{2} + \frac{\hbar k t}{2}\right)\right]. \tag{3.50}$$

Now we have to express the function $f(k,\gamma,0)$ in terms of the initial auxiliary functions $w_{m+\mu/2}(\alpha,0)$ by using the inverse Fourier transformation

$$f(k,\gamma,0) = \frac{1}{2\pi}\sum_{m\in\mathbb{Z}}\int_{-\pi}^{\pi}\mathrm{d}\alpha\; w_{m+\mu/2}(\alpha,0)e^{im\gamma - i\alpha k}. \tag{3.51}$$

Inserting this into (3.50) carrying out the integration over in the exponential function

I obtain the solution $w_{m+\mu/2}(\alpha,t)$ of the equation of motion (3.47)

$$w_{m+\mu/2}(\alpha,t)=\int_{-\pi}^{\pi}\mathrm{d}\alpha' \sum_{m'\in\mathbb{Z}} w_{m'+\mu/2}(\alpha',0)T(\alpha-\alpha';m,m';t), \tag{3.52}$$

with the propagator

$$\begin{aligned} T(\alpha-\alpha';m,m';t)=&\frac{1}{4\pi^2}e^{-2Dt/\hbar^2}\sum_{k\in\mathbb{Z}} e^{ik(\alpha-\alpha')}e^{-i\hbar(m+\mu/2)tk/I}\int \mathrm{d}\gamma e^{-i\gamma(m-m')} \\ &\times \exp\left[\frac{4DI}{k\hbar^3}\sin\left(\frac{\hbar kt}{2I}\right)\cos\left(\gamma+\frac{\hbar kt}{2I}\right)\right]. \end{aligned} \tag{3.53}$$

This propagator depends only on the difference between the initial and final angle, and on the intial and final momentum. After the substitution $\gamma'=\gamma+\hbar kt/(2I)$ we can carry out the γ-integration and obtain

$$\begin{aligned} T(\alpha-\alpha';m,m';t)=&\frac{1}{2\pi}e^{-2Dt/\hbar}\sum_{k\in\mathbb{Z}}\exp\left[ik\left(\alpha-\alpha'-\frac{\hbar t}{I}\frac{m+m'+\mu}{2}\right)\right] \\ &\times I_{m-m'}\left[\frac{2Dt}{\hbar^2}\mathrm{sinc}\left(\frac{\hbar kt}{2I}\right)\right]. \end{aligned} \tag{3.54}$$

Substituting $\ell=m-m'$ and $\alpha''=\alpha-\alpha'-\hbar t(m+\mu/2)/I$ results in the compact solution

$$w_{m+\mu/2}(\alpha,t)=\sum_{\ell\in\mathbb{Z}}\int_{-\pi}^{\pi}\mathrm{d}\alpha''\ w_{m+\mu/2-\ell}\left(\alpha-\alpha''-(m+\mu/2)\frac{\hbar t}{I},0\right)\tilde{T}(\alpha'',\ell;t) \tag{3.55}$$

with the propagator

$$\tilde{T}(\alpha'',\ell;t)=\frac{1}{2\pi}e^{-2Dt/\hbar}\sum_{k\in\mathbb{Z}}e^{ik(\alpha''-\hbar t\ell/2)}I_\ell\left[\frac{2Dt}{\hbar^2}\mathrm{sinc}\left(\frac{\hbar kt}{2I}\right)\right] \tag{3.56}$$

Equation (3.52) together with the propagator (3.54) give us a compact solution of the equation of motion (3.47). In the following, I will discuss this solution in more detail and use it to evolve an exemplary initial state. At first let us verify that the propagator preserves the normalization of the Wigner function. For that one must show that the relation

$$\int_{-\pi}^{\pi}\mathrm{d}\alpha''\sum_{\ell\in\mathbb{Z}}\tilde{T}(\alpha'',\ell;t)=1 \tag{3.57}$$

is fulfilled. The integration over α'' results in a Kronecker delta δ_{k0}. After using the relation $\sum_{\ell=-\infty}^{\infty} I_\ell(z) = e^z$ [72] we see that the propagator (3.56) indeed obeys the relation (3.57).

In case of vanishing diffusion, $D = 0$, the modified Bessel function turns into a Kronecker delta $I_\ell(0) = \delta_{\ell 0}$. With this the equation (3.55) simplifies so that we can carry out the sum over k and ℓ and the α''-integration with the result

$$w_{m+\mu/2}(\alpha, t) = w_{m+\mu/2}[\alpha - \hbar t(m + \mu/2)/I, 0]. \tag{3.58}$$

This equation describes a shearing of the initial state similar to the classical dynamics. Due to the 2π-periodicity of the auxiliary functions and the discrete values of m the initial state reappears at integer multiples of the revival time $T_{\mathrm{rev}} = 4\pi I/\hbar$. I apply equation (3.55) now on the initial state $\psi_0(\alpha) \propto \exp[-\cos^2\alpha/(4\sigma^2)]$ which is a spatial superposition of two wave packets loclized at $\alpha = \pm\pi/2$. Inserting this into equation (2.38) and using the relations $\cos(2\alpha) = 2\cos^2\alpha - 1$ and $\exp(z\cos\theta) = \sum_{k\in\mathbb{Z}} I_k(z)\exp(ik\theta)$ leads to the respective auxiliary function

$$w_{m+\mu/2}(\alpha, 0) = \frac{1}{N\pi} \sum_{k=-\infty}^{\infty} (-1)^k I_k \left[\frac{\cos(2\alpha)}{4\sigma^2}\right] \int_{-\pi}^{\pi} \mathrm{d}\alpha' e^{-2i(m+\mu/2-k)\alpha'}. \tag{3.59}$$

The integration over α' yields a Kronecker delta $\delta_{m+\mu/2,k}$. Here, we see that only the auxiliary function with $\mu = 0$ contributes because m and k are integers. The initial auxiliary function reads

$$w_m(\alpha, 0) = \frac{2(-1)^m}{N} I_m \left[\frac{\cos(2\alpha)}{4\sigma^2}\right], \tag{3.60}$$

with the constant $N = 2\pi I_0(1/(4\sigma^2))$. Note that the auxiliary function itself is not normalized to one but the Wigner function is. The numerical evolution of the time evolution via the equation (3.55) is illustrated in Fig. 3.4. We can see the two initially localized wave packets at $\alpha = \pm\pi/2$ and the interference pattern in between. The angular momentum distribution shows that initially only even m are occupied. The unitary time evolution leads to shearing while the interaction with the environment quickly turns the superposition into a classical mixture once the interference pattern has vanished. On longer timescales the interaction leads to a broadening of the angular momentum distribution, i.e. to angular momentum diffusion.

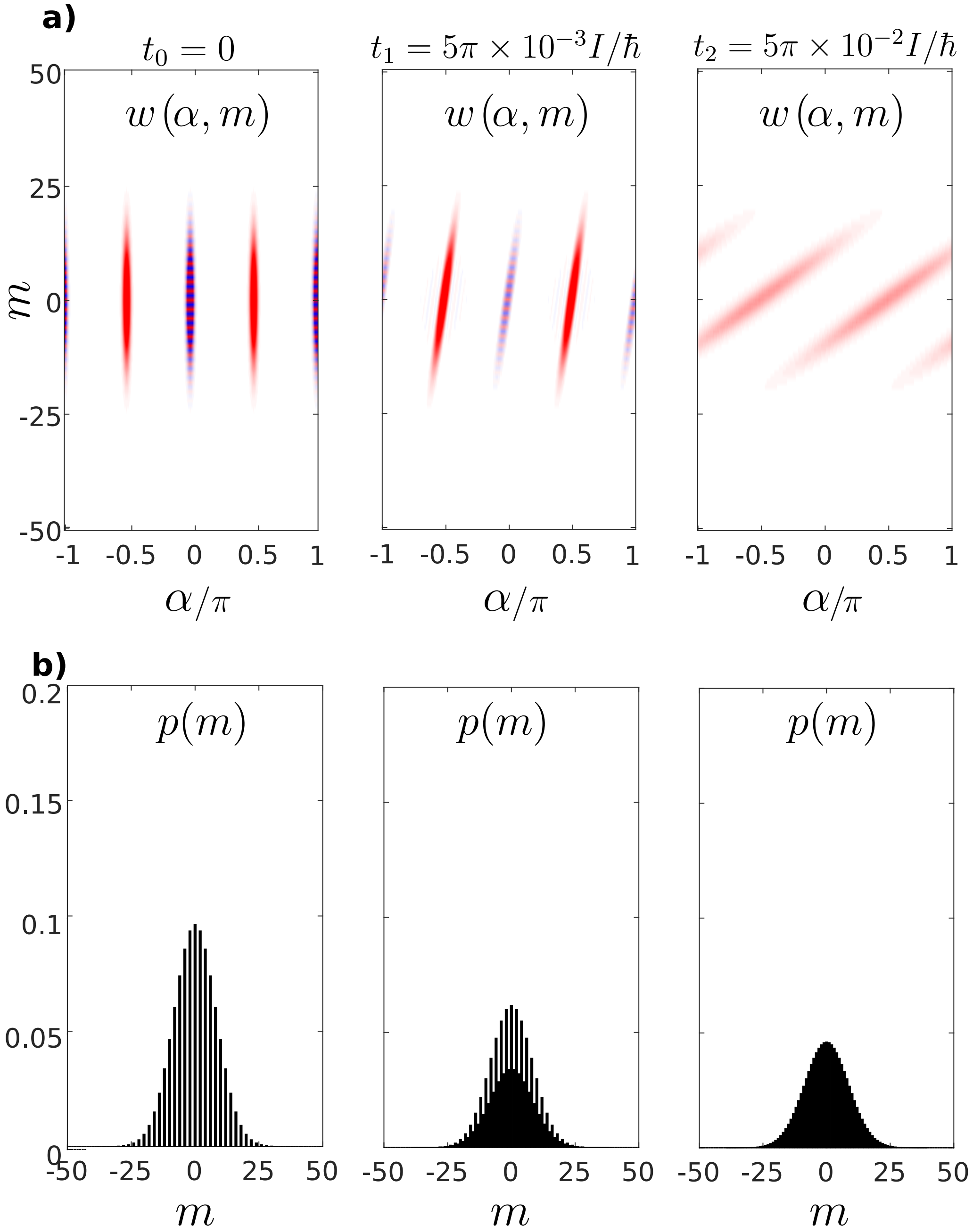

Figure 3.4.: Time evolution of a planar rotor under angular momentum diffusion, as described by equation (3.41). The initial state $\psi(\alpha) \propto \exp(-\cos^2\alpha/(4\sigma^2))$ with $\sigma = 0.06$ is a superposition of two wave packets located at $\alpha = \pm\pi/2$. Panels a) show density plots of the Wigner function $W(\alpha, m, t)$ for the times $t = 0$, $t = 5\pi \times 10^{-3} I\hbar$ and $t = 5\pi \times 10^{-2} I\hbar$. In b) we see the respective angular moment distributions. Note that initially only even angular momentum states are occupied. For the times t_1 and t_2 we observe the shearing of the initial state, a decreasing of the interference pattern around $\alpha = 0$ and a occupation of odd angular momentum states.

4. Orientational Quantum Revivals of Nanoscale Particles

Observing quantum phenomena on macroscopic scales is still a challenging task. While there are several proposals for macroscopic quantum tests with spherical nanoparticles [13, 14] in Ref. [45] we propose a new way for testing the superposition principle involving the orientational degrees of freedom of nanoscale aspherical particles. This superposition test exploits the quantized angular momentum of free evolving rigid rotors. We assume a nanorod thin enough to be approximated as a linear rigid rotor characterized by the moment of inertia I. Then the Hamiltonian takes the form (2.28) and the unitary time evolution operator $\mathsf{U}(t)$ for the free orientational dynamics can be expanded as

$$\mathsf{U}(t) = e^{-i\mathsf{H}t/\hbar} = \sum_{j\in\mathbb{N}_0} \sum_{m=-j}^{j} e^{-i\hbar j(j+1)t/(2I)} |jm\rangle\langle jm|. \tag{4.1}$$

Since the term $j(j+1)$ is always an even integer, this time evolution operator reduces to the unity operator for all integer multiples of the revival time

$$T_{\text{rev}} = 2\pi I/\hbar. \tag{4.2}$$

At this revival time the angular momentum state with the smallest angular momentum, $j = 1$, performs one complete rotation and all higher angular momenta perform full rotations as well. Thus, at this time the phase between different angular momentum states vanishes and as a consequence the collective interference of all occupied angular momentum states leads to a reappearance of the initial state. This is an effect of the free time evolution and it is based on the discrete angular momenta. It has no analogue in classical or center of mass physics.

For an initial state with a specific orientation for a tightly aligned rod these orientational quantum revivals can be exploited for testing the superposition principle. They have already been discussed and observed for molecules [17, 22] and in this chapter I propose an experimental set up for observing the revivals with nanoscale particles on much larger mass, length and time scales. This set up makes use of the great progress in the field of levitated optomechanics with aspherical particles. It does not require any diffraction grating and uses only a single dielectric nanorod and differs crucially from quantum experiments with center of mass motion.

At first, I introduce the revival scheme and explain the single steps. Later, I discuss the feasibility of the set up with silicon nanorods and nanoscale carbon nanotubes, and show simulations of the time evolution under realistic environmental conditions. The results of this chapter are published in Ref. [45].

4.1. The Revival Scheme

The here proposed revival scheme consists of cycles with four main steps which are illustrated in figure 4.2 :

- **alignment**
  In the first step the nanorotor is trapped in a linearly polarized optical tweezer and the rotor's librations are cooled. So the symmetry axis $\mathbf{m}(\Omega)$ of the rotor aligns with a space-fixed direction, the polarization $\boldsymbol{\epsilon}$ of the laser beam. Thus, an initial state with a specific orientation and a superposition of several angular momentum states is created. The initial state is characterized by its alignment, $\langle[\mathbf{m}(\Omega)\cdot\boldsymbol{\epsilon}]^2\rangle$

- **free fall**
  After the optical tweezer is switched off the center of mass of the particle drops and the orientation state disperses quickly into a uniform distribution. There it remains the most of the time except for multiple integers of the revival time.

- **revival**
  At the revival time the initial state and with this the initial alignment reappears briefly on a timescale much smaller than the revival time. The alignment can be measured by collecting the scattered light of a probe beam with the same polarization direction as the tweezer laser. The intensity of scattered light is proportional to the relative orientation between the symmetry axis $\mathbf{m}(\Omega)$ and the polarization $\boldsymbol{\epsilon}$.

- **recapture**
  After measuring the alignment the tweezer laser is switched on and recaptures the nanorotor. With this the particle is recycled and can be used for another run of the experiment. By running the experiment thousands of times and measuring the alignment at the same time one obtains a statistical distribution of the alignment. For most points in time we should obtain an evenly

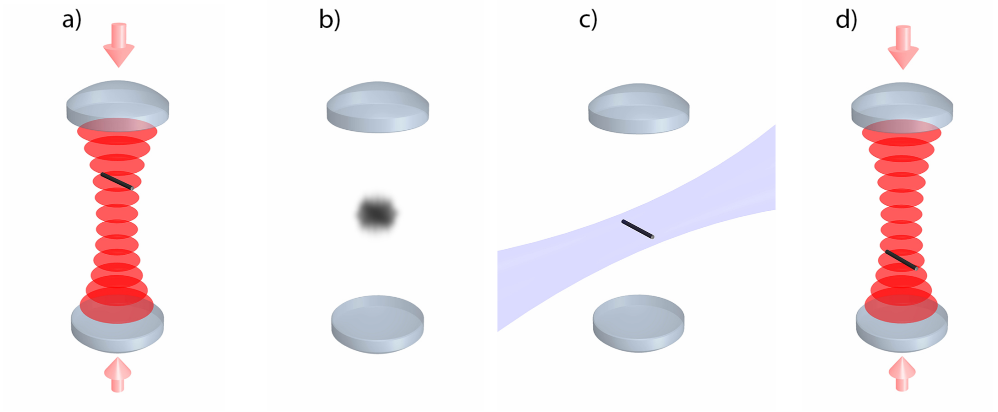

Figure 4.1.: Illustration of the four steps of the here proposed revival scheme: a) the rotor is trapped in an optical tweezer and cavity or feedback cooling the orientational degrees of freedom to subkelvin temperatures leads to a tight alignment with the polarization direction of the trapping laser. b) After the trapping laser is turned off the particle drops in the gravitational field and the orientational state evolves freely. The quantum state quickly disperses in a superposition of all possible orientations. c) At multiple integers of the revival time $T_{\text{rev}} = 2\pi I\hbar$ the collective interference of all occupied rotation states leads to a brief reappearance of the initial state. d) The rotor is recaptured by the trapping laser and recycled to repeat this measurement several times with the same particle. Figure taken from [45].

distributed alignment, but at the revival time one should observe a much more narrow distribution of the alignment. Thus the interference signal is characterized by the width of the alignment distribution. It can be represented by the expectation value $\langle[\mathbf{m}(\Omega)\cdot\boldsymbol{\epsilon}]^2\rangle$.

For the following discussion I consider a dielectric linear rigid rotor of length ℓ, mass M, moment of inertia $I = M\ell^2/12$ and the polarizability tensor $\alpha_0 = \text{diag}(\alpha_\perp, \alpha_\perp, \alpha_\parallel)$ in the body-fixed system. Here, $\alpha_\perp$ and $\alpha_\parallel$ denotes the polarizability perpendicular and parallel to the symmetry axis of the rotor. Thus, the particle has an anisotropy in the polarizability of $\Delta\alpha = \alpha_\parallel - \alpha_\perp$. The rotor is optically levitated by an optical tweezer, consisting of two counter-propagating linear polarized laser beams of power P and polarization direction $\boldsymbol{\epsilon}$. They form a standing laser wave of waist w. The tweezer is aligned with the gravitational field. When the tweezer is turned off the particle drops along the tweezer axis. The space-fixed $\mathbf{e}_3$-axis is aligned with the polarization direction $\boldsymbol{\epsilon}$ of the tweezer.

4.1.1. Alignment

Optical potential

Due to the anisotropic polarizability of the dielectric particle a standing laser wave creates an orientation dependent optical potential. For the calculation of this potential we start with the electric field $\mathbf{E}_{\rm sw}$ of the standing laser wave

$$\mathbf{E}_{\rm sw}(\mathbf{r},t) = E_0 e^{-i\omega t} f(y,z)\cos(kx)\mathbf{e}_3, \tag{4.3}$$

with $f(y,z)$ the transverse mode profile and the wave number k. In the following we assume a symmetric Gaussian transverse mode profile $f(y,z) = \exp[-(x^2+y^2)/w^2]$. The optical potential of a dielectric particle evolving in an electric field is given by [73]

$$V(\mathbf{r},\Omega) = -\frac{1}{4}\mathbf{E}_{\rm sw}(\mathbf{r})\alpha(\Omega)\mathbf{E}_{\rm sw}(\mathbf{r}), \tag{4.4}$$

with the orientation dependent polarizability tensor $\alpha(\Omega) = \mathsf{R}(\Omega)\alpha_0\mathsf{R}(\Omega) = \alpha_\perp\mathbb{1} + (\alpha_\parallel - \alpha_\perp)\mathbf{m}(\Omega)\otimes\mathbf{m}(\Omega)$. Inserting the electric field (4.3) into the optical potential (4.4) we obtain

$$V(\mathbf{r},\Omega) = -\frac{1}{4}|E_0|^2 f^2(y,z)\cos^2(kx)\left[\Delta\alpha[\mathbf{m}(\Omega)\cdot\mathbf{e}_3]^2 + \alpha_\perp\right]. \tag{4.5}$$

In the following we are interested in the orientation dependence of the optical potential and thus, we assume the particle to be in the minimum of the potential for the three center of mass degrees of freedom, $x = y = z = 0$. The relation between intensity $I(x=0,y=0,z=0) = \varepsilon c|E_0|^2$ and laser power P is $I(0,0,0) = 8P/A$ with the spot area $A = \pi w^2/2$ for a Gaussian beam. With $\mathbf{m}(\Omega)\cdot\mathbf{e}_3 = \cos\beta$ the azimuthal symmetric orientation dependent part of the optical potential 4.5 reads

$$V(\beta) = -V_0\cos^2\beta \tag{4.6}$$

with $V_0 = 4\Delta\alpha P/\pi c\varepsilon_0 w^2$.

Initial state

Feedback [31] or cavity cooling [30] of the orientational degrees of freedom of the trapped particle leads to a tight alignment along the polarization direction of the tweezer. We can quantify the initial alignment by

$$\langle\cos^2\beta\rangle_0 = \mathrm{tr}\left\{\rho_0\cos^2\beta\right\}. \tag{4.7}$$

Here, ρ_0 is the initial state, which is the thermal state characterized by its librational temperature T, and takes the form

$$\rho_0 = \frac{1}{Z} e^{-\mathsf{H}/k_B T}, \tag{4.8}$$

with the Hamiltonian

$$\mathsf{H} = \mathsf{J}^2/(2I) - V_0 \cos^2 \upbeta, \tag{4.9}$$

and the partition function Z. For calculating the initial alignment we represent both, the initial state and the cosine of the β-operator, in the angular momentum representation, i.e. in the eigenbasis of the free flight Hamiltonian of the linear rigid rotor.

Numerical Implementation

In a first step, we calculate the matrix elements $\langle jm| \cos^2 \upbeta |j'm'\rangle$ by inserting two unity operators in the Euler angle basis (2.12). With the Euler angle representation of the eigenstates $|jm\rangle$ (2.30) and the orthogonal relation of the angle states we get

$$\langle jm| \cos^2 \upbeta |j'm'\rangle = \int_0^{2\pi} \mathrm{d}\alpha \int_0^{\pi} \mathrm{d}\beta \, \sin\beta \, Y_j^{m*}(\beta,\alpha) Y_{j'}^{m'}(\beta,\alpha) \cos^2\beta. \tag{4.10}$$

We can express the squared cosine-function by spherical harmonics as $\cos^2\beta = 1/3 + 4\sqrt{\pi/5}Y_2^0(\beta,\alpha)/3$. The integral of the product of three spherical harmonics over the whole sphere can be expressed in terms of Wigner 3-j symbols $\begin{pmatrix} j_1 & j_2 & j_3 \\ m_1 & m_2 & m_3 \end{pmatrix}$ and we obtain [72]

$$\begin{aligned}\langle jm| \cos^2 \upbeta |j'm'\rangle =& \frac{1}{3}\delta_{jj'}\delta_{mm'} + (-1)^m \frac{2}{3}\sqrt{(2j+1)(2j'+1)} \\ &\times \begin{pmatrix} j' & 2 & j \\ 0 & 0 & 0 \end{pmatrix} \begin{pmatrix} j' & 2 & j \\ m' & 0 & -m \end{pmatrix}.\end{aligned} \tag{4.11}$$

Since Wigner 3-j symbols are directly linked to Clebsch Gordan coefficients [72] they obey certain selection rules implying that the expression (4.11) vanishes except for $m = m'$ and $j = j'$ or $j = j' \pm 2$.

Adding the matrix elements $\langle jm|\mathsf{J}^2/2I|j'm'\rangle = \hbar^2 j(j+1)/2I\delta_{jj'}\delta mm'$ to equation (4.11) we obtain the matrix elements of the Hamiltonian H. By a numerical diagonalization of this Hamiltonian we get its eigenvalues E_n and eigenstates $|\psi_n\rangle$ in the angular momentum representation.

The initial state ρ_0 can be written as

$$\rho_0 = \sum_n e^{-E_n/k_bT} \sum_{j\in\mathbb{N}_0} \sum_{m=-j}^{j} \sum_{j'\in\mathbb{N}_0} \sum_{m'=-j'}^{j'} c_{jm}^{(n)*} c_{j'm'}^{(n)} |jm\rangle\langle j'm'|, \tag{4.12}$$

with $c_{jm}^{(n)} = \langle jm|\psi_n\rangle$.

For the numerical diagonalization the subscripts j and m are mapped onto a joint index i of a one dimensional array of length $(j_{\max}+1)^2$ with $i(j,m) = (j+1)^2 - j + m$ and $j_{\max}$ the highest contributing quantum number j. This way the Hamiltonian $\mathsf{H}_{jmj'm'}$ is implemented as a $(j_{\max}+1)^2 \times (j_{\max}+1)^2$ matrix with elements $\mathsf{H}_{ii'}$. We have to truncate the matrix at a certain $j_{\max}$ for the simulations and ensure that the results do not depend on this cutoff-parameter. In this way I proceed throughout this thesis.

This exact diagonlization becomes more and more intractable for increasing quantum numbers j, because the number of required matrix elements increases with $(j+1)^4$. Since millions of angular momentum states are occupied for realistic particles, we must resort to semiclassical methods shown in section 2.4.4 to calculate the matrix elements of ρ_0 in the $|jm\rangle$ basis.

Semiclassical Matrix Elements

To calculate the matrix elements of the initial state semiclassically one writes the initial state ρ_0 (4.8) in terms of the action-angle variables (2.69) yielding the semiclassical operator

$$\rho_0(\mathsf{J}, \mathsf{M}, \alpha_J, \alpha_M) = \exp\left[\frac{\mathsf{J}^2}{2I} - V_0 \cos^2\alpha_J \left(1 - \frac{\mathsf{M}^2}{(\mathsf{J}+1/2)^2}\right)\right]. \tag{4.13}$$

Inserting this semiclasscial operator for the initial state ρ_0 into the formula (2.72) and carrying out the integrations over α_j and α_m leads to

$$\begin{aligned}\langle jm|\rho_0|j'm'\rangle \approx{}& \frac{1}{Z}\exp\left[-\hbar^2\frac{(\bar{j}+1/2)^2}{2Ik_BT}\right]\exp\left[\frac{V_0}{2k_BT}\left(1-\frac{m^2}{(\bar{j}+1/2)^2}\right)\right] \\ &\times I_{(j-j')/2}\left[\frac{V_0}{2k_BT}\left(1-\frac{m^2}{(\bar{j}+1/2)^2}\right)\right]\delta_{mm'},\end{aligned} \tag{4.14}$$

for $j-j'$ even and 0 for $j-j'$ odd. Here, $I_n(.)$ denotes the modified Bessel function of order n. The partition function Z is given by the trace over the operator $e^{-\mathsf{H}/k_BT}$

$$\begin{aligned} Z =& e^{V_0/(2k_BT)} \sum_{j\in N_0} \sum_{m=-j}^{j} e^{-\hbar^2(j+1/2)^2/(2Ik_BT)} \exp\left[-\frac{V_0}{k_BT}\frac{m^2}{(j+1/2)^2}\right] \\ &\times I_0\left[\frac{V_0}{2k_BT}\left(1-\frac{m^2}{(j+1/2)^2}\right)\right]. \end{aligned} \tag{4.15}$$

To evaluate this approximately we replace the modified Bessel function by its asymptotic expansion [72] $I_0(z)\approx e^z/\sqrt{2\pi z}$ for large arguments z and replace the sum over j by an integral over j from 0 to ∞ and the sum over m by an integral over m from $-j$ to j

$$\begin{aligned} Z \approx& e^{V_0/(k_BT)} \int_0^\infty \mathrm{d}j\, e^{-\hbar^2(j+1/2)^2/(2k_BTI)} \int_{-j}^{j} \mathrm{d}m\, \exp\left[-\frac{V_0}{k_BT}\frac{m^2}{(j+1/2)^2}\right] \\ &\times \left[\frac{\pi V_0}{k_BT}\left(1-\frac{m^2}{(j+1/2)^2}\right)\right]^{-1/2}. \end{aligned} \tag{4.16}$$

First one can solve the integration over m with help of the substitution $\xi = m/(j+1/2)$ where we approximate the resulting integration borders with -1 and 1, which is well allowed for large j. The resulting modified Bessel function is again approximated by its asymptotic expression $I_0(z)\approx e^z/\sqrt{2\pi z}$. For the integration over j we substitute $u=j+1/2$, yielding

$$Z \approx \frac{k_BT\exp(V_0/k_BT)}{V_0}\int_0^\infty \mathrm{d}u\, u\, e^{\hbar^2u^2/(2Ik_BT)} = \frac{\exp(V_0/k_BT)k_B^2T^2I}{V_0\hbar^2}. \tag{4.17}$$

Inserting the expression (4.17) for the partition function Z in equation (4.14) leads to resulting matrix elements of the initial state (4.8) in the Bohr-Sommerfeld approximation

$$\begin{aligned} \langle jm|\rho_0|j'm'\rangle \approx& \frac{V_0\hbar^2}{k_B^2T^2I} e^{-\hbar^2(\bar{j}+1/2)^2/(2Ik_BT)} \exp\left[-\frac{V_0}{k_BT}\frac{m^2}{(\bar{j}+1/2)^2}\right] \\ &\times \exp\left[-\frac{k_BT}{V_0(1-m^2/(j+1/2)^2}\left(\frac{j-j'}{2}\right)^2\right] \\ &\times \left[\frac{\pi V_0}{k_BT}\left(1-\frac{m^2}{(j+1/2)^2}\right)\right]^{-1/2} \end{aligned} \tag{4.18}$$

where I use the approximation [72]

$$I_n(z) \approx \frac{e^z}{\sqrt{2\pi z}} e^{-n^2/(2z)}, \tag{4.19}$$

for modified Bessel function of order n and $z \gg 1$ and thus it is valid for deeply trapped initial states with $k_B T/V_0 \ll 1$.

Properties of the Initial State

With the semiclassical matrix elements of the initial state (4.18) we can calculate the time evolution of the alignment numerically even when millions of angular momentum states are occupied. Crucial for a good visibility of the revival signal is a high initial alignment. Even though we can calculate the initial alignment for a certain potential depth, moment of inertia and temperature numerically it is helpful to have available analytically approximated formula showing the dependence on this three quantities.

To this end we express the initial alignment $\mathrm{tr}(\rho_0 \cos^2 \beta)$ of a rotor in the potential $V(\beta) = -V_0 \cos^2 \beta$ in terms of the partition function Z (4.17)

$$\langle \cos^2 \beta \rangle_0 = k_B T \frac{\partial}{\partial V_0} \ln Z. \tag{4.20}$$

With the expression (4.17) for the partition function Z one obtains

$$\langle \cos^2 \beta \rangle \approx 1 - \frac{k_B T}{V_0}, \tag{4.21}$$

which is valid in the deep trapping regime $k_B T/V_0 \ll 1$. Here, it is obvious that the initial alignment increases with decreasing librational temperatur T and increasing potential depth V_0. In the following I compare this result for the initial alignment with the result for a classical probability distribution function

$$f_0(\alpha, \beta, p_\alpha, p_\beta) = \frac{1}{Z'} e^{-H(\alpha,\beta,p_\alpha,p_\beta)/(k_B T)}. \tag{4.22}$$

After carrying out the integrals over the canonical momenta p_α and p_β and the azimuthal angle α, the probability distribution function for the polar angle β reads $f(\beta) = \sin\beta \exp[V_0 \cos^2 \beta/(k_B T)]/Z''$, yielding the classical initial alignment

$$\langle \cos^2 \beta \rangle_0 = \int_0^\pi \mathrm{d}\beta \cos^2 \beta f(\beta) \approx 1 - \frac{k_B T}{V_0}, \tag{4.23}$$

in the limit $k_B T/V_0 \ll 1$. We see that this result is identical to our semiclassical result for the alignment (4.21)

The initial state is characterized not only by its initial alignment but also by the expectation value of the total angular momentum quantum number $\langle j \rangle_0 = \sum_{j \in \mathbb{N}_0} j p(j)$. It determines mainly the free rotational time evolution. In addition, it influences the duration of the numerical simulations, the larger the expectation value the more angular momentum states we have to consider in the calculation and the longer the calculation time. We obtain the distribution $p(j)$ from the semiclassical matrix elements of the initial state by a summation over m. Multiplying it with j and integrating over j with the approximation $j + 1/2 \approx j$ for large j leads to

$$\langle j \rangle_0 \approx \frac{1}{Z'} \int_0^\infty j^2 e^{-\hbar^2 j^2/(2Ik_BT)} = \sqrt{\frac{\pi I k_B T}{2\hbar^2}}. \tag{4.24}$$

The expectation value of the total angular momentum quantum number increases with the square root of the temperature T and the moment of inertia I as is consistent with $\hbar^2 j_0^2/2I \propto k_B T$

4.1.2. Free Fall

After the trapping laser is turned off, the center of mass of the particle drops in the gravitational field along the tweezer axis while the orientation of the particle evolves freely. This quickly leads to a dispersion of the initially tightly aligned orientational wave packet, a delocalization of the state. In addition to this unitary process, we have to consider orientational decoherence processes which can suppress the revivals. In a first step, we examine the dispersion and later we discuss decoherence effects.

Unitary Time Evolution

Considering only the unitary (decoherence-free) time evolution the matrix elements of the time dependent state operator read in the angular momentum representation

$$\begin{aligned} \langle jm|\rho_\mathrm{u}(t)|j'm'\rangle = \sum_{j,j'\in\mathbb{N}_0} \sum_{m=-j}^{j} \sum_{m'=-j'}^{j'} &\langle jm|\rho_0|j'm'\rangle \\ \times \exp&\left[-\frac{i\hbar}{2I}[j(j+1) - j'(j'+1)]t\right], \end{aligned} \tag{4.25}$$

where the subscript u denotes the unitary time evolution. With this state operator we can calculate the decoherence-free time evolution of the alignment $\langle \cos^2 \beta\rangle_\mathrm{u} = \mathrm{tr}[\rho_\mathrm{u}(t)\cos^2\beta]$.

The dispersion of the initial state leads to a rapid decay of alignment. This dispersion timescale determines also the length of the time period in which the revival occurs and thus the required accuracy for the measurement of the alignment. We can estimate this timescale by calculating the time dependence of the classical alignment of a Gaussian initial state in a flat configuration space. The classical initial state $g(\beta, p_\beta)$ in a potential $V = -V_0 \cos^2 \beta$ is given by

$$g(\beta, p_\beta) = \frac{1}{N} \sin\beta \exp\left(-\frac{p_\beta^2}{2Ik_BT} + V_0 \frac{\cos^2\beta}{k_BT}\right), \tag{4.26}$$

with a normalization constant N. In a flat configuration space the free time evolution leads to a simple shearing in the angle $\beta(t) = \beta_0 + p_\beta t/I$, known also from the free center of mass time evolution. With this approximation one obtains

$$\begin{aligned}\langle\cos^2\beta\rangle_{\mathrm{u}} &\approx \int_0^\beta \mathrm{d}\beta \int_{-\infty}^{\infty} \mathrm{d}p_\beta \cos^2\left(\beta + \frac{p_\beta}{I}t\right) g(\beta, p_\beta) \\ &= \langle\cos^2\beta\rangle_0 e^{-\kappa^2 t^2} + \frac{1}{2}\left(1 - e^{-\kappa^2 t}\right)\end{aligned} \tag{4.27}$$

with the dispersion timescale $\kappa = \sqrt{2k_BT/I}$. This shows that the higher the temperature the faster the alignment decreases. Remembering that the expectation value of the angular momentum increases with the temperature T for a given moment of inertia I we see that a higher number of occupied angular momentum states j leads to faster decay of the alignment.

Further, (4.27) shows that the alignment decays to a value of $\langle\cos^2\beta\rangle = 1/2$. For the classical rotational dynamics it stays there for the rest of the time. In contrast to that, a quantum state stays there for most of the time but at integer multiples of the revival time T_{rev} the value of the initial state alignment (4.21) recurs as follows from equation (4.25).

If we had a uniform distribution of the orientation over the whole surface of a sphere one would expect a substantially lower alignment of $\langle\cos^2\beta\rangle = \int_0^{2\pi} \mathrm{d}\alpha \int_0^{\pi} \mathrm{d}\beta \sin\beta\cos^2\beta/(4\pi) = 1/3$. So why does the dispersion of our initial state not lead to an equally distributed state? In the classical approximation (4.27) we assumed shearing in the polar angle β. This shearing of β leads to a state uniformly distributed on the corresponding great circle. The alignment for such a state is 1/2 and after averaging it over all azimuth angles α it remains at this value. This is still valid for the quantum description. For initial states with increasingly high values of the quantum number m we observe a decreasing of the constant alignment between two revivals from a value of around 1/2 to values of 1/3. Thus, a high angular momentum in $\mathbf{e}_3$-direction leads to a state uniformly distributed on the surface of a sphere due to dispersion.

Decoherence

Having discussed the free unitary rotational dynamics of the rotor, let us now examine the effect of environmental decoherence [41, 42] on the rotor's orientational dynamics. The dominant sources of decoherence are collisions with residual gas particles and thermal emission of photons, as already discussed for other matter wave experiments [13, 14, 67, 74, 75].

In section 3.2 I discussed the Markovian orientational decoherence master equation and below, in section 6.3.2, I solve this master equation numerically. For the present purpose it suffices to obtain a short estimate of the effect of environmental decoherence on the revival signal. I therefore make a very conservative assumption that a single decoherence event, for example a single collision with a gas particle, completely destroys the revival signal by producing a uniformly distributed state ρ_i on the surface of a sphere with $\langle \alpha, \beta | \rho_i | \alpha, \beta \rangle = \frac{1}{4\pi}$. In this case the dynamics of the orientational state can be described by the master equation

$$\partial_t \rho = -\frac{i}{\hbar}[\mathsf{H}_0, \rho] + \Gamma(\rho_i - \rho), \tag{4.28}$$

with the free Hamiltonian (2.28) and the rate of decoherence events Γ. This equation is solved by $\rho(t) = \rho_{\mathrm{u}}(t)\exp(-\Gamma t) + \rho_i[1 - \exp(-\Gamma t)]$, with $\rho_u(t)$ the evolved state operator (4.25) without decoherence. From this follows the alignment

$$\langle \cos^2 \beta \rangle_t = \langle \cos^2 \beta \rangle_{\mathrm{u}} e^{-\Gamma t} + \frac{1}{3}\left(1 - e^{-\Gamma t}\right) \tag{4.29}$$

with $\langle \cos^2 \beta \rangle_{\mathrm{u}} = \mathrm{tr}(\rho_u(t) \cos^2 \mathsf{\beta})$. The decoherence leads to a decay of the alignment to a value of 1/3, in accordance to a uniform distribution over the spherical surface. This means that the alignment between the revivals decreases but we also see a decay of the revival signal until the revivals are fully destroyed after a characteristic time, determined by the rate Γ.

If environmental decoherence is included we have three important time scales in the quantum mechanical rotational dynamics. On the timescale $1/\kappa$ the dispersion leads to a rapid decay of the alignment to a value of 1/2, see Eq. (4.27), after the much longer revival time T_{rev} the collective interference of the orientational states lead to a brief reappearance of the initial alignment and on the timescale of decoherence $1/\Gamma$ we observe a decay of the revival signal and the alignment between the revivals to the value 1/3.

In the classical rotational dynamics the collisions with residual gas particles lead to a decay of the alignment from 1/2 to 1/3 as in the quantum mechanical case. In this case there are two significant time scales, $1/\kappa$ and $1/\Gamma$.

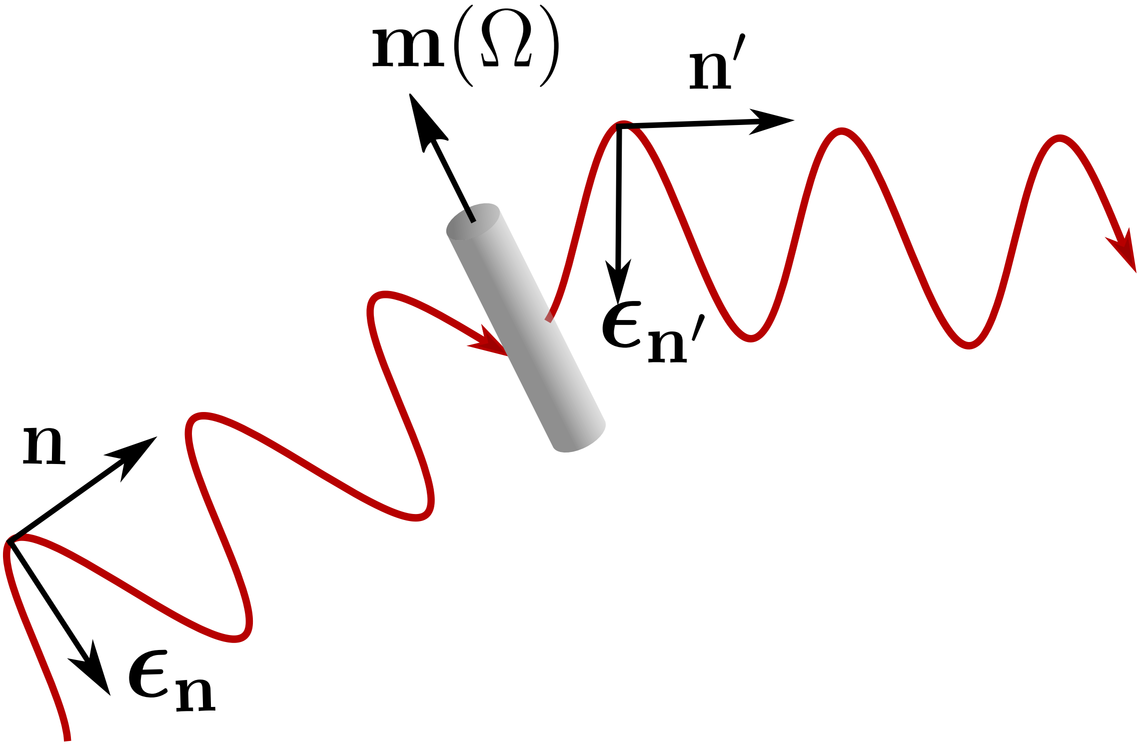

Figure 4.2.: Illustration of the unit vectors discussed in the main text. The light of the probe laser with propagation direction $\mathbf{n}$ and polarization vector $\boldsymbol{\epsilon}_{\mathbf{n}}$ is scattered at a dielectric rod with symmetry axis $\mathbf{m}(\Omega)$. The scattered field propagates in direction $\mathbf{n}'$ with polarization vector $\boldsymbol{\epsilon}_{\mathbf{n}'}$.

4.1.3. Measuring the Alignment

We have seen how the orientational state of the rotor evolves during the free fall and particularly we discussed the alignment dynamics. But how can one measure the alignment in an experiment?

One can observe the alignment of a dielectric linear rotor at a certain time by illuminating it with a plane laser wave pulse of nanoseconds duration, and collecting the scattered light, as demonstrated in Ref. [25]. The dielectric nanorod is characterized by an anisotropic suszeptibility tensor $\chi_0 = \mathrm{diag}(\chi_\perp, \chi_\perp, \chi_\parallel)$ and thus, the intensity of the scattered light depends on the angle between the symmetry axis of the rotor and the polarization of the probe beam. Thus, we choose a plane running laser wave $\mathbf{E}(\mathbf{r}) = E_0 e^{ik\mathbf{n}\cdot\mathbf{r}}\boldsymbol{\epsilon}_{\mathbf{n}}$ with direction of propagation $\mathbf{n} = \mathbf{e}_2$ and polarization direction $\boldsymbol{\epsilon}_{\mathbf{n}} = \mathbf{e}_3 \perp \mathbf{n}$. Here, the polarization direction is in the same direction as the trapping laser polarization, so that the measured alignment is comparable to the initial alignment. We calculate the scattered field $\mathbf{E}_{\mathrm{sc}}(\mathrm{r})$ in the limit of a small particle in comparison to the laser wavelength. In this approximation the light wave cannot resolve the shape of the particle and the field is approximately constant inside of the particle, so that the internal polarization field $\mathbf{u}(\Omega)$ has the same position dependence as the laser field [76]. This approximation is called Rayleigh-Gans approximation. With this the scattered field $\mathbf{E}_{\mathrm{sc}}(\mathbf{r})$ reads [76]

$$\mathbf{E}_{\mathrm{sc}}(\mathbf{r}) = -E_0 \frac{Vk^2\chi_\parallel}{4\pi}\frac{e^{ikr}}{r}\mathbf{n}' \times (\mathbf{n}' \times \mathbf{u}(\Omega)) \tag{4.30}$$

with $\mathbf{r} = r\mathbf{n}'$, the wave number k, the volume of the rod $V = \ell\pi d^2/4$. For a thin rod with a suszeptibility tensor $\chi(\Omega) = \mathsf{R}(\Omega)\mathrm{diag}(\chi_\perp, \chi_\perp, \chi_\parallel)\mathsf{R}^T(\Omega)$ the internal polarization field is given by

$$\mathbf{u}(\Omega) = \frac{\chi_\perp}{\chi_\parallel}\mathbf{e}_3 + \frac{\Delta\chi}{\chi_\parallel}[\mathbf{m}(\Omega)\cdot\mathbf{e}_3]\mathbf{m}(\Omega) \tag{4.31}$$

with an anisotropy in the suszeptibility $\Delta\chi$ and the symmetry axis $\mathbf{m}(\Omega) = \mathsf{R}(\Omega)\mathbf{e}_3$ of the nanorod. From the scattered field (4.30) follows the intensity $I(r\mathbf{n}')$ of the scattered light

$$I(r\mathbf{n}') = \frac{c\varepsilon_0}{2}\left(\frac{Vk^2E_0\chi_\parallel}{4\pi r}\right)^2 |\mathbf{n}' \times \mathbf{u}(\Omega)|^2. \tag{4.32}$$

Integrating the intensity over the whole sphere yields the power of the total scattered light. For the integration I parametrize

$$\mathbf{n}' = \cos\theta\mathbf{m}(\Omega) + \boldsymbol{\alpha}\sin\theta\cos\phi + \boldsymbol{\beta}\sin\theta\sin\phi \tag{4.33}$$

with

$$\boldsymbol{\alpha} = \mathbf{m}(\Omega)\times\mathbf{e}_3/|\mathbf{m}(\Omega)\times\mathbf{e}_3|, \tag{4.34a}$$

$$\boldsymbol{\beta} = \mathbf{m}(\Omega)\times\boldsymbol{\alpha}. \tag{4.34b}$$

With this we obtain

$$\begin{aligned} P(r;\Omega) =& \frac{c\varepsilon_0}{2}\left(\frac{Vk^2E_0\chi_\parallel}{4}\right)^2 \int_0^{2\pi}\mathrm{d}\phi\int_0^{\pi}\mathrm{d}\theta\sin\theta\left(2\frac{\Delta\chi\chi_\perp}{\chi_\parallel^2} + \frac{\Delta\chi^2}{\chi_\parallel^2}\right) \\ & \times(\mathbf{m}(\Omega)\cdot\mathbf{e}_3)^2 + \frac{\chi_\perp^2}{\chi_\parallel^2} - \left[\cos\theta\left(\frac{\chi_\perp}{\chi_\parallel} + \frac{\Delta\chi}{\chi_\parallel}\right)\mathbf{m}(\Omega)\cdot\mathbf{e}_3\right. \\ & \left. - \sin\theta\cos\phi\frac{\chi_\perp}{\chi_\parallel}|\mathbf{m}(\Omega)\times\mathbf{e}_3|\right]^2 . \end{aligned} \tag{4.35}$$

Carrying out the integrations yields

$$P(r;\Omega) = \frac{4\pi c\varepsilon_0}{3}\left(\frac{Vk^2E_0\chi_\parallel}{4}\right)^2\left[\frac{\chi_\perp^2}{\chi_\parallel^2} + \left(2\frac{\Delta\chi\chi_\perp}{\chi_\parallel^2} + \frac{\Delta\chi^2}{\chi_\parallel^2}\right)[\mathbf{m}(\Omega)\cdot\mathbf{e}_3]^2\right]. \tag{4.36}$$

We see that the resulting power is directly connected and in the limit $\chi_\perp \ll \chi_\parallel$ even proportional to $[\mathbf{m}(\Omega)\cdot\mathbf{e}_3]^2 = \cos^2\beta$. Repeating the measurement a hundreds of times for different points in time give us a statistical distribution of the alignment $\langle\cos^2\beta\rangle$ for these points in time.

Note that the illumination of the dielectric particle leads to complete decoherence of the orientational state. So one can only measure the alignment once before it is trapped and cooled again.

4.1.4. Recapture

To get the alignment signal one has to repeat the measurement of the alignment at the same time after turning off the trapping laser. The moment of inertia of a rod $I = \pi\varrho r^2\ell^3/12$ (with $\pi\varrho r^2\ell = M$) depends on the second power of the radius r of the rod and the third power of rod's length ℓ. Thus, a slight deviation in length or radius leads to high variation in the revival time $T_{\mathrm{rev}} = 2\pi I\hbar$. To prevent this variations in the revival time I suggest to recycle the particle for the repeating measurements.

After the alignment measurement the rotor is recaptured by switching on the trapping laser when the particle traverses an antinode of the resulting standing laser wave, so that it is captured in the laser potential. One can estimate the necessary laser power by estimating the kinetic energy of the falling particle directly after the revival.

We start with the momentum distribution $f_0(p_x) = \exp\left(-p_x^2/2mk_BT\right)/Z$ of the initial state at $x = x_0$, with the mass m and translational temperature T. Then the x-depending momentum distribution of the nanorotor after a falling distance of $s = x - x_0$ reads

$$f(p_x, x) = \frac{1}{Z}e^{-\left[p-\sqrt{2(x-x_0)gm}\right]^2/(2mk_BT)}. \tag{4.37}$$

With the recapture condition $E_{\mathrm{kin}} + V(x) < 0$ we obtain the limits of the allowed momenta $p_x^{\mathrm{min/max}}(x;P) = \pm\sqrt{2mV(x;P)}$, depending on the position x and the laser power P. For a conservative estimation of the probability of recapture we insert the minimum polarizability $\alpha = \alpha_\perp$ in the optical x-depending potential $V(x;P) = -4P\alpha_\perp\cos^2(kx)/\pi\varepsilon_0 cw_0^2$. By integrating the momentum distribution

(4.37) over all allowed momenta we obtain the recapture probability

$$W(x; P) = \int_{p_x^{\min}(x;P)}^{p_x^{\max}(x;P)} \mathrm{d}p_x \; f(p_x; x). \tag{4.38}$$

4.2. Implementation with Nanorotors

In the following, I discuss the proposed scheme using the example of two different nanoparticles. As we have seen in the discussion of the revival scheme, certain requirements on material and dimension of the particle must be met. For the initial trapping in an optical tweezer, the recapture, and the measurement of the alignment with a running plane laser wave we need a dielectric particle with an anisotropic polarizability. Further, we need a sufficiently stiff material, so that we can neglect vibrational effects by treating the particle as a rigid rotor and to avoid deformations during the recapture process. The mass and the dimensions of the particle are limited by the falling hight and the kinetic energy at times greater than the revival time. To demonstrate the viability of the scheme I discuss the experimental realization for semiconducting double-walled carbon nanotubes on the one hand and silicon nanorods on the other hand.

4.2.1. Silicon Nanorods and Double-Walled Carbon Nanotubes

A double-walled carbon nanotube (DWCNT) with a length of $\ell = 50\,\mathrm{nm}$, an outer diameter of 1.5 nm and an inner diameter of 1.1 nm has a mass of $M = 1.9 \times 10^5$ amu. From this follows a revival time of $T_{\mathrm{rev}} = 3.8\,\mathrm{ms}$. During this time the particle falls over $72\,\mu\mathrm{m}$.

The anisotropy in the polarizability $\Delta\alpha$ can be taken from [77] and depends on the type of the carbon nanotube. Here, I assume zigzag carbon nanotubes of the type (19,0) for the outer tube and (14,0) for the inner tube with $\Delta\alpha = 3,7 \times 10^{-35}$ $\mathrm{A}^2\mathrm{s}^4/\mathrm{kg}$.

A silicon nanorod of length $\ell = 50\,\mathrm{nm}$ can be fabricated with a diameter of $d = 5$ nm and has then a mass of $M = 1.4 \times 10^6$ amu. The revival time is $T_{\mathrm{rev}} = 28\,\mathrm{ms}$ and it falls about 4 mm until the first revival.

Initial state

The nanorotor is initially trapped in an optical tweezer with a laser waist of $w = 30\,\mu\mathrm{m}$ and a laser power of $P = 5\,\mathrm{W}$. To prepare a tightly aligned initial state, see the initial alignment in figure 4.4 for the DWCNT and figure 4.6 for silicon nanorods, one has to reach subkelvin temperatures. In our scenario a temperature of $T = 100$ μK implies that only the ground state is occupied. There are several works which show that feedback [25] or cavity cooling [30] of the rotational motion to subkelvin temperatures is feasible.

Environmental Orientational Decoherence

As discussed before, I expect two dominant sources of decoherence, the thermal emission of photons and scattering with residual gas particles. The total rate of decoherence events $\Gamma = \Gamma_{\text{th}} + \Gamma_{\text{gas}}$ is the sum of the rate Γ_{th} of thermal emissions of photons and the collision rate Γ_{gas} for collisions with residual gas particles.

There are several processes we have to consider when we think about thermal emission of photons. They are discussed in Ref. [14] and I will briefly summarize them in the following. The emission rate of photons with frequency ω increases with the internal temperature T_{int} and depends on a material specific absorption cross-section $\sigma_{\text{abs}}(\omega)$ [14].

$$\gamma_{\text{em}}(\omega) = \left(\frac{\omega}{\pi c}\right)^2 \sigma_{\text{abs}}(\omega) \exp\left(-\frac{\hbar\omega}{k_B T_{\text{int}}}\right). \tag{4.39}$$

Integrating this spectral rate over all frequencies yields the total emission rate $\Gamma_{\text{th}}(T_{\text{int}}) = \int_0^\infty \mathrm{d}\omega\, \gamma_{\text{th}}(\omega, T_{\text{int}})$. The internal temperature of the particle increases due to absorption of photons and decreases due to emission.

In Ref. [14] it is demonstrated that the trapping laser with a wavelength of $\lambda = 1.55\,\mu$m leads to a linear heating of a silicon nanoparticle but once the trapping laser is turned off the internal temperature remains almost constant and we do not expect relevant decoherence effects due to thermal emission of photons.

For semiconducting carbon nanotubes excitonic excitations play no role for wavelengths well above $2.5\,\mu m$ [78], while the position and width of vibrational excitations depend on the exact structure of the carbon nanotube [79]. Thus, the optimal trapping wavelength for the nanorotor used in the experiment which minimizes the heating of the DWCNT and with this the decoherence due to thermal emission can be determined experimentally. Thermal emissions of photons can be neglected for carbon nanotubes at room temperature. I propose to use an infrared laser with a wavelength between the vibrational excitations to minimize heating of the carbon nanotube. For my simulations I can then neglect the emission of thermal photons because there will always be a wavelength for which it is negligible in comparison to the decoherence process due to collisions with residual gas particles.

To estimate the collision rate Γ_{gas} of a cylindrical particle with a length ℓ and an effective diameter d_{eff} in a gas with atoms of mass m_g, pressure p_g and temperature T_g we integrate the particle flux into the surface of the rotors shape. The average particle flux is obtained by integrating the number of atoms hitting an area $\mathrm{d}A$ in a time interval $\mathrm{d}t$ with velocity v and angle θ to the normal vector on the surface over the velocity distribution, the Maxwell-Boltzmann distribution $f(v)$ [80]

$$J = \int_0^\infty \mathrm{d}v\, v^2 \int_0^{\pi/2} \mathrm{d}\theta \sin\theta \int_0^{2\pi} \mathrm{d}\phi\, v\cos\theta f(v) = \frac{p_g}{\sqrt{2\pi k_B T_g m_g}}. \tag{4.40}$$

Multiplying the average flux with the surface of the rod yields

$$\Gamma_{\text{gas}} = \frac{\pi p_g \ell d_{\text{eff}}}{\sqrt{2\pi k_B T_g m_g}} \left(1 + \frac{d_{\text{eff}}}{2\ell}\right). \tag{4.41}$$

Recapture

To estimate the laser power of the trapping lasers for a sufficient high recapture probability of the DWCNTs we assume a trapping laser wavelength of $\lambda = 20\,\mu$m and a falling distance of the rotor of around $s_{\text{cap}} = 80\,\mu\text{m} > s_{\text{rev}} = 72\,\mu$m. Assuming that the trapping laser is turned on in the perfect moment when the nanorotor traverses the potential minimum near 100 percentage for laser powers above $P = 25$ mW (see Fig. 4.3 (a)). But since it is impossible to hit this exact time we further examine in Fig. 4.3 (b) the probability as a function of the falling distance and the distance to the potential minimum at $x = 80\,\mu$m. We see that the probability decreases with increasing distance to the minimum and vanishes around the nodes of the standing wave. For a laser power of 50 mW there is a range of $\delta x = \pm 2.5\,\mu$m around the potential minimum for a successful recapture of the particle while this range for a laser power of 100 mW is $\delta x = \pm 3.5\,\mu$m. The particle needs $12.6\,\mu$s for the $5\,\mu$m distance and $17.6\,\mu$s for the distance of $7\,\mu$m, which give us as an estimation for the required precision in time for switching on the trapping laser.

4.2.2. Numerical Results

In a first step, we examine the alignment without including decoherence effects. In this case the initial alignment drops sharply to a value of $\langle\cos^2\beta\rangle = 1/2$ and recurs perfectly a the revival time T_{rev}, as it is shown in figure 4.4 (a). At one half of the revival time the particle is briefly located in the equatorial plane and thus we see a minimum of the alignment. Figure 4.4 (b) shows for three different temperatures the rapid decay of the initial alignment and the time around the first half revival and around the first revival. The initial states with temperatures of $100\,\mu$K and $1\,$mK are calculated by exact numerical diagonalization. Since this is no longer feasible for a temperature of $1\,$K I use the semiclassical matrix elements (4.18) calculated with Bohr-Sommerfeld quantized action-angle variables.

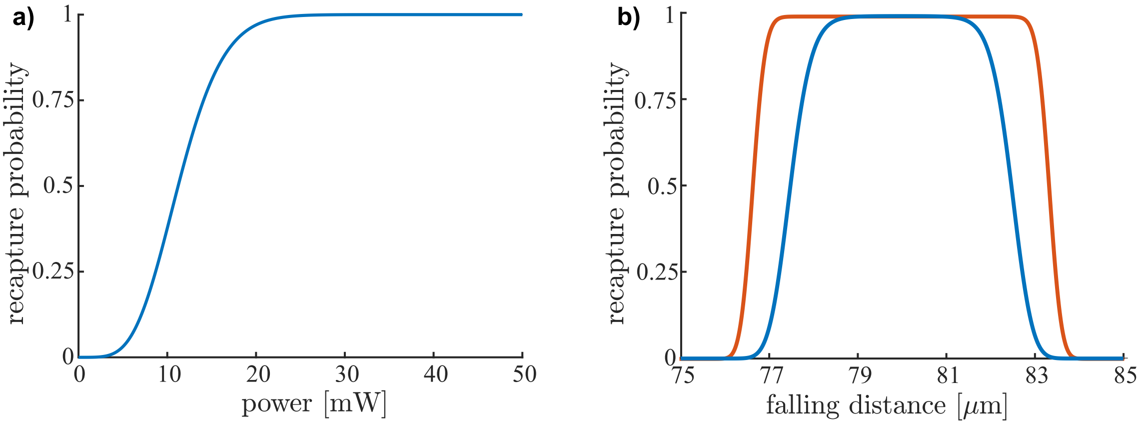

Figure 4.3.: a)Probability of recapture in dependence of the laser power P, assuming that the trapping lasers are turned on exactly in the moment the particle traverses the minimum of the b) Recapture probability for a fixed laser power P = 50 mW (blue line) and P = 100 mW (orange line) as a function of the falling distance and with this the location in the optical potential. In the minimum of the potential the probability is the highest and vanishes at the nodes of the standing laser wave.

The librational temperature affects the initial alignment but it affects the dispersion timescale even more. Although the initial alignment of the 100 μK and the 1 mK case is hard to distinguish we see a big difference as time progresses. The temperature is not the limiting factor for an experimental realization because of the decreasing initial alignment with increasing temperatures but because of the much faster dispersion process. This fast dispersion means that one has to measure the alignment very precisely in time.

Figure 4.5 shows the numerically calculated alignment signal for the carbon nanotubes as a function of time delay after the release of the trap. Here, the alignment signal is shown for an initial state with a temperature of T = 100 μK over a time of $60\,T_{\rm rev}$, including environmental decoherence due to collision with residual gas particles with a gas pressure of $p_g = 5 \times 10^{-9}$ mbar. Assuming nitrogen molecules and room temperature T = 300 K for the surrounding gas this leads to a time scale $1/\Gamma \approx 145$ ms of alignment decay from 1/2 to 1/3. Further, the decoherence destroys the interference effects, the reapperence of the initial state at integer multiples of the revival time and the brief local minima of the alignment at half integers of the revival time. Both values approach also the value of 1/3 with increasing time. In comparison we see in figure 4.6 the expected alignment signal for the silicon nanorods as function of time delay after the release. Due to the longer revival time $T_{\rm rev}$ = 28 ms we have to reduce the gas pressure to a value of $p_g = 5 \times 10^{-10}$mbar to observe multiple revivals.

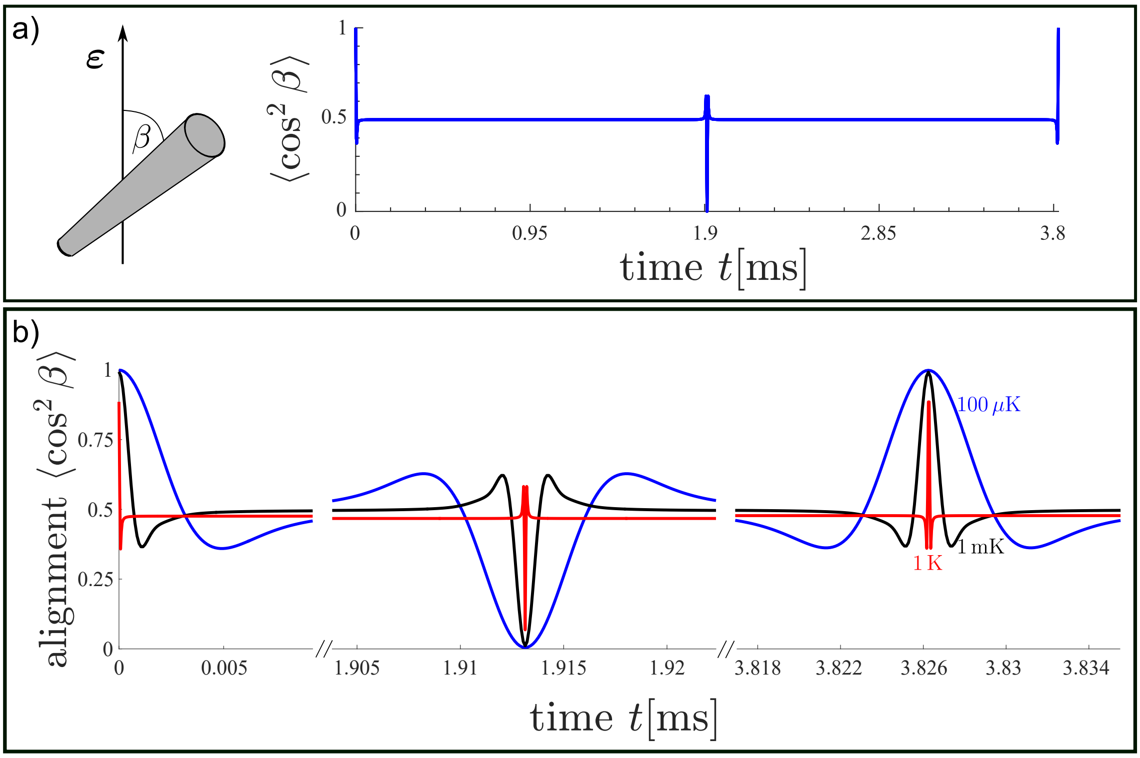

Figure 4.4.: a)Orientational alignment signal $\langle\cos^2\beta\rangle$ (blue solid line) for double-walled carbon nanotubes with a length of $\ell = 50$ nm and mass of $M = 1.9 \times 10^5$ amu at a temperature of 100 μK as a function of time. The initial state is tightly aligned and decays rapidly to a value of $1/2$ with rate κ, where it remains most of the time. But at integer multiples of the revival time $T_{\text{rev}} = 3.8$ ms the initial alignment reappears and it has a minimum at half integer multiples of T_{rev}. b) Initial alignment decay, half revival and first revival for three different temperatures.

4.3. Conclusion

I presented an experimentally viable scheme to observe orientational quantum revivals of nanoscale particles and to testify orientational superpositions of quantum rotors. The scheme needs no diffraction grating and is realizable with state-of-the art and upcoming techniques.

The orientational revivals are an effect of the free time evolution. Further questions are how external potentials affect the revival signal. I discuss this in the next chapters.

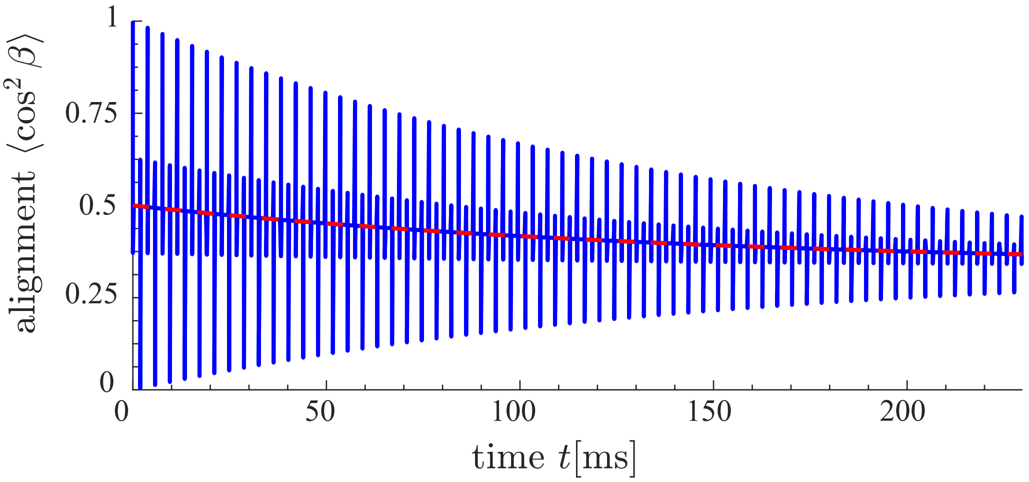

Figure 4.5.: Orientational alignment signal $\langle\cos^2\beta\rangle$ in for double-walled carbon nanontubes with a length of $\ell = 50$ nm and mass of $M = 1.9\times10^5$ amu at a temperature of 100 μK as a function of time. The surrounding gas has a pressure of $p_g = 5\times10^{-9}$mbar. Most of the time the signal is indistinguishable from the classical behaviour (red dashed line) where the alignment decays from 1/2 to 1/3 with the rate Γ, but at integer multiples of the revival time $T_{\text{rev}} = 3.8$ ms the initial alignment reappears and it has a minimum at half integer multiples of T_{rev}.

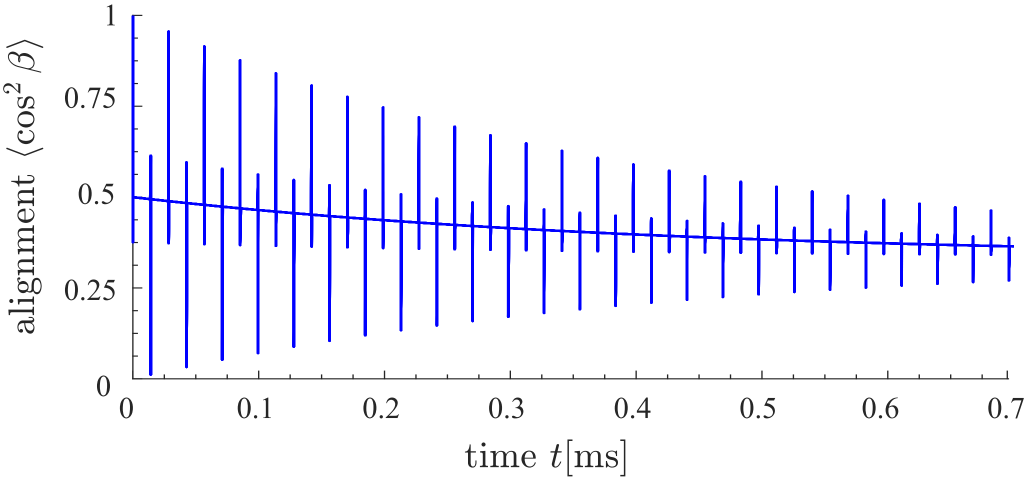

Figure 4.6.: Orientational alignment signal $\langle\cos^2\beta\rangle$ (blue solid line) for silicon nanorods with a length of $\ell = 50$ nm, a diameter of $d = 5$ nm, and mass of $M = 1.6\times10^6$ amu at a temperature of 100 μK as a function of time. The surrounding gas has a pressure of $p_g = 5\times10^{-10}$mbar. The initial state is tightly aligned and decays rapidly to a value of 1/2 with rate κ. Then the mean alignment decays from 1/2 to 1/3 with the rate Γ where it stays the most of the time. However, at integer multiples of the revival time $T_{\text{rev}} = 28$ ms the initial alignment reappears and at half integer multiples of T_{rev} it reaches a local minimum.

5. Rotation Dynamics in the Presence of a Static Potential

In the previous chapter, I discussed quantum revivals of the free rotation dynamics and how the interaction with the environment affects these quantum effects. Here, I focus on a new aspect and discuss the rotational quantum dynamics in the presence of an external torque. The torque has a strong influence on the quantum rotation dynamics and in particular the revival signal is sensitive to the torque. This may open the door for quantum enhanced torque sensing applications.

The external torque can be expected to have the highest influence on the revival signal, when it acts orthogonal to the polarization $\mathbf{e}_3$ of the trapping laser of the initial state. Therefore, I assume a Hamiltonian of the form

$$\begin{aligned}\mathsf{H} &= \frac{\mathsf{J}^2}{2I} - N_0[\mathbf{m}(\Omega)\cdot\mathbf{e}_1]^2 && (5.1)\\ &= \frac{\mathsf{J}^2}{2I} - N_0\cos^2\alpha\sin^2\beta, && (5.2)\end{aligned}$$

with the symmetry axis of the rotor $\mathbf{m}(\Omega)$.

Since the Hamiltonian (5.1) is no longer diagonal in the angular momentum representation, the numerical calculation of the time evolution is much more computationally intensive than for the free time evolution. Analogously to the numerical implementation of the initial thermalized state in 4.1.1 we can diagonalize the Hamiltonian in the angular momentum representation to obtain the eigenvalues E_n and corresponding eigenstates $|\phi_n\rangle$ in the angular momentum eigenbasis. This leads to

$$\mathsf{U} = \sum_n e^{-iE_nt/\hbar}\sum_{jm}\sum_{j'm'} a_{jm}^{(n)}a_{j'm'}^{*(n)}|jm\rangle\langle j'm'|. \tag{5.3}$$

Depending on the required cut-off value $j_{\max}$ it may be possible to carry out the numerical diagonalization of the Hamiltonian in a reasonable time and to store the eigenvectors temporarily. However, when combining the time evolution operator

(5.3) and the initial state (4.12) one obtains

$$\rho(t) = \sum_{n}\sum_{n'}\sum_{N} e^{-i(E_n - E_{n'})t/\hbar} e^{-E_N/(k_b T)} \sum_{j\in\mathbb{N}_0}\sum_{m=-j}^{j}\sum_{j'\in\mathbb{N}_0}\sum_{J\in\mathbb{N}_0}\sum_{m'=-\min(j',J)}^{\min(j',J)}\sum_{J'\in\mathbb{N}_0}\sum_{M'=-J'}^{J'} \\ \times a_{jm}^{(n)} a_{j'm'}^{*(n)} c_{j'm'}^{(N)} c_{Jm'}^{*(N)} a_{Jm'}^{(n')} a_{J'M'}^{*(n')} |jm\rangle\langle J'M'|. \tag{5.4}$$

A lot of summations have to be carried out numerically and in particular the summations over the quantum numbers j and m make the numerical calculation highly unattractive for large $j_{\max}$, since the calculation time increases as $j_{\max}^7$.

Instead of decomposing the Hamiltonian spectrally, we also could use matrix multiplication. But this method comes even earlier to its limits because of the large number of matrix elements and the finite size of the main memory. So, we need other methods than exact numerical calculations.

The difficulties here lie in sufficiently simplifying the calculation while preserving the crucial quantum properties of the rotational dynamics. In the following, we will see that here the rotational quantum dynamics can be based on the semiclassical WKB method [62] for planar rotations and later the EBK method [63] for linear rotations. In the end of this chapter, I use perturbation theory to discuss the effect of an external torque on the quantum revivals for the set up in chapter 4 with the double-walled carbon nanotube.

5.1. Semiclassical Approximations

In the following I apply the WKB method (see section 2.4.2) to calculate the time evolution of planar rotors in the presence of an external torque. After that, it is discussed to what extend the EBK method (see section 2.4.3) can be used to examine the effect of an external torque on the quantum rotational dynamics of a linear rigid rotor.

5.1.1. Planar Rigid Rotor: WKB Approximation

For the discussion of the planar rotational dynamics of a rotor with moment of inertia I I start with an initial state of the form

$$\psi_0(\alpha) = \frac{1}{N}\exp\left(\frac{\cos^2\alpha}{2\sigma_\alpha^2}\right) e^{i\alpha m_0}, \tag{5.5}$$

with the mean angular momentum m_0. The initial state is well-localized at $\alpha = 0$ and $\alpha = \pi$ with the angular spread σ_α.

The external potential $V(\alpha) = -N_0 \sin^2\alpha$ exhibits its minima at $\alpha = \pi/2$ and $\alpha = 3\pi/2$. The Schrödinger equation then reads

$$\hbar^2 \frac{\mathrm{d}\psi_{E_m}(\alpha)}{\mathrm{d}\alpha^2} + p_\alpha^2(\alpha)\psi_{E_m}(\alpha) = 0, \tag{5.6}$$

with $p_\alpha(\alpha) = \sqrt{2I\left[E_m + N_0\sin^2\alpha\right]}$. According to (2.55) the WKB eigenstates $\psi_{E_m}(\alpha)$ corresponding to the eigenenergies E_m are

$$\psi_{E_m}(\alpha) \propto \frac{1}{\sqrt[4]{2I\left[E_m + N_0\sin^2\alpha\right]}} \exp\left(\pm\frac{i}{\hbar}\sqrt{2IE_m}E(\alpha, -N_0/E_m)\right), \tag{5.7}$$

with the incomplete elliptic integral of the second kind $E(.,.)$.

The wave function of a planar rotor has to be 2π-periodic, $\psi_{E_m}(\alpha{+}2\pi m) = \psi_{E_m}(\alpha)$ with $m \in \mathbb{Z}$. This boundary condition leads to a quantization relation for the eigenenergies

$$\frac{\sqrt{2IE_m}}{\hbar} 4E(-N_0/E_m) = 2\pi m, \tag{5.8}$$

with $E(.)$ the complete elliptical integral of the second kind. We see here that the periodicity condition of the WKB eigenstates leads to the Bohr-Sommerfeld quantization rule of the action [62]. The complete elliptical integral of the second kind can only be inverted numerically. So there is no exact analytical expression for the semiclassical eigenenergies, but we can find an approximated solution. For the following calculation I use the dimensionless quantities $\tilde{E}_m = 2IE_m/\hbar^2$ and $\tilde{N}_0 = 2IN_0/\hbar^2$. Further, I assume that the potential depth N_0 is small in comparison to the eigenenergies E_m (high energy approximation) and expand the function $E(-N_0/E_m)$ for small arguments. With this I obtain a first approximation for the energy eigenvalues

$$\tilde{E}_m^{(0)} = -\frac{1}{4}\tilde{N}_0 + \frac{1}{2}m^2 + \frac{1}{2}m\sqrt{m^2 - \tilde{N}_0}. \tag{5.9}$$

This analytical expression is a first approach for the eigenenergies. To obtain a better approximation one may use Newton's method to solve equation (5.8) by finding the roots of the function

$$f(\tilde{E}_m) = 4\sqrt{\tilde{E}_m}E\left(-\frac{\tilde{N}_0}{\tilde{E}_m}\right) - 2\pi m. \tag{5.10}$$

It turns out that it is sufficient for our purpose to carry out only the first step of

Newton's method

$$\begin{aligned}\tilde{E}_m^{(1)} =&\tilde{E}_m^{(0)} - \frac{f'(\tilde{E}_m^{(0)})}{f(\tilde{E}_m^{(0)})}\\ =&\tilde{E}_m^{(0)} - \frac{2\tilde{E}_m^{(0)} E(-\tilde{N}_0/\tilde{E}_m^{(0)}) - \sqrt{\tilde{E}_m^{(0)}}m\pi}{K(-\tilde{N}_0/\tilde{E}_m^{(0)})},\end{aligned} \tag{5.11}$$

with the starting point $\tilde{E}_m^{(0)}$ given in (5.9) and $K(.)$ the complete elliptic integral of the first kind.

Using the approximated eigenenergies (5.11) and eigenstates (5.7) the time evolution of the alignment $\langle \cos^2 \alpha \rangle$ reads

$$\begin{aligned}\langle \cos^2 \alpha \rangle_t =& \sum_{m\in\mathbb{Z}} \sum_{m'\in\mathbb{Z}} \langle \psi_{E_m} | \psi_0 \rangle \langle \psi_0 | \psi_{E_{m'}} \rangle e^{-i(E_m - E_{m'})t/\hbar}\\ &\times \int_0^{2\pi} \mathrm{d}\alpha \; \langle \alpha | \psi_{E_m} \rangle \langle \psi_{E_{m'}} | \alpha \rangle \cos^2 \alpha .\end{aligned} \tag{5.12}$$

The α-integration can only be carried out numerically. For an analytical approximation I assume again that the eigenenergies $E_m \gg N_0$ are much greater than the potential depth N_0. In this limit we can expand the forth root in the demoninator and the incomplete ellipitic integral in expression becomes (5.7)

$$\frac{1}{\sqrt[4]{2I(E_m + N_0 \sin^2 \alpha)}} \approx \frac{1}{\sqrt[4]{2IE_m}} \left(1 - \frac{N_0}{4E_m} \sin^2 \alpha \right), \tag{5.13a}$$

$$E\left(\alpha, -\frac{N_0}{E_m}\right) \approx \alpha + \frac{N_0}{E_m}\frac{\alpha}{4}. \tag{5.13b}$$

With this approximation follow the approximated eigenstates

$$\psi_{E_m}(\alpha) = C \frac{1}{\sqrt[4]{2IE_m}} \left(1 - \frac{N_0}{4E_m} \sin^2 \alpha \right) \exp\left[i\sqrt{2IE_m} \left(\alpha + \alpha \frac{N_0}{4E_m} \right) /\hbar \right], \tag{5.14}$$

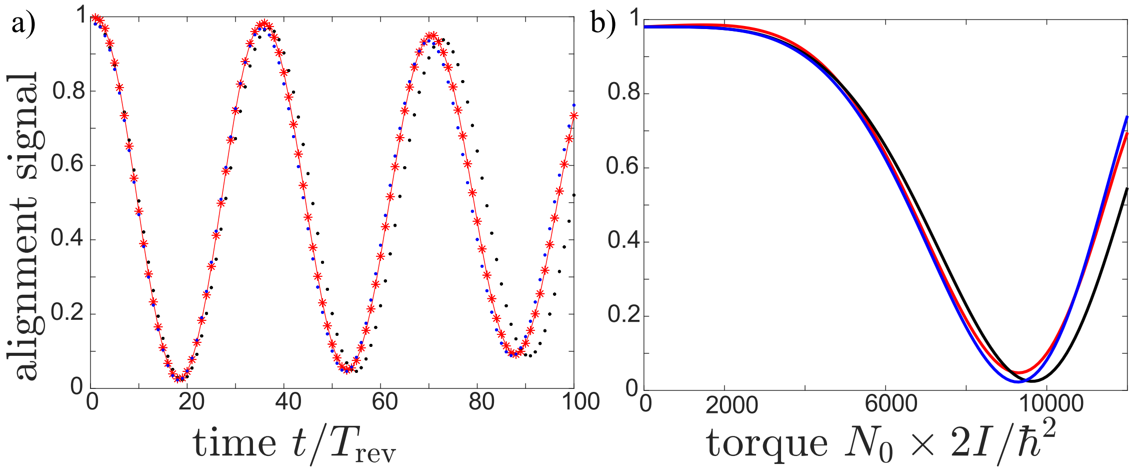

Figure 5.1.: Alignment signal of a planar rotor with the initial state $\langle m|\psi\rangle \propto \exp\left[-(m-m_0)^2/(2\sigma_m^2)\right]$ centered around $m_0 = 300$ with a width of $\sigma_m = 5$. The numerically exact signal (black) is compared to (5.12) as obtained with WKB approximated eigenstates (5.14) and eigenvalues (5.11) (blue). For the red graphs I use WKB approximated eigenvalues and in addition approximate the time evolution operator as diagonal in the m basis. In a) we see the alignment signal as a function of integer multiples of the revival time for a fixed value of $\tilde{N}_0 = 5000$ and in b) the alignment signal at the fifth revival as a function of the torque $\tilde{N}_0$.

with the normalization constant C. With this the α integration leads to

$$\begin{aligned}
&\int_0^{2\pi} \mathrm{d}\alpha \; \langle\alpha|\psi_{E_m}\rangle\langle\psi_{E_{m'}}|\alpha\rangle \cos^2\alpha \\
&= C^2\left(1-e^{i2\pi A}\right)\left[\frac{i}{2}\left(\frac{1}{A}+\frac{1}{2}\frac{1}{A+2}+\frac{1}{2}\frac{1}{A-2}\right)-\frac{i}{32}\left(\frac{N_0}{E_m}+\frac{N_0}{E_{m'}}\right)\right. \\
&\times\left(\frac{1}{A}+\frac{1}{2}\frac{1}{A+4}+\frac{1}{2}\frac{1}{A-4}\right)+\frac{i}{64}\frac{N_0^2}{E_mE_{m'}} \\
&\times\left.\left(\frac{1}{4}\frac{1}{A-6}-\frac{1}{2}\frac{1}{A-4}-\frac{1}{2}\frac{1}{A+4}-\frac{1}{4}\frac{1}{A+2}-\frac{1}{4}\frac{1}{A-2}+\frac{1}{A}+\frac{1}{4}\frac{1}{A+6}\right)\right],
\end{aligned} \tag{5.15}$$

with

$$A = \left[\sqrt{2IE_m}\left(1+\frac{N_0}{4E_m}\right)-\sqrt{2IE_{m'}}\left(1+\frac{N_0}{4E_{m'}}\right)\right]/\hbar. \tag{5.16}$$

We could even go one step further in approximating the eigenstates of the Hamiltonian by simply using the eigenstates of the potential-free Hamiltonian. The Hamiltonian is then diagonal in m which leads to a strongly simplified calculation.

Figure 5.1 shows that this quite strong approximation is permissible. We see almost no difference between the graphs calculated with WKB eigenstates and the ones with the eigenstates of the free Hamiltonian. The effect of the external torque on the revival signal is mainly determined by the difference in the energy eigenvalues.

To discuss the influence of the external torque on the revival signal, I examine the alignment signal for increasing integer multiples of the revival time and the revival signal at the fifth revival as a function of the torque N_0 (see Fig. 5.1).

The state of a freely revolving particle reappears at multiple integers of the revival time, whereas we see high influence of the potential to this behaviour. The external torque leads to a decreasing of the revival signal for the first integer multiples of the revival time. However, at a certain integer multiple of the revival time the alignment signal goes through a local minimum and increases after that followed by a periodic de- and increasing of the alignment signal.

We can observe a similar behaviour for the alignment signal as a function of the external torque. Here, at first the alignment signal decreases with increasing torque, but then it increases again.

5.1.2. Linear Rigid Rotor: EBK Approximation

After we have seen how to describe the quantum rotation dynamics of a planar rotor semiclassically we apply a similar method for the linear rigid rotor in the presence of an external torque. In the introductory part of this chapter we have seen how strongly the potential and especially the dependence on both, the polar and the azimuthal angle complicates the calculation of the rotational dynamics. Therefore I rotate the coordinate system such that now the trapping laser polarization points along the space-fixed $\mathbf{e}_1$- axis. This results in a thermal initial state $\rho = \exp[-\mathsf{H}/(k_B T)]$ with the Hamiltonian

$$\begin{aligned} \mathsf{H} &= \frac{\mathsf{J}^2}{2I} - V_0[\mathbf{e}_1 \cdot \mathbf{m}(\Omega)]^2 \\ &= \frac{\mathsf{J}^2}{2I} - V_0 \cos^2 \alpha \sin^2 \beta. \end{aligned} \tag{5.17}$$

The torque perpendicular to the trapping laser polarization is then given by $N(\Omega) = N_0[\mathbf{e}_3 \cdot \mathbf{m}(\Omega)]^2$. Thus, the Hamiltonian H_t for the time after switching off the trapping laser reads

$$\begin{aligned} \mathsf{H}_\mathrm{t} &= \frac{\mathsf{J}^2}{2I} - N_0[\mathbf{e}_3 \cdot \mathbf{m}(\Omega)]^2 \\ &= \frac{\mathsf{J}^2}{2I} - N_0 \cos^2 \beta. \end{aligned} \tag{5.18}$$

Now the torque depends only on the polar angle β and the time evolution operator is then diagonal in the quantum number m. This simplifies the calculation of the time evolution. But note that the initial state characterized by the Hamiltonian (5.17) is no longer diagonal in m and the alignment $\langle\cos^2\alpha\sin^2\beta\rangle$ is more complicated to calculate.

For the discussion of rotational dynamics of a linear rigid rotor we may use the insights gained from the treatment of the planar rotor. In particular, we focus on the semiclassical calculation of the energy eigenvalues and approximate right from the start the Hamiltonian (5.18) to be diagonal in j and m. Since we have to degrees of freedom, the angles α and β, I use the EBK approximation [63] for the calculation of the energy eigenvalues .

The classical Lagrangian reads

$$\mathcal{L}(\alpha,\beta,\dot{\alpha},\dot{\beta}) = \frac{I}{2}\left(\dot{\alpha}^2\sin^2\beta + \dot{\beta}\right) + N_0\cos^2\beta. \tag{5.19}$$

Identifying the canonical momenta $p_\alpha = I\dot{\alpha}\sin^2\beta$ and $p_\beta = I\dot{\beta}$ we obtain the classical Hamiltonian function corresponding to (5.18)

$$\mathcal{H}(\alpha,\beta,p_\alpha,p_\beta) = \frac{1}{2I}\left(\frac{p_\alpha^2}{\sin^2\beta} + p_\beta^2\right) - N_0\cos^2\beta. \tag{5.20}$$

The canonical momentum p_α and the total energy $E = \mathcal{H}(\alpha,\beta,p_\alpha,p_\beta)$ are independent constants of motion and so the system is integrable. From the quantization of the action $I_\alpha = \hbar m$ for the α-motion follows

$$I_\alpha = \frac{1}{2\pi}\oint \mathrm{d}\alpha\; p_\alpha = \frac{1}{2\pi}\int_0^{2\pi} p_\alpha = p_\alpha = \hbar m. \tag{5.21}$$

When we look at the β-motion, we see that the particle evolves in an effective p_α-dependent potential

$$V_{\text{eff}}(\beta) = \frac{p_\alpha^2}{2I\sin^2\beta} - N_0\cos^2\beta. \tag{5.22}$$

This potential diverges for $\beta = 0$ and $\beta = \pi$ and so the β motion has two turning points β_{min} and β_{max}. At the turning points we have $\dot{\beta} = 0$ yielding the equation

$$2I(E + N_0\cos^2\beta_{\text{min,max}})\sin^2\beta_{\text{min,max}} - p_\alpha^2 = 0. \tag{5.23}$$

From this follow the turning points expressed in terms of the constants of motion

$$\beta_{\text{min}}(E,p_\alpha) = \arccos\left[\frac{1}{2} - \frac{E}{2N_0} + \sqrt{\left(\frac{1}{2} - \frac{E}{2N_0}\right)^2 + \frac{E}{N_0} - \frac{p_\alpha^2}{2IN_0}}\,\right], \tag{5.24a}$$

$$\beta_{\text{max}}(E,p_\alpha) = \pi - \beta_{\text{min}}(E,p_\alpha). \tag{5.24b}$$

We have to consider these turning points for the quantization of the action $I_\beta = \hbar(n+1/2)$ by adding a Maslov index of 1/4 for each of them and get

$$I_\beta = \frac{1}{\pi}\int_{\beta_{\min}(E,p_\alpha)}^{\beta_{\max}(E,p_\alpha)} \mathrm{d}\beta \sqrt{2I(E+N_0\cos^2\beta) - \frac{\hbar^2 m^2}{\sin^2\beta}} = \hbar(n+1/2). \tag{5.25}$$

As discussed in section 2.4.3 we replace $n = j - |m|$. Equation (5.25) implies a relation for the energy eigenvalues. We can find these energy eigenvalues E_{jm} corresponding to the quantum numbers j and m again by calculating the root of the function

$$\begin{aligned} f(E_{jm}) =& \frac{1}{\pi}\int_{\beta_{\min}(E_{jm},p_\alpha)}^{\beta_{\max}(E_{jm},p_\alpha)} \mathrm{d}\beta \left(\sqrt{2I(E_{jm}+N_0\cos^2\beta) - \frac{\hbar^2 m^2}{\sin^2\beta}}\right) \\ &- \hbar(j-|m|+1/2) = 0 \end{aligned} \tag{5.26}$$

for each j and m by Newton's method. In contrast to the planar rotor, it is not sufficient to carry out only the first iteration step, so that the energy eigenvalues must be calculated numerically.

When we approximate the energy eigenvalues of the free Hamiltonian ($N_0 = 0$) in this way we obtain $E_j = \hbar^2(j+1/2)^2/(2I)$. For large j the difference between $(j+1/2)^2$ and $j(j+1)$ might seem negligible but looking at the revivals it makes a crucial difference because the semiclassical eigenvalues are no longer integer multiples of $\hbar^2/(2I)$ and one wouldn't observe revivals in simulations using these eigenvalues. Thus, we subtract a value of 1/4 from eigenvalues resulting from equation (5.26).

We can now apply the EBK approximation of the eigenvalues and the assumption of the time evolution operator to be diagonal in the angular momentum basis to examine the effect of an external torque onto the revival signal and compare it to exact numerical results, see Fig. 5.2. As an initial state I use a thermal state $\rho = \exp(-V_0\sin^2\alpha\cos^2\beta)$ which can be diagonalized numerically. We see that an increasing external torque N_0 leads to a decrease of the revival signal.

The approximation shows the same behaviour of the alignment signal as the exact calculations but deviates more from the exact result than we have seen for the WKB approximations for planar rotors. Additionally, we are limited to initial states which can be diagonalized numerically because we do not know a suitable method to approximate thermal states depending on the azimuthal angle α and the polar angle β. Thus, in the next section we examine an alternative method to consider external torques.

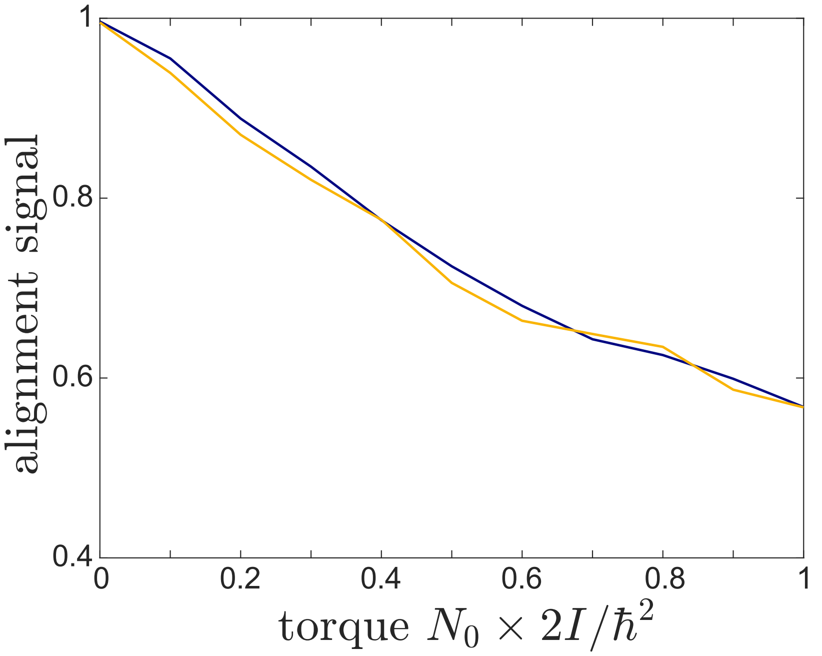

Figure 5.2.: Alignment signal at the second revival as a function of the torque N_0 of a linear rotor with the thermal initial state $\rho \propto \exp(-V_0 \cos^2\alpha \sin^2\beta)$ with $V_0 = 1.8 \times 10^5\, 2I/\hbar^2$ and $I = 10^{-43}\,\mathrm{kgm}^2$. The numerically exact signal (blue) is compared to the one (red) obtained by using EBK eigenvalues and approximating the time evolution operator as diagonal in the angular momentum basis $|jm\rangle$.

5.2. Perturbation Theory

In section 5.1.2 we have chosen an potential depending on the Euler angles α and β for the preparation of the initial state and a β-dependent torque during the time evolution. Since the dependence on α leads to difficulties in the exact numerical calculation and also in the approximation of the initial state, we now choose a β-dependent potential for the initial state as in chapter 4 and the Hamiltonian 5.1 for the time evolution after the release of the trapping potential.

Next to semiclassical methods the perturbation theory is a very common method to describe the time evolution approximately. Here, we assume that the orientation dependent potential $N(\alpha,\beta) = -N_0 \cos^2\alpha \sin^2\beta$ is only weak compared to the kinetic energy $E_{\mathrm{rot}} = \langle \mathsf{J}^2/2I \rangle$ of the particle. Thus, we can write the complete Hamiltonian (5.1) of the system,

$$\mathsf{H} = \mathsf{H}^{(0)} + \lambda \tilde{\mathsf{N}}, \tag{5.27}$$

in terms of the unperturbated Hamiltonian $\mathsf{H}^{(0)}$ and the small parameter $\lambda = N_0/E_{\mathrm{rot}}$ and the potential $\tilde{\mathsf{N}} = -E_{\mathrm{rot}} \cos^2\boldsymbol{\alpha} \sin^2\boldsymbol{\beta}$. If the perturbation is sufficiently small the energy eigenvalues E_n and the corresponding eigenstate $|n\rangle$ can be written as a power series in the small parameter λ

$$E_n = E_n^{(0)} + \lambda E_n^{(1)} + \lambda^2 E_n^{(2)} + ... \tag{5.28a}$$

$$|n\rangle = |n^{(0)}\rangle + \lambda |n^{(1)}\rangle + ... \tag{5.28b}$$

In the following, I will only calculate the first-order change. If the eigenvalues $E_n^{(0)}$ of the unperturbated Hamiltonian are non-degenerate the first-order energy correction is given by the expectation value of the perturbation with respect to the unperturbated state $|n^{(0)}\rangle$

$$E_n^{(1)} = \langle n^{(0)}|\tilde{\mathsf{N}}|n^{(0)}\rangle. \tag{5.29}$$

The first-order correction of $|n^{(1)}\rangle$ of the eigenstates is then given by

$$|n^{(1)}\rangle = \sum_{k\neq n} \frac{\langle k^{(0)}|\tilde{\mathsf{N}}|n^{(0)}\rangle}{E_n^{(0)} - E_k^{(0)}} |k^{(0)}\rangle. \tag{5.30}$$

However, we have already seen that the free-flight Hamiltonian with the eigenstates $|jm\rangle$ has eigenvalues E_j with $(2j+1)$-fold degeneracy. The eigenstates for degenerate eigenvalues are not unambiguous. But the choice of the eigenbasis crucially determines the outcome of the first-order change of the eigenvalues. Thus, we have to make the right choice for the eigenbasis. In equation (5.30) we see that the degeneracy of the eigenstates leads to a possible value of zero in the denominator and we choose the eigenbasis in a way that leads to a finite correction of the eigenstates [81].

To this end we solve the eigenvalue problem in the degenerated subspace exactly and use the basis in which the orientation-dependent perturbation operator $\sin^2 \beta \cos^2 \alpha$ is diagonal in the subspace of fixed j. For the calculation the

$(2j+1) \times (2j+1)$ matrix with the elements

$$\begin{aligned}
\langle jm| \sin^2 \beta \cos^2 \alpha |jm'\rangle = \\
&\sqrt{\frac{1}{6}}(-1)^m (2j+1) \begin{pmatrix} j & j & 2 \\ 0 & 0 & 0 \end{pmatrix} \begin{pmatrix} j & j & 2 \\ -m & m' & -2 \end{pmatrix} \delta_{mm'-2} \\
+&\sqrt{\frac{1}{6}}(-1)^m (2j+1) \begin{pmatrix} j & j & 2 \\ 0 & 0 & 0 \end{pmatrix} \begin{pmatrix} j & j & 2 \\ -m & m' & 2 \end{pmatrix} \delta_{mm'+2} \\
+&\frac{1}{3} \left[ ]1 - (-1)^m (2j+1) \begin{pmatrix} j & j & 2 \\ 0 & 0 & 0 \end{pmatrix} \begin{pmatrix} j & j & 2 \\ -m & m' & 0 \end{pmatrix} \right] \delta_{mm'}
\end{aligned} \tag{5.31}$$

is diagonalized for each value of j. With numerical diagonalization we obtain unperturbated eigenstates $|\psi_j^k\rangle$ in terms of the linear combination of the eigenstates $|jm\rangle$

$$|\psi_j^k\rangle = \sum_{m=-j}^{j} c_m^{(k)} |jm\rangle. \tag{5.32}$$

Now these eigenstates can be used for the calculation of the first order change of the eigenvalues and eigenstates as described in (5.29) and (5.30) and we obtain

$$E_{jk}^{(1)} = \langle \psi_{jk} | \tilde{\mathsf{N}} | \psi_{jk} \rangle, \tag{5.33a}$$

$$|\psi_{jk}^{(1)}\rangle = \sum_{j' \neq j} \sum_{k=1}^{2j+1} |\psi_{j'k'}\rangle \frac{\langle \psi_{j'k'} | \tilde{\mathsf{N}} | \psi_{jk} \rangle}{E_{j'}^{(0)} - E_j^{(0)}} + \sum_{k' \neq k} |\psi_{jk'}\rangle \frac{\langle \psi_{jk'} | \tilde{\mathsf{N}} | \psi_{jk} \rangle}{E_j^{(0)} - E_j^{(0)}}, \tag{5.33b}$$

where the second summation vanishes due to the diagonality of the perturbation operator $\tilde{\mathsf{N}}$.

With the perturbation theory we can calculate approximate eigenstates and eigenvalues without the numerical diagonalization of the complete Hamiltonian but only with diagonalization of the potential operator in the subspace of a fixed j. But carrying out the time evolution with these approximate eigenstates is still numerical expensive as seen in equation (5.4).

For a further simplification I assume that the dominant effect of the external potential on the time evolution and especially on the revival signal is due to the change of the energy eigenvalues. The α-dependence of the potential reduces the multi-state degeneracy, involving all states with the same angular momentum quantum number j, to a two-state degeneracy, consisting of the two states with same j and $|m|$. Thus, in the following, I consider the first-order correction of the eigenvalues, but use the unperturbated eigenstates $\psi_{jk}^{(0)}$. The resulting time evolution operator is diagonal in the quantum number j, but not in the quantum number m. With this we can

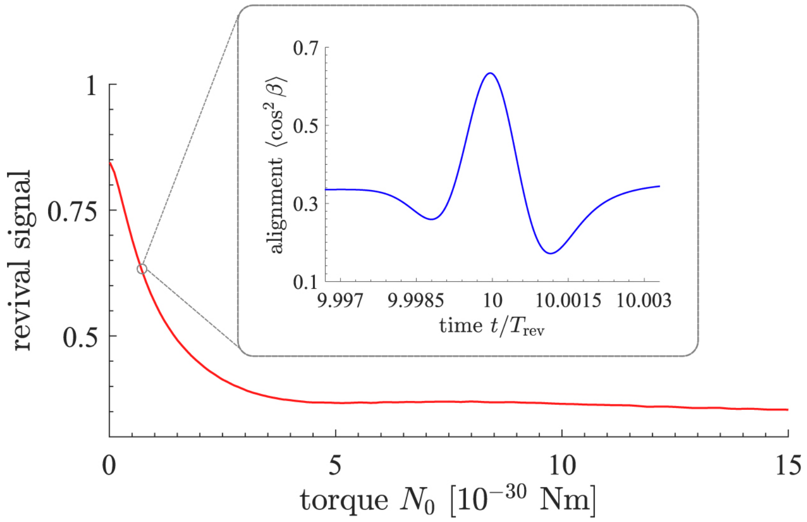

Figure 5.3.: The decay of the tenth revival signal of a CNT ($T = 100\,\mu$K) in presence of an external torque N_0 can be used for ultra-precise sensing, surpassing the sensitivity of state-of-the-art systems by many orders of magnitude. The inset shows the alignment signal as a function of time for $N_0 = 7 \times 10^{-31}$ Nm.

introduce the time evolution operator $U_j = \exp(-itH_j/\hbar)$ acting on the subspace of fixed j with

$$H_j = \frac{\hbar^2}{2I}\mathbb{1}_j + \langle jm|\mathsf{N}_{\mathrm{ext}}|jm'\rangle, \tag{5.34}$$

with $\mathbb{1}_j$ a $(2j+1) \times (2j+1)$ identity matrix. For the calculation of the time evolution of the alignment $\langle \cos^2 \upbeta \rangle$ the initial state $\rho_0 = \sum_k p_k |\Phi_k\rangle\langle\Phi_k|$ is diagonalized and we define the vectors $(\underline{\Phi}_{kj})_m$. The alignment signal can now be expressed by summations over matrix multiplications in the subspace of fixed j and j'

$$\langle \cos^2 \upbeta \rangle = \sum_n \sum_{j=0}^{\infty} \sum_{j'=0}^{\infty} p_n \underline{\Phi}_{nj} \cdot \mathsf{U}_j \mathsf{C}_{jj'} \mathsf{U}_{j'}^{\dagger} \underline{\Phi}_{nj'}, \tag{5.35}$$

with $C_{jj'}$ a $(2j+1) \times (2j+1)$ matrix with elements $(C_{jj'}) = \langle jm| \cos^2 \upbeta |j'm\rangle$. With this we can calculate the alignment signal for a realistic particle in the presence of an external torque. In figure 5.3 we see the revival signal for the tenth revival of the carbon nanotube discussed in chapter 4 at a temperature of $T = 100\,\mu$K. With increasing torque the revival signal decreases and for torques larger than 2×10^{-30} Nm it is completely suppressed. This implies that torques on the order of 10^{-30} Nm are observable with this set up. This is eight orders of magnitude smaller than levitated [26,28] or solid-state-integrated [82] set ups considered so far and with this promising for ultra sensitive torque sensing.

6. Interferometric Control of Nanorotor Alignment

In chapter 4 I discussed orientational quantum revivals, a quantum effect in the free rotational dynamics of symmetric rotors. It has already been proposed to control the planar rotational quantum dynamics of trapped Bose-Einstein condensates [46] and planar and linear rotations of molecules [47]. Here, I present an interferometric scheme, a rotational analogue of Mach-Zehnder interferometry, which allows steering the 3D alignment of symmetric nanorotors with weak, pulsed torques.

We will see that the free rotational dynamics of a linear rigid rotor exhibit a particular phenomenon: an initially tightly aligned state emerges briefly in a superposition of well-localized wave packets after integer fractions of the revival time. We can exploit this superposition to imprint a relative phase between the individual wave packets by applying a short pulsed torque and thus control the nanorotor alignment interferometrically. The results of this chapter are published in Ref. [83].

In the first part of this chapter, I introduce the interference scheme and start with a description of the time evolution of a freely rotating linear rigid rotor with help of a semiclassically approximated time evolution operator. We will find that the state at one eighth of the revival time $t = T_{\mathrm{rev}}/8$ offers a good possibility for imprinting the required relative phase. By introducing a semiclassical eight-state model I then demonstrate that this enables tuning the alignment at the revival time from fully aligned to completely anti-aligned. After that, I focus on the experimental realization and numerical implementation of the phase pulse. In the second part, I treat the alignment control of realistic particles by accounting for symmetric rigid rotors with a finite occupation of the intrinsic angular momentum component, a slightly asymmetry of the nanorotor, and orientational decoherence due to the interaction with the environment. I discuss how these effects degrade the interference signal at the example of silicon nanorods, thus demonstrating that steering the alignment is viable for realistic particles in a realistic environment.

6.1. Interference Scheme

The exact time evolution operator for the free time evolution of a symmetric rotor is given by $\mathsf{U} = \exp(-it\mathsf{H}_{\mathrm{rot}}/\hbar)$, with the Hamiltonian (2.25) for symmetric rotors. In the angular momentum eigen basis it takes the form

$$U = \sum_{jkm} e^{-i\pi[j(j+1)+(I/I_c-1)k^2]t/T_{\mathrm{rev}}} |jmk\rangle\langle jmk|, \tag{6.1}$$

where I introduced the revival time $T_{\mathrm{rev}} = 2\pi I/\hbar$. With this time evolution operator we evolve a state which is initially aligned in direction of the space-fixed $\mathbf{e}_3$-axis. This implies that the initial state is diagonal in the quantum numbers m and k. According to (6.1) initial states of a symmetric rotor, diagonal in k, fully recur at the revival time $\mathsf{U}(T_{\mathrm{rev}})\rho_0\mathsf{U}^\dagger(T_{\mathrm{rev}}) = \rho_0$ even for finite k. What is more, expectation values of observables, which are diagonal in the quantum number k, such as the alignment $\langle\cos^2\upbeta\rangle$, reappear at $t = T_{\mathrm{rev}}$, even for arbitrary initial states of symmetric rotors since in this case only the coherences in k play a role.

For the following calculation we assume a pure state of a massive prolate top ($I_c \ll I$) which is well-aligned with the space-fixed $\mathbf{e}_3$-axis ($\beta \approx 0$). In this limit of a small polar angle β the body- and space-fixed angular momentum component $\tilde{\mathsf{J}}_3$ and J_3 coincidence. We may therefore choose the exemplary initial state

$$\langle\alpha\beta\gamma|\Psi_0\rangle = \langle\beta|\psi_0\rangle e^{ik_0(\alpha+\gamma)} \tag{6.2}$$

with fixed k_0 and an azimuthally symmetric part $\langle\beta|\psi_0\rangle$. With the time evolution operator (6.1) we evolve the initial state (6.2) freely in time and obtain

$$\langle\alpha\beta\gamma|\mathsf{U}(t)|\Psi_0\rangle = \int_0^{2\pi} \mathrm{d}\alpha_0 \int_0^{\pi} \mathrm{d}\beta_0 \, \sin\beta_0 \int_0^{2\pi} \mathrm{d}\gamma_0 \, \langle\alpha\beta\gamma|\mathsf{U}(t)|\alpha_0\beta_0\gamma_0\rangle\langle\alpha_0\beta_0\gamma_0|\Psi_0\rangle \tag{6.3}$$

with the exact propagator

$$\begin{aligned}\langle\alpha\beta\gamma|\mathsf{U}(t)|\alpha_0\beta_0\gamma_0\rangle =& \sum_{j\in\mathbb{Z}} \sum_{m=-j}^{j} \sum_{k=-j}^{j} \frac{2j+1}{8\pi^2} d^j_{mk}(\beta) d^j_{mk}(\beta_0) e^{im(\alpha-\alpha_0)} \\ &\times e^{ik(\gamma-\gamma_0)} e^{-i\pi[j(j+1)+(I/I_c-1)k^2]t/T_{\mathrm{rev}}}.\end{aligned} \tag{6.4}$$

Here, $d^j_{mk}(\beta)$ denote small Wigner d-matrices, see Eq. (2.27).

Semiclassical Time Evolution Operator

Due to the tight alignment of the initial state (6.2) the total angular momentum quantum number j is distributed over a wide range, while the fixed k_0 is small compared to j. Thus, we can approximate the Wigner d-matrices $d^j_{mk}(\beta)$ in the propagator (6.4) for small values of $|m|$ and $|k|$ in comparison to j, i.e. $|m|$, $|k| \ll j$ [84]

$$d^j_{mk}(\beta) \approx \frac{\cos\left[\left(j+\frac{1}{2}\right)\beta + (m-k)\frac{\pi}{2} - \frac{\pi}{4}\right]}{\sqrt{\frac{\pi}{2}\left(j+\frac{1}{2}\right)\sin\beta}}. \tag{6.5}$$

In a first step, I focus on the time evolution for initial states (6.2) with $k_0 = 0$. The effect of finite k and m is discussed later on. The initial state is then independent of α and γ and with (6.5) we obtain the semiclassical propagator for the β-motion

$$\langle\beta|\mathsf{U}_\beta(t)|\beta_0\rangle \approx \frac{u_c(\beta-\beta_0;t) + u_s(\beta+\beta_0;t)}{\sqrt{\sin\beta\sin\beta_0}} \tag{6.6}$$

with

$$u_c(\Delta\beta;t) = \frac{1}{\pi}\sum_{j\in\mathbb{N}_0} e^{-i\pi j(j+1)t/T_{\text{rev}}} \cos\left[\left(j+\frac{1}{2}\right)\Delta\beta\right], \tag{6.7a}$$

$$u_s(\bar{\beta};t) = \frac{1}{\pi}\sum_{j\in\mathbb{N}_0} e^{-i\pi j(j+1)t/T_{\text{rev}}} \sin\left[\left(j+\frac{1}{2}\right)2\bar{\beta}\right]. \tag{6.7b}$$

Here, and throughout this chapter I use the abbreviations $\Delta\beta = \beta - \beta_0$ and $\bar{\beta} = (\beta + \beta_0)/2$. Note that one gets the same result by calculating the semiclassical eigenstates of the time evolution operator (6.1) in WKB approximation, as explained in the appendix A.

For the evaluation of the semiclassical propagator at integer fractions of the revival time we can use the expressions

$$\sum_{j\in\mathbb{N}_0} \cos(j\theta) = \pi\sum_{n\in\mathbb{Z}} \delta(\theta - 2\pi n) + \frac{1}{2}, \tag{6.8a}$$

$$\sum_{j\in\mathbb{N}_0} \sin(j\theta) = \frac{1}{2}\mathcal{P}\cot\left(\frac{\theta}{2}\right), \tag{6.8b}$$

based on the Poisson summation formula to resum the summands (6.7). Here, $\mathcal{P}$ denotes the Cauchy principal value.

For $t = 0$ we use the angle sum identity $\cos[(j + 1/2)\beta] = \cos(\beta/2)\cos(j\beta) -$

$\sin(\beta/2)\sin(j\beta)$ and apply (6.8). Thus, we obtain $u_c(\beta-\beta_0;0)=\delta(\beta-\beta_0)$. The finite value of $u_s(\bar\beta;0)$ is an artifact of the semiclassical approximation and has to be neglected to obtain the the expected behaviour $\mathsf{U}(0)=\mathbb{1}$.

For fractions of the revival time the calculation is more lengthy and I show the whole calculation for $t=T_{\text{rev}}/8$ in detail. In a first step, we rewrite the contributions (6.7) of the propagator

$$u_c(\Delta\beta;t)=\frac{1}{2\pi}e^{i\Delta\beta/2}\sum_{k\in\mathbb{Z}}e^{i\pi k(k+1)t/T_{\text{rev}}}e^{ik\Delta\beta}, \tag{6.9a}$$

$$u_s(\bar\beta;t)=\frac{1}{\pi}\sin\bar\beta+\frac{1}{\pi}\sum_{j=1}^{\infty}e^{i\pi j(j+1)t/T_{\text{rev}}}\sin\left[\left(j+\frac{1}{2}\right)\bar\beta\right]. \tag{6.9b}$$

For $t=T_{\text{rev}}/8$ the time depending exponential function within the sum (6.9) evaluates to values $\exp(il\pi/4)$ with $l\in\mathbb{Z}$ grouped into eight sets of equal phase, see table 6.1.

k		$e^{i\pi k(k+1)/8}$
$16n$	$16n-1$	1
$16n-2$	$16n+1$	$e^{-i\pi/4}$
$16n-3$	$16n+2$	$e^{-i3\pi/4}$
$16n-4$	$16n+3$	i
$16n-5$	$16n+4$	$-i$
$16n-6$	$16n+5$	$e^{i\pi/4}$
$16n-7$	$16n+6$	$e^{i3\pi/4}$
$16n-8$	$16n+7$	-1

Table 6.1.: Overview over the possible results for the time depending exponential function within the summation (6.9) depending on the summation index k with $n\in\mathbb{Z}$ respectively on the summation index j with $n\in\mathbb{N}$.

After grouping the contribution (6.9a) into these eight sets of equal phase one can extract the term $\sum_{n\in\mathbb{Z}}\exp(i16n\Delta\beta)/(2\pi)$ which can be transformed by the expression (6.8a) to a summation over delta-distributions $\sum_{n\in\mathbb{Z}}\exp(i16n\Delta\beta)/(2\pi)=\sum_{l\in\mathbb{Z}}\delta(\Delta\beta-l\pi/8)/16$. We see that the part (6.9a) of the propagator has only finite values for $\Delta\beta=n\pi/8$ with $n\in\mathbb{Z}$. After calculating the prefactors for the different $n\in\mathbb{Z}$ we obtain

$$\begin{aligned}u_c(\Delta\beta;T_{\text{rev}}/8)&=\frac{\sqrt{2}}{4}\sum_{n=0}^{3}e^{-i(3+2n(n+1))\pi/16}\\&\times\left[\delta\left(\Delta\beta-(2n+1)\frac{\pi}{8}\right)+\delta\left(\Delta\beta+(2n+1)\frac{\pi}{8}\right)\right].\end{aligned} \tag{6.10}$$

Analogous to that we calculate the part $u_s(\bar{\beta}; T_{\text{rev}}/8)$ and obtain

$$\begin{aligned} u_s(\bar{\beta}; T_{\text{rev}}/8) = \frac{1}{\pi} \sin \bar{\beta} + \frac{2}{\pi} \sum_{n=0}^{3} e^{-in(n+1)\pi/8} \\ \times P \left[\cos\left((2n+1)2\bar{\beta}\right) - \cos\left(2(15-2n)\bar{\beta}\right) \right] \cot 16\bar{\beta}. \end{aligned} \tag{6.11}$$

This term has Cauchy-integrable singularities for $2\bar{\beta} = (2n+1)\pi/8$ with $n \in \mathbb{Z}$. Together with the locations of the delta distributions this implies that a state initially tightly aligned around $\beta = 0$ and $\beta = \pi$ is at $t = T_{\text{rev}}/8$ in a superposition of four well-localized states, localized at $\beta = \pi/8$, $\beta = 3\pi/8$, $\beta = 5\pi/8$ and $\beta = 7\pi/8$ (as is seen in Fig. 6.1 where the β-probability distribution for different fractions of the revival time is illustrated) due to the interference of the angular momentum states. For odd integer multiples of $t = T_{\text{rev}}/8$ we can proceed analogously and get the same result, a superposition of four narrow wave packets located at $\beta = \pi/8$, $\beta = 3\pi/8$, $\beta = 5\pi/8$ and $\beta = 7\pi/8$. Similarly, we obtain the state for $t = T_{\text{rev}}/4$ by splitting the summation index set in (6.7) residue classes modulo four instead of eight resulting in four groups of equal phase. Alternatively one can apply the result (6.10) and (6.11) twice on the initial state. Thus, after one quarter of the revival time the initial state evolves into a superposition of two well-localized wave packets at $\beta = \pi/4$ and $\beta = 3\pi/4$. After a half of the revival time the state is localized in the equatorial plane $\beta = \pi/2$ and amounting to the perfect anti-aligned state with $\langle \cos^2 \beta \rangle = 0$.

This shows that the points in time $t = T_{\text{rev}}/8$ and $t = T_{\text{rev}}/4$ are suitable for imprinting a relative phase between the wave packets with a β-depending potential to steer the alignment. While the two wave packets at $t = T_{\text{rev}}/4$ have the same alignment and only different orientations the wave packets at $t = T_{\text{rev}}/8$ differ in the alignment. From this follows that we need a not inversion-symmetric potential for steering the alignment at $t = T_{\text{rev}}/4$. For example one could use a potential of the form $V(\beta) = V_0 \cos \beta$ created by an static electric field pulse acting on a particle with permanent electric dipole moment. At $t = T_{\text{rev}}/8$ one could use a potential which depends on the polar angle β in the form of the squared cosine, $V(\beta) = V_0 \cos^2 \beta$, and so does not differentiate between different orientations. We have seen in chapter 4 that such kind of potential applies if an anisotropic dielectric particle is illuminated by a linear polarized plane wave. In the following, I will focus on an interference scheme for a phase imprinted at $t = T_{\text{rev}}/8$.

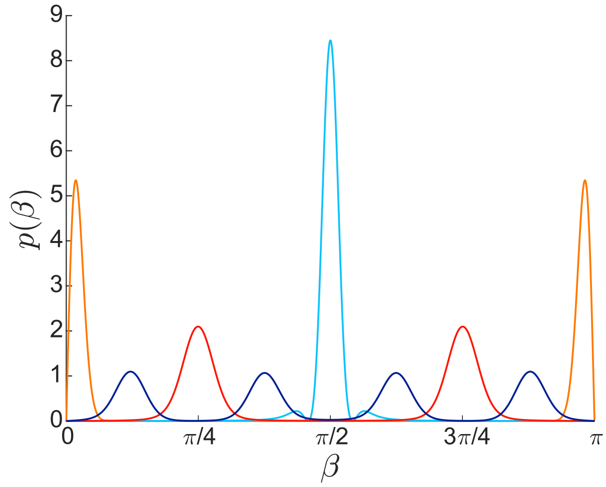

Figure 6.1.: Probability distribution $p(\beta) = \sin(\beta)|\langle\beta|\psi\rangle|^2$ at fractional revival times t for a initially tightly aligned state. At $t = 0$ the state is in superposition of two wave packets well-localized near $\beta = 0$ and $\beta = \pi$ (orange). After one half of the revival time $t = T_{\mathrm{rev}}/2$ the is well-localized in β at $\beta = \pi/2$ (light blue). The red line represents the state at $t = T_{\mathrm{rev}}/4$ in a superposition of two wave packets localized at $\beta = \pi/4$ and $\beta = 3\pi/4$. And at the smallest fraction of the revival, $t = T_{\mathrm{rev}}/8$, the state is in a superposition of four localized wave packets at $\beta = n\pi/8$ with $n \in \{1, 3, 5, 7\}$ (blue).

8-state Model

To discuss the state at multiples of an eigth of the revival time I introduce the operator $\mathsf{W}^\ell = \mathsf{U}_\beta(\ell T_{\mathrm{rev}}/8)$. The states $|\psi_\ell\rangle = \mathsf{W}^\ell|\psi_0\rangle$ $(\ell = 1, ..., 7)$ can be represented as superpositions of eight wave packets $|\xi_n\rangle$ centered at $\beta = n\pi/8$. With this we can write $|\psi_\ell\rangle = e^{i\nu_\ell}\sum_{n=1}^{7} M_{\ell n}|\xi_n\rangle$ with the coefficients

$$\mathsf{M} = \frac{1}{2}\begin{pmatrix} 1 & 0 & 1 & 0 & 1 & 0 & 1 \\ 0 & \sqrt{2} & 0 & 0 & 0 & \sqrt{2} & 0 \\ 1 & 0 & i & 0 & -i & 0 & -1 \\ 0 & 0 & 0 & 2 & 0 & 0 & 0 \\ 1 & 0 & -1 & 0 & -1 & 0 & 1 \\ 0 & \sqrt{2} & 0 & 0 & 0 & -\sqrt{2} & 0 \\ 1 & 0 & -i & 0 & i & 0 & -1 \end{pmatrix} \tag{6.12}$$

and

$$\begin{aligned} \nu_1 = \nu_2 = \nu_4 = 0, \qquad \nu_3 = -\frac{\pi}{8}, \\ \nu_5 = \frac{\pi}{2}, \qquad \nu_6 = \frac{\pi}{4}, \qquad \nu_7 = 3\frac{\pi}{8}. \end{aligned} \tag{6.13}$$

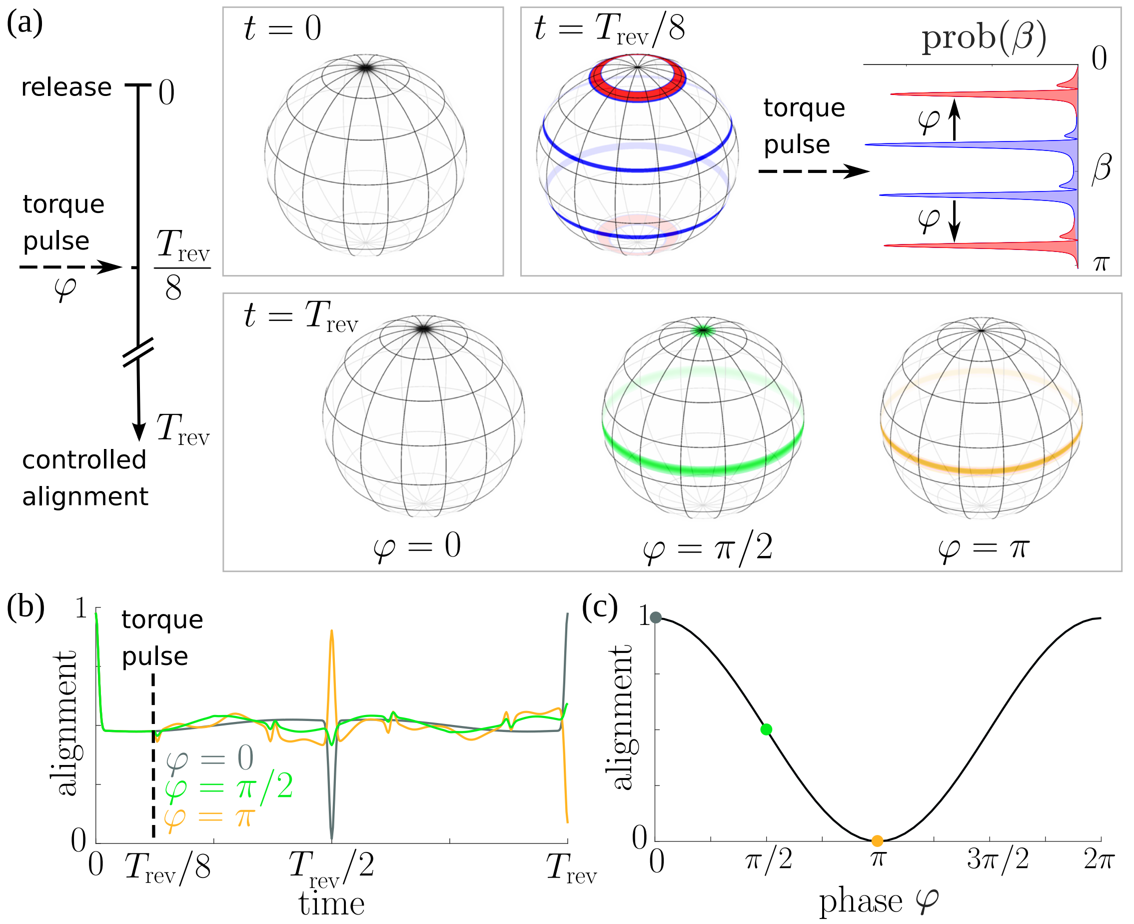

Figure 6.2.: (a) Density plots of the orientational distribution of the rotor's symmetry axis for different times t. In the first row on the left hand side is a Mollweide projection of the initial state ($t = 0$) well-localized at $\beta = 0$. After a time $t = T_{\text{rev}}$ the state is in superposition of wave packets localized at $\beta = n\pi/8$, $n \in \{1, 3, 5, 7\}$ (middle: Mollweide projection, right: probability density function dependent on the polar angle β. In the second row we see the resulting states at $t = T_{\text{rev}}$ for different relative phase φ which are induced between the wave packets at $t = T_{\text{rev}}/8$. Without phase the initial state recurs (left), a phase of $\pi/2$ (middle) leads to a superposition of $\beta = 0$ and $\beta = \pi/2$ and a phase of π (right) leads to a state in the equator plane. (b) The time evolution of the alignment $\langle \cos^2 \beta \rangle_t$ is shown for three different relative phases, $\varphi = 0$ (gray), $\varphi = \pi/2$ (green) and $\varphi = \pi$ (orange) for an initial state $\langle j00|\psi\rangle = \exp(-j^2/(2\sigma_j))$ and $\sigma_j = 20$. (c) Here, we see the ideal revival signal $\langle \cos^2 \beta \rangle_{T_{\text{rev}}}$ as a function of φ. Figure taken from [83].

To specify the coefficients $M_{\ell n}$ and ν_ℓ we start with setting $|\psi_1\rangle = \frac{1}{2}(|\xi_1\rangle + |\xi_3\rangle + |\xi_5\rangle + |\xi_7\rangle)$. By calculating $u_c(\Delta\beta; 3T_{\mathrm{rev}}/8)$ and $u_s(\bar{\beta}; 3T_{\mathrm{rev}}/8)$ analogous to $u_c(\Delta\beta; T_{\mathrm{rev}}/8)$ and $u_s(\bar{\beta}; T_{\mathrm{rev}}/8)$ and comparing the result to (6.10) and (6.11) we obtain M_{3n} and ν_3. In a similar way one gets M_{5n},M_{7n},ν_5, and ν_7. For the remaining coefficients we fix M_{4n}, M_{2n}, and ν_2 and compare $u_c(\Delta\beta; 3T_{\mathrm{rev}}/4)$, $u_s(\bar{\beta}; 3T_{\mathrm{rev}}/4)$ with $u_c(\Delta\beta; T_{\mathrm{rev}}/4)$, $u_s(\bar{\beta}; T_{\mathrm{rev}}/4)$ to calculate M_{6n} and ν_6.

By writing the states $|\xi_n\rangle$ in terms of the states $|\psi_l\rangle$ we know how the operator W acts on the states $|\xi_n\rangle$, for example

$$\mathsf{W}|\xi_1\rangle = \frac{1}{2}\left[e^{-i\nu_7}|\psi_0\rangle + e^{-i\nu_3}|\xi_4\rangle + \frac{1}{\sqrt{2}}\left(1 + e^{-i\nu_4}\right)|\xi_2\rangle + \frac{1}{\sqrt{2}}\left(1 - e^{-i\nu_4}\right)|\xi_6\rangle\right]. \tag{6.14}$$

Note that this simplified system of eight states works for an arbitrary initial state. It does not matter where the initial state is localized and it does not even have to be localized. Now I introduce a phase operator

$$\phi = \exp\left(i\sqrt{2}\varphi\cos^2\beta\right) \tag{6.15}$$

which adds an β-dependent phase to localized states. We assume that the initial state is perfectly localized around $\beta = 0$ (initial alignment $\langle\cos^2\beta\rangle = 1$). This entails that the states $|\xi_n\rangle$ are well-localized at $\beta = n\pi/8$ and the operator ϕ acts as follows on the $|\xi_n\rangle$

$$\begin{aligned} \phi|\psi_0\rangle &= e^{i\sqrt{2}\varphi}|\psi_0\rangle & \phi|\xi_4\rangle &= |\xi_4\rangle \\ \phi|\xi_2\rangle &= e^{i\varphi/\sqrt{2}}|\xi_2\rangle & \phi|\xi_6\rangle &= e^{i\varphi/\sqrt{2}}|\xi_6\rangle \\ \phi|\xi_1\rangle &= e^{i(\sqrt{2}+1)\varphi/2}|\xi_1\rangle & \phi|\xi_3\rangle &= e^{i(\sqrt{2}-1)\varphi/2}|\xi_3\rangle \\ \phi|\xi_7\rangle &= e^{i(\sqrt{2}+1)\varphi/2}|\xi_7\rangle & \phi|\xi_5\rangle &= e^{i(\sqrt{2}-1)\varphi/2}|\xi_5\rangle. \end{aligned} \tag{6.16}$$

As discussed before and illustrated in Fig. 6.1 the particle is in a superposition of different well-localized orientational states at both $t = T_{\mathrm{rev}}/4$ and $t = T_{\mathrm{rev}}/8$. At $t = T_{\mathrm{rev}}/4$ the state is in a superposition of the states $|\xi_2\rangle$ and $|\xi_6\rangle$ localized at $\beta = \pi/4$ and $\beta = 3\pi/4$ and thus the phase operator (6.15) cannot apply a relative phase between these two wave packets. But we see in (6.16) that it induces the relative phase φ between the states $|\xi_1\rangle$,$|\xi_7\rangle$ and $|\xi_3\rangle$, $|\xi_5\rangle$

$$\phi\mathsf{W}|\psi_0\rangle = \frac{e^{i\sqrt{2}}}{2}\left[e^{i\varphi/2}(|\xi_1\rangle + |\xi_7\rangle) + e^{-i\varphi/2}(|\xi_3\rangle + |\xi_5\rangle)\right]. \tag{6.17}$$

Thus, the time $t = T_{\mathrm{rev}}/8$ seems to be ideal for imprinting the phase and with this to control the further time evolution. Especially the state at the revival time is in general no longer the initial state but a superposition of wave packets at $\beta = 0$ and $\beta = \pi/2$

$$\mathsf{W}^7 \mathsf{\Phi} \mathsf{W} |\psi_0\rangle = e^{i\varphi/\sqrt{2}} \left[\cos(\varphi/2)|\psi_0\rangle + \sin(\varphi/2)|\xi_4\rangle\right]. \tag{6.18}$$

Thus, one can control the state and the alignment at the revival time by imprinting the phase difference (see Fig. 6.2) by applying a torque depending on the squared cosin of β for a brief duration. For a perfectly aligned initial state the alignment at the revival time depends with $\langle \cos^2 \mathsf{\beta} \rangle = \cos^2(\varphi/2)$ on the induced phase difference. For a relative phase of $\varphi = n2\pi$ with the integer n the initial state reappears, for a relative phase of $(2n + 1)\pi$ the state is localized at $\beta = \pi/2$ and for all other imprinted relative phases φ the state at $t = T_{\text{rev}}$ is in a superposition of a wave packet localized at the pole of a sphere and a wave packet in the equatorial plane.

Note that the phase operator $\mathsf{\Phi}$ is in general not 2π-periodic. For realistic initial states we will see deviations from the cosine-dependence on the relative phase for the alignment signal at $t = T_{\text{rev}}$, which I will discuss later in this chapter.

6.2. Implementation of the Phase Operator

In the previous section, we have seen how a β-dependent torque imprints a phase difference on the wave packets emerging at fractional revival times $t = T_{\text{rev}}/8$. In this section, the focus is on the implementation of the phase, both experimentally and numerically as required for the following simulations of the interference signal.

As mentioned before and discussed in detail in chapter 4, a dielectric particle with an anisotropic polarizability illuminated by a linear polarized experiences a β-dependent potential of the form $V(\beta) = -V_0 \cos^2 \beta$. Thus, a linear polarized laser pulse of duration Δt is suitable to imprint the relative phase. The time evolution until $t = T_{\text{rev}}$ is then given by

$$\rho(t_{\mathrm{T}_{\text{rev}}}) = \mathsf{U}(t_1)\mathsf{U}_\varphi(\Delta t)\mathsf{U}(t_2)\rho_0\mathsf{U}^\dagger(t_2)\mathsf{U}_\varphi^\dagger(\Delta t)\mathsf{U}^\dagger(t_1) \tag{6.19}$$

with $\mathsf{U}(t)$ the free time evolution operator propagating for the periods $t_1 = T_{\text{rev}}/8 - \Delta t/2$ and $t_2 = T_{\text{rev}} - (T_{\text{rev}}/8 + \Delta t/2)$. In the time interval Δt around $t = T_{\text{rev}}/8$ the time evolution operator reads $\mathsf{U}_\varphi = \exp(-it\mathsf{H}_\varphi/\hbar)$ with the Hamiltonian $\mathsf{H}_\varphi = \mathsf{H}_{\text{rot}} - V_0 \cos^2 \mathsf{\beta}$.

However, in the limit that the pulse duration Δt is much smaller than the dispersion time scale $1/\kappa$ we can assume a constant orientation during the pulse and we can use the phase operator $\mathsf{\Phi}$ (6.15) with the relative phase $\varphi = V_0\Delta t$. The free time evolution operator acts then in the time durations $t_1 = T_{\text{rev}}/8$ and $t_2 = 7T_{\text{rev}}/8$.

Thus, $\mathsf{U}(t_1)$ becomes the operator W of the eight-state system and $\mathsf{U}(t_2)$ is W^7.

Numerical Implementation

For the numerical simulation of the interference signal I prefer again the angular momentum eigenbasis $|jmk\rangle$ of a symmetric rigid rotor. The free time evolution operator is diagonal in this basis so that only the calculation of the matrix elements of the phase operator ϕ in angular momentum representation is challenging. The technique of exact numerical diagonalization is here intractable because of the high number of occupied angular momentum states. We use again semiclassical matrix elements based on Bohr-Sommerfeld quantized action-angle variables as in chapter 4, now for the symmetric rigid rotor rather than for the linear top. The Euler angles α, β, γ and the corresponding conjugate momenta are related to the action-angle variables α_J, α_M, α_K and J, M, K via [62]

$$\begin{aligned}
\alpha_J =& \arccos\left[\frac{J^2\cos\beta - MK}{[(J^2-K^2)(J^2-M^2)]^{1/2}}\right], && \text{(6.20a)}\\
\alpha_M =& \alpha + \pi - \arccos\left[\frac{M\cos\beta - K}{\sin\beta(J^2-M^2)^{1/2}}\right], && \text{(6.20b)}\\
\alpha_K =& \gamma + \pi - \arccos\left[\frac{K\cos\beta - M}{\sin\beta(J^2-K^2)^{1/2}}\right], && \text{(6.20c)}\\
J^2 =& p_\beta^2 + \frac{1}{\sin^2\beta}\left(p_\alpha^2 + p_\gamma^2 - 2p_\alpha p_\gamma\cos\beta\right), && \text{(6.20d)}\\
M =& p_\alpha, && \text{(6.20e)}\\
K =& p_\gamma, && \text{(6.20f)}
\end{aligned}$$

with the quantization rules $M = \hbar m$, $K = \hbar k$ and $J = \hbar(j + 1/2)$. Extending equation (2.72) for the calculation of semiclassical matrix elements to a third degree of freedom, from (6.20) follow the semiclassical matrix elements for the phase operator ϕ

$$\begin{aligned}
\langle jmk|\phi|j'm'k'\rangle =& \frac{1}{8\pi^3}\int_0^{2\pi}\mathrm{d}\alpha_j\int_0^{2\pi}\mathrm{d}\alpha_m\int_0^{2\pi}\mathrm{d}\alpha_k\, e^{i[(j'-j)\alpha_j+(m'-m)\alpha_m+(k'-k)\alpha_k]}\\
&\times\exp\left\{-i\sqrt{2}\varphi\left[\cos\alpha_j\sqrt{A_{j+j'+1}^{\bar{m}\bar{k}}} + \frac{\bar{m}\bar{k}}{(\bar{j}+1/2)^2}\right]^2\right\},
\end{aligned} \tag{6.21}$$

with $A_j^{mk} = (1 - 4k^2/j^2)(1 - 4m^2/j^2)/2$ and $\bar{m} = (m + m')/2$, $\bar{k} = (k + k')/2$, $\bar{j} = (j + j')/2$. The α_m and α_k integral can be easily carried out resulting in Kronecker deltas $\delta_{mm'}$ and $\delta_{kk'}$. For the α_j integral I express the second exponential function in (6.21) in a Fourier integral

$$\begin{aligned}\langle jmk|\phi|j'm'k'\rangle =&\frac{1}{4\pi^2}\sqrt{\frac{\pi}{i\sqrt{2}\varphi}}\int_{-\infty}^{\infty}\mathrm{d}\chi\; e^{-\chi^2/(4\sqrt{2}i\varphi)}e^{i\chi km/(\bar{j}+1/2)^2}\int_0^{2\pi}\mathrm{d}\alpha_j\; e^{i(j'-j)\alpha_j}\\ &\times e^{i\chi(A^{mk}_{j+j'+1})^{1/2}\cos\alpha_j}\delta_{mm'}\delta_{kk'}.\end{aligned} \tag{6.22}$$

Carrying out the α_j integration yields a Bessel function $J_n(.)$ [85]

$$\int_0^{2\pi}\mathrm{d}\alpha_j\; e^{i(j'-j)\alpha_j}e^{i\chi(A^{mk}_{j+j'+1})^{1/2}\cos\alpha_j} = 2\pi i^{|j-j'|}J_{|j-j'|}\left(\chi\sqrt{A^{km}_{j+j'+1}}\right). \tag{6.23}$$

For the integration over χ we have to approximate the integrand for $k, m \ll j$. This approximation is valid for all the initial states I will look at later. We then can expand the exponential $\exp[i\chi km/(\bar{j}+1/2)^2] \approx 1+i\chi km/(\bar{j}+1/2)^2-\chi^2k^2m^2/[2(\bar{j}+1/2)^4]$. The integration over the linear part in χ vanishes because of the symmetry of the integrand and we obtain

$$\begin{aligned}\langle jmk|\phi|j'm'k'\rangle \approx&\frac{1}{2\pi}\sqrt{\frac{\pi}{i\sqrt{2}\varphi}}i^{|j-j'|}\int_{-\infty}^{\infty}\mathrm{d}\chi\;\left(1-\chi^2\frac{k^2m^2}{2(j+1/2)^4}\right)e^{-\chi^2/(4\sqrt{2}i\varphi)}\\ &\times J_{|j'-j|}\left[\chi(A^{mk}_{j+j'+1})^{(1/2)}\right]\delta_{mm'}\delta_{kk'}\end{aligned} \tag{6.24}$$

After writing the term proportional to χ^2 as a $1/\varphi$ derivative we can carry out the χ integration with the result

$$\begin{aligned}\langle jmk|\phi|j'm'k'\rangle =&\delta_{mm'}\delta_{kk'}e^{-i\pi|j-j'|/4}\left[1+i\sqrt{2\xi}\frac{32k^2m^2}{(j+j'+1)^4}\frac{d}{d\xi}\frac{1}{\sqrt{\xi}}\right]\\ &\times e^{-i\sqrt{2}A^{km}_{j+j'+1}/\xi}J_{\frac{|j-j'|}{2}}\left(\frac{\sqrt{2}A^{km}_{j+j'+1}}{\xi}\right)\Bigg|_{\xi=1/\varphi}\delta_{mm'}\delta_{kk'}\end{aligned} \tag{6.25}$$

for $j-j'$ an even integer. If $j-j'$ is odd the corresponding matrix element vanishes. This approximation works better the more angular momentum states are occupied, see Fig. 6.3.

6.3. Discussion of the Interference Signal

In section 6.1 I discussed the interference signal for an ideal, perfectly aligned symmetric rotor with $m = 0$ and $k = 0$. For this case we have seen that the interference signal, i.e. the alignment in dependence on the relative phase φ at the revival time T_{rev}, is a perfect squared cosine, $\langle\cos^2\beta\rangle^{\varphi}_{T_{\mathrm{rev}}} = \cos^2(\varphi/2)$. A realistic particle differs

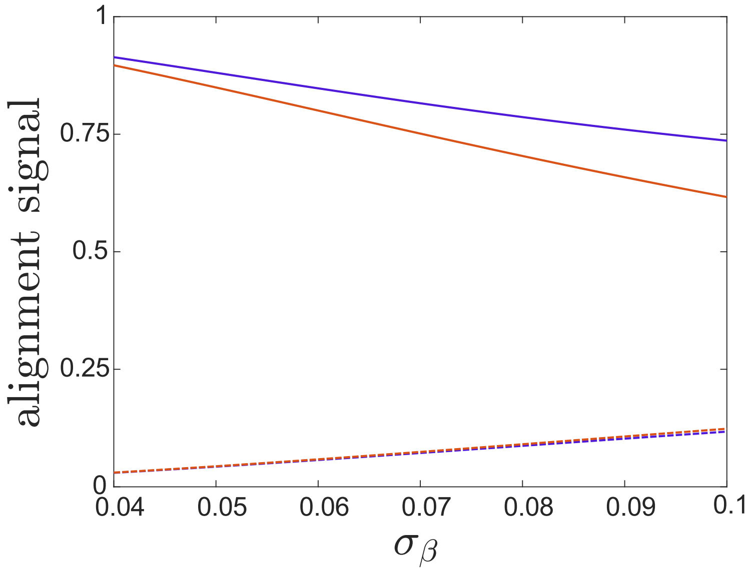

Figure 6.3.: Comparison of the alignment signal at T_{rev} for relative phases of $\varphi = \pi$ (dashed lines) and $\varphi = 2\pi$ (solid line) calculated numerically exactly (blue lines) with the one calculated with help of semiclassical matrix elements (6.25) for initial states $\psi(\beta) \propto e^{-\cos^2\beta/(2\sigma_\beta^2)}$. The most strongly aligned initial state ($\sigma_\beta = 0.04$) has an expectation value of $\langle j \rangle = 21,6$ for the occupied angular momentum states $|00j\rangle$ and for the least aligned one ($\sigma_\beta = 0.1$) this expectation value is much smaller, $\langle j \rangle = 8.3$.

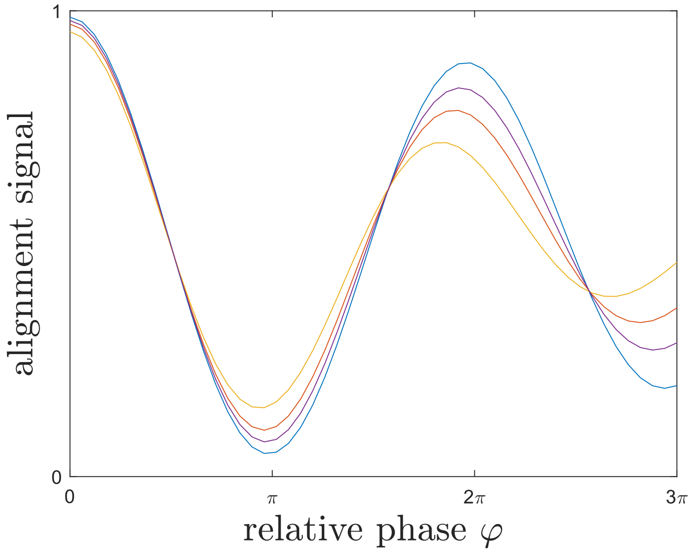

Figure 6.4.: Interference signal as a function of the relative phase φ for different initial states of the form $\psi \propto e^{-j^2/(2\sigma_j^2)}$ with $\sigma_j = 30$ (blue), $\sigma_j = 20$ (purple), $\sigma_j = 15$ (orange) and $\sigma_j = 5$ (yellow).The smaller the σ_j the broader is the β-distribution of the initial state. This implies that the initial alignment decreases with decreasing σ_j.

in several aspects from this idealized case which leads to deviations from this ideal signal.

In a first step, we still assume a symmetric rotor with $m = 0$ and $k = 0$, which is however not perfectly aligned. The phase operator $\phi = \exp(i\sqrt{2}\varphi\cos^2\beta)$ acts then no longer in a 2π-periodic way in φ. The four wave packets at $t = T_{\mathrm{rev}}/8$ have now a finite width and the average relative phase imprinted between the packets is the larger the broader the wave packets. On the one hand this leads to a shift of the local maximum of the alignment as a function of the phase φ to smaller phases and, on the other hand, the initial state does not reappear completely except for $\varphi = 0$. One therefore observes a decrease of the maximum alignment and with this a decrease of the contrast of the interference signal (see Fig. 6.4).

In a next step, we allow finite quantum numbers $k \neq 0$, implying rotations around the symmetry axis of the rigid rotor. Note that in the limit of a tightly aligned initial states this implies $m \neq 0$ as well, because of the near identity of the body-fixed $\mathbf{n}_3$-axis and the space-fixed $\mathbf{e}_3$-axis. Finite occupations of k might have an effect on different contributions to the interference signal. At first, it may affect the initial alignment. The classical thermal state $f_{\mathrm{L}}(\alpha, \beta, p_\alpha, p_\beta) = \exp[-(H_{\mathrm{L}}(\alpha, \beta, p_\alpha, p_\beta) + V(\beta))/(k_B T)]/Z$ with the free Hamiltonian (2.11) of the linear rigid rotor shows the same initial alignment as the state $f_{\mathrm{S}}(\alpha, \beta, \gamma, p_\alpha, p_\beta, p_\gamma) = \exp[-(H_{\mathrm{S}}(\alpha, \beta, \gamma, p_\alpha, p_\beta, p_\gamma) + V(\beta))/(k_B T)]/Z'$ with the free Hamiltonian (2.10) of a symmetric top. Numerical simulations indicate that the same holds true for quantum mechanicals states, so that the initial alignment is not affected by the finite value for k.

But let us again have a look at the free quantum Hamiltonian of the symmetric top (2.25) and the corresponding time evolution operator

$$\mathsf{U} = \sum_{j\in\mathbb{N}} \sum_{m=-j}^{m=j} \sum_{k=-j} \exp\left\{-i\hbar t\left[\frac{1}{2I}j(j+1) + \frac{1}{2}\left(\frac{1}{I_3} - \frac{1}{I}\right)k^2\right]\right\} |jmk\rangle\langle jmk| \tag{6.26}$$

Unlike the free time evolution operator of the linear rigid rotor, the one for symmetric rotors (6.26) does not reduce to the unity operator for integer multiples of the revival time $T_{\mathrm{rev}} = 2\pi I/\hbar$. But if the initial state ρ_0 is diagonal in k the k-dependent parts of the time evolution operators in $\rho(t) = \mathsf{U}(t)\rho_0\mathsf{U}^\dagger(t)$ cancel so that the initial state reappears for integer multiples of T_{rev}. What is more, even if the initial state is not diagonal in k all expectation values of operators diagonal in k show revivals, although the state itself does not recur.

The critical part is imprinting the phase. The phase operator ϕ depends on the quantum numbers k and m and therefore has an effect on the interference signal. I observe numerically that the broader the state is in k the broader is the β-distribution at fractional revival times. This again leads to a decreasing contrast.

6.3.1. Asymmetric Rotors

Since any realistic particle will never be perfectly symmetric, we have to consider the effect of deviations of the azimuthal symmetry on the interference signal. In general, the eigenstates and eigenvalues of the free Hamiltonian of an arbitrarily shaped asymmetric rotor cannot be stated analytically. But for such arbitrarily shaped particles no revival signal is expected anyhow, so that only small deviations in the symmetry of the rotor are discussed in the following.

Here, I consider a slightly asymmetric prolate particle with moments of inertia I_1, I_2 and I_3 with $I_1 > I_2 > I_3$ and $I_1 \approx I_2$. The free Hamiltonian can then be written in the form [86]

$$\mathsf{H} = \mathsf{H}_0 + b\mathsf{H}_1 \tag{6.27}$$

with the asymmetry parameter

$$b = \left(\frac{1}{I_1} - \frac{1}{I_2}\right)\left(\frac{2}{I_3} - \frac{1}{I_1} - \frac{1}{I_2}\right)^{-1}, \tag{6.28}$$

and the Hamiltonians

$$\mathsf{H}_0 = \frac{1}{I_1 + I_2}\mathsf{J}^2 + \left(\frac{1}{2I_3} - \frac{I_1 + I_2}{2I_1 I_2}\right)\tilde{\mathsf{J}}_3^2 \tag{6.29a}$$

$$\mathsf{H}_1 = \left(\frac{1}{2I_3} - \frac{I_1 + I_2}{2I_1 I_2}\right)\left(\mathsf{J}_1^2 - \mathsf{J}_2^2\right). \tag{6.29b}$$

The asymmetry parameter b is zero for a perfect symmetric rotor with $I_1 = I_2$ and increases with increasing asymmetry. For a slightly asymmetric rotor we assume that the time evolution is dominated by the energy eigenvalues of the asymmetric rotor and we can approximately use the energy eigenstates of the Hamiltonian for the symmetric rotor. The energy eigenvalues can be calculated with perturbation theory [86]

$$E_{jk} = E_{jk}^{(0)} + b^2 E_{jk}^{(2)}. \tag{6.30}$$

Here, the $E_{jk}^{(0)}$ are the unperturbated eigenvalues of the symmetric rotor and the $E_{jk}^{(2)}$ are given in Ref. [86] for all j and k. I only use them for simulations with initial states where only $k = 0$ is occupied. In this case the $E^{(2)}_{j0}$ read [86]

$$E^{(2)}_{j0} = -\frac{\hbar^2}{16}(I_3 - I_1)j(j+1)(j-1)(j+1) \tag{6.31}$$

The new energy eigenvalues leads to a decrease of the revival signal and to a shift of the revival time. For the implementation of the interference scheme one should consider this new revival time for applying the phase imprinting torque at an eighth of it and measuring the alignment at the full shifted revival time.

6.3.2. Decoherence

Another aspect we have to take into account is the interaction with the environment, which leads to environmental decoherence and so to a reduction of the interference signal.

As for the proposed revival experiment discussed in chapter 4, thermal emission of photons and collisions with residual gas particles are dominant sources of environmental decoherence. But here we have to examine also a third source: the interaction with the phase imprinting laser pulse.

Regardless of the type of interaction the rotational dynamics of a symmetric rotor due to a weak interaction with the environment may be described by the angular momentum diffusion master equation (3.26). Since such master equations act on the statistical operator ρ any numerical calculation operates on the dimension of the Hilbert space squared. One way to circumvent this increasing numerical requirement is the so called unraveling of the master equation on the level of pure states where the non-hermitian behaviour is implemented via stochastic quantum jumps. In the following, I introduce this method for general master equations of Lindblad form and then apply it on the angular momentum diffusion master equation.

Monte Carlo Unraveling of the Master Equation

Any initial state ρ can be written as a convex sum of pure states $\rho = \sum_k p_k |\psi_k\rangle\langle\psi_k|$. The time evolution of these pure states $|\psi_k\rangle$ is described by a quantum stochastic differential equation

$$\begin{aligned} \mathrm{d}|\psi_k(t)\rangle =& \frac{1}{i\hbar}\mathsf{H}|\psi_k(t)\rangle \mathrm{d}t - \frac{1}{2}\sum_i \gamma_i \left(\mathsf{L}_i^\dagger \mathsf{L}_i - \langle \mathsf{L}_i^\dagger \mathsf{L}_i\rangle\right)|\psi_k(t)\rangle \mathrm{d}t \\ &+ \sum_i \left(\frac{\mathsf{L_i}|\psi_k(t)\rangle}{||\mathsf{L}_i|\psi_k(t)\rangle||} - |\psi_k(t)\rangle\right)\mathrm{d}N_i(t). \end{aligned} \tag{6.32}$$

With this stochastic differential equation one can create samples of single quantum trajectories $|\psi_k^{(n)}\rangle$. The time dependence of the pure state is then given by the ensemble average over all these trajectories and thus the density operator ρ_t reads

$$\rho_t = \sum_k p_k \mathbb{E}\left[|\psi_k^{(n)}(t)\rangle\langle\psi_k^{(n)}(t)|\right]. \tag{6.33}$$

The stochastic differential equation (6.32) describes a piecewise deterministic process. This means that we have a deterministic time evolution described by the first two terms of expression (6.32) interrupted by random quantum jumps described by the stochastic third term.

The stochastic term is determined by the Poisson increment $\mathrm{d}N_i(t)$, defined as $\mathrm{d}N_i(t) = N_i(t+\mathrm{d}t) - N_i(t)$. The $N_i(t)$ are the number of events induced by the Lindblad operator L_i that have occurred up to the time t. Thus, the expectation value of the Poisson increment is determined by the rate $r_i(t)$ of the process, $\mathbb{E}[\mathrm{d}N_i(t)] = r_i(t)\mathrm{d}t$ [64]. Further, the total rate $\Gamma(t) = \sum_i r_i(t)$ is defined as the sum of the rates $r_i(t)$. In general, the rates $r_i(t)$ depend on the present state $|\psi_k(t)\rangle$ and so on the time t. The stochastic differential equation given in (6.32) is a special kind of piecewise deterministic unraveling, the Monte Carlo unraveling. In this case the ensemble average of the Poisson increment reads [50, 64]

$$\begin{aligned}\mathbb{E}[\mathrm{d}N_i(t)] &= \gamma_i \langle \mathsf{L}_i^\dagger \mathsf{L}_i\rangle_{\psi(t)}\mathrm{d}t \\ &= r_i(t)\mathrm{d}t\end{aligned} \tag{6.34}$$

Here, $\langle . \rangle$ is to understand as the expectation value for the current state $|\psi_k(t)\rangle$.

I use this Monte Carlo unraveling to solve the angular momentum master equation (3.26) with the superoperator (3.35a), which is linear in the orientation. We have then three different Lindblad operators, which are given by the operator-valued components of the orientation vector $\mathbf{m}(\Omega)$

$$\mathsf{m}_1 = \cos\alpha\sin\beta, \quad \mathsf{m}_2 = \sin\alpha\sin\beta, \quad \mathsf{m}_3 = \cos\beta \tag{6.35}$$

with

$$\sum_{i=1}^{3} \mathsf{m}_i^\dagger \mathsf{m}_i = \mathbb{1}. \tag{6.36}$$

The rate γ_i is characterized by the diffusion constant $\gamma_i = 2D/\hbar^2$ for all $i \in \{1,2,3\}$. Inserting the Lindblad operators (6.35) and $\gamma_i = 2D/\hbar^2$ in the stochastic differential equation (6.32) and using the identity (6.36) leads to the Monte Carlo unraveling of the orientational master equation (3.35a)

$$\mathrm{d}|\psi(t)\rangle = -\frac{i}{\hbar}\mathsf{H}|\psi(t)\rangle \mathrm{d}t + \sum_{i=1}^{3}\left(\frac{\mathsf{m}_i|\psi_(t)\rangle}{||\mathsf{m}_i|\psi(t)\rangle||} - |\psi(t)\rangle\right)\mathrm{d}N_i(t). \tag{6.37}$$

From (6.33) it follows that $\mathrm{d}\rho(t) = \mathrm{d}\mathbb{E}[|\psi(t)\rangle\langle|\psi(t)|]$. Inserting the stochastic differential equation (6.37) for $\mathrm{d}|\psi(t)\rangle$ and using $\mathrm{d}N_i\mathrm{d}N_j = \delta_{ij}\mathrm{d}N_i$ one retains the master equation (3.35a).

Using the stochastic differential equation (6.37) one can calculate random trajectories numerically and by building the ensemble average the density operator $\rho(t)$ can be obtained.

I start with the deterministic time evolution for the random time τ between two quantum jumps. It is given by

$$|\tilde{\psi}(t+\tau)\rangle = \frac{\exp\left(-i\tau\mathsf{H}_{\text{eff}}/\hbar\right)}{||\exp\left(-i\tau\mathsf{H}_{\text{eff}}/\hbar\right)|\psi_t\rangle||}|\psi_t\rangle \tag{6.38}$$

with the effective Hamiltonian H_{eff},

$$\mathsf{H}_{\text{eff}} = \mathsf{H} - \frac{i\hbar}{2}\frac{2D}{\hbar^2}\sum_{i=1}^{3}\mathsf{m}_i^2 = \mathsf{H} - i\frac{D}{\hbar}. \tag{6.39}$$

Note that H_{eff} is not hermitian and we need the renormalization factor in (6.38).

After a random time τ we jump to a new normalized state

$$|\psi(t+\tau)\rangle = \frac{\mathsf{m}_i}{||\mathsf{m}_i|\tilde{\psi}(t+\tau)\rangle||}|\tilde{\psi}(t+\tau)\rangle. \tag{6.40}$$

We still have to clarify how to calculate the random time steps τ between the jumps and how to choose which one of the three jump operators m_i acts. From (6.34) it follows that $r_i(t) = 2D\langle\mathsf{m}_i^\dagger\mathsf{m}_i\rangle_{\tilde{\psi}(t)}$ determines the rate for a quantum jump with jump operator m_i. This rate depends on the current state $|\psi(t)\rangle$, but with (6.36) the total rate $\Gamma(t)$ reads

$$\Gamma = \frac{2D}{\hbar}. \tag{6.41}$$

This rate is independent of the current state and with this independent of the time.

The jump operators are now selected with a probability $P(\mathsf{m}_i) = r_i(t)/\Gamma$ leading to

$$P(\mathsf{m}_i) = \langle\mathsf{m}_i^\dagger\mathsf{m}_i\rangle_{\tilde{\psi}(t+\tau)}, \tag{6.42}$$

with $\sum_{i=1}^{3} P(\mathsf{m}_i) = 1$. Thus, this probability depends on the state $|\psi(t+\tau)\rangle$ just before the jump. The time period τ for the deterministic time evolution is determined by the total rate Γ via the cumulative probability $F(\tau|t)$ for a quantum jump in the time interval $[t, t+\tau]$. This is given by one minus the probability that no jump occurred yet

$$\begin{aligned} F(\tau|t) =& 1 - \exp\left[-\int_t^{t+\tau} \mathrm{d}t' \Gamma(t')\right] \\ =& 1 - e^{-2D\tau/\hbar}. \end{aligned} \tag{6.43}$$

This probability function (6.43) only depends on τ and not on the time t, $F(\tau) \equiv F(\tau|t)$. The jump times τ are now drawn randomly corresponding to the distribution of the jump times $f(\tau) = \mathrm{d}F(\tau)/\mathrm{d}\tau$.

For this I use the inverse transformation method [87]. There one draws $x \in [0,1]$ with the uniform probability distribution $p(x) = 1$ for $x \in [0,1]$ and a vanishing probability outside of this interval. We are now looking for a transformation from $x \to \tau(x)$ with the associated distribution function

$$f(\tau) = \int_0^1 \mathrm{d}x \; p(x)\delta[\tau(x) - \tau]. \tag{6.44}$$

With the assumption that this transformation is unambiguous we obtain

$$f(\tau) = \frac{1}{\tau'[x(\tau)]}, \tag{6.45}$$

with $x(\tau) = \tau^{-1}(\tau)$. With the inverse function theorem it follows that $\tau'[x(\tau)] = 1/x'(\tau)$ and so $f(\tau) = x'(\tau)$. After an integration over τ we obtain

$$F(\tau) = \int_0^{\tau} \mathrm{d}\tau' \; f(\tau) = x. \tag{6.46}$$

Inserting the cumulative probability (6.43) and solving for τ leads to

$$\tau = -\frac{\hbar^2}{2D} \ln\left(1 - x\right). \tag{6.47}$$

Having discussed the different steps of the Monte Carlo unraveling in detail, I now summarize these steps and give a short algorithm for the numerical implementation.

1) draw $x \in [0,1]$ from a uniform distribution

2) calculate the time until the next jump $\tau = -\frac{\hbar}{2D}\ln(1-x)$

3) deterministic time evolution until τ: $|\tilde{\psi}(t+\tau)\rangle = \frac{\exp(-i\tau\mathsf{H}_{\text{eff}}/\hbar)}{||\exp(-i\tau\mathsf{H}_{\text{eff}}/\hbar)|\psi_t\rangle||}|\psi_t\rangle$

4) Choose jump operator m_i with probability $\langle \mathsf{m}_i^2 \rangle_{\tilde{\psi}(t)}$

5) Jump to a new state $|\psi(t+\tau)\rangle = \frac{\mathsf{m}_i|\tilde{\psi}(t+\tau)\rangle}{||\mathsf{m}_i|\tilde{\psi}(t+\tau)\rangle||}$

6) Repeat the steps 1)-6) until t_{final}

This protocol has to be repeated for a large number N of trajectories. After that the ensemble average can be calculated

$$\rho(t) = \frac{1}{N} \sum_k p_k \sum_{n=1}^{N} |\psi_k^{(n)}(t)\rangle\langle\psi_k^{(n)}(t)|. \tag{6.48}$$

The larger the number N of trajectories the smaller is the error.

The effect of the individual sources of environmental decoherence is discussed with help of Monte Carlo unraveling for a specific particle in the following section.

6.4. Implementation with Silicon Nanorods

In the previous sections we have seen how to control the orientation of dielectric aspherical particles and how to describe their time evolution. Further, I discussed possible deviations from the ideal conditions and how they affect the interference signal.

Here, I examine the feasibility of alignment control of nanosized particles with the example of a concrete ellipsoidally shaped silicon nanoparticle with principle diameters $\ell_a = 5\,\text{nm}$, $\ell_b = 5.5\,\text{nm}$ and $\ell_c = 50\,\text{nm}$. The particle has a volume of $V = \pi\ell_a\ell_b\ell_c/6 = 720\,\text{nm}^3$ and a mass of 1.1×10^6 amu. With the moments of inertia $I_a = m(\ell_b^2 + \ell_c^2)/20$, $I_b = m(\ell_a^2 + \ell_c^2)/20$, $I_c = m(\ell_b^2 + \ell_a^2)/20$ we obtain a revival time of $2\pi I_b/\hbar = T_{\text{rev}} = 13.8$ ms. Due to the aspherical shape of the particle the susceptibility tensor $\chi(\Omega) = R(\Omega)\chi_0 R^T(\Omega)$,$\chi_0 = \text{diag}(\chi_a, \chi_b, \chi_c)$ depends on the orientation Ω of the particle, as described by the rotation matrix $\mathsf{R}(\Omega)$ (2.2).

The experimental set up is similar to the set up for the observation of rotational quantum revivals discussed in chapter 4.1. We start with the preparation of the initial state in an optical trapping potential. Then the tweezer laser is turned off and the particle evolves freely. But in contrast to the revival experiment, one needs an additional laser for imprinting the relative phase in order to control the nanorotor's alignment. After the phase shift, the particle evolves freely again and the alignment is measured as described in section 4.1.3 at $t = T_{\text{rev}}$ and is recaptured and recycled directly after the measurement.

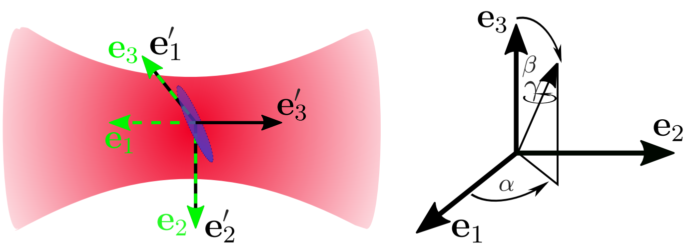

Figure 6.5.: Illustration of the particle in the tweezer. It aligns with the $\mathbf{e}_3$-axis of the unprimed (green) frame and the $\mathbf{e}_1$-axis of the primed (black) frame. Both frames differ through a rotation around the mutual $\mathbf{e}_2$-axis. On the right hand side the Euler angles are represented.

In the following, I focus on the differences to the set up for the quantum revivals, starting with the preparation of the initial state. In contrast to the initial state for observations of revivals, we have to take the rotation around the body-fixed $\mathbf{n}_3$-axis into account. I introduce the modified trapping potential and propose to cool all rotational degrees of freedom of the particle by elliptic coherent scattering [32, 33]. And we need an additional laser for imprinting the relative phase at $t = T_{\mathrm{rev}}/8$. In the end, I discuss the main effects for reducing the interference signal for this specific particle and experimental set up.

6.4.1. Initial State

For the alignment control it is important to not only align the particle with the space-fixed $\mathbf{e}_3$-axis, but also to reduce the rotation around the body-fixed $\mathbf{n}_3$-axis. Thus, we have to cool all three rotational degrees of freedom, the α-, β- and γ-motion. For a perfectly symmetric dielectric particle the optical dipole potential does not depend on γ and so we have to use a slightly asymmetric particle, the aforementioned ellipsoide. This asymmetric particle is initially trapped in an elliptically polarized optical tweezer with $\mathbf{e}_t = \cos\psi \mathbf{e}_1' + i \sin\psi \mathbf{e}_2'$ characterized by the ellipticity $\psi = \pi/8$, propagation direction $\mathbf{e}_3'$, laser Power $P_t = 0.1\,\mathrm{W}$ and the tweezer waists $w_{x'} = 1.6\,\mu\mathrm{m}$ and $w_{y'} = 1.3\ \mu\mathrm{m}$. Here, I introduced a primed reference system, which we will use for the derivation of the initial state. In the end, I will write the initial state in the space-fixed unprimed system see Fig. 6.5. The electric field $\mathbf{E}(\mathbf{r})e^{i\omega t}$ of the tweezer laser is given by [32, 33]

$$\mathbf{E}(\mathbf{r}) = \sqrt{\frac{2\hbar\omega}{\varepsilon_0 V_c}} \epsilon \mathbf{e}_t f_t(\mathbf{r}'), \tag{6.49}$$

with the cavity mode volume V_c, the mode variable $\epsilon = \sqrt{2P_t k V_c/(\pi\hbar\omega^2 w'_x w'_y)}$ and the mode function [32, 33]

$$f_t(\mathbf{r}') = \frac{1}{r(z')}\exp\left(-\frac{x'^2}{w_x'^2 r^2(z') - (y'/w_{y'})^2}\right) e^{i[kz' - \phi_t(\mathbf{r}')]}. \tag{6.50}$$

Here, $r(z') \simeq \sqrt{1 + z'^2/z_R^2}$ with $z_\mathrm{R} \simeq k w_x w_y/2$ is a dimensionless broadening function and $\phi_t(\mathbf{r})$ is the Gouy phase,

$$\phi_t(\mathbf{r}) \simeq \arctan\left(\frac{z}{z_\mathrm{R}}\right) - \frac{kz}{2}\frac{x^2 + y^2}{z^2 + z_\mathrm{R}^2}, \tag{6.51}$$

of the tweezer. The Hamiltonian $\mathsf{H} = \mathsf{H}_0 + \mathsf{V}_t$ depends on the free Hamiltonian H_0 of the asymmetric rotor (2.24) and the tweezer potential [33]

$$V_t(\mathbf{r}', \Omega') = -\frac{\varepsilon_0 V}{4}\mathbf{E}^*(\mathbf{r}') \cdot \chi(\Omega')\mathbf{E}(\mathbf{r}'). \tag{6.52}$$

The potential energy is minimal for $\alpha' = \gamma' = 0$ and $\beta' = \pi/2$. The particle in the tweezer potential is cooled into the ground state by elliptic coherent scattering [32, 33, 88]. In the deep trapping regime we can expand the potential harmonically around the minimum with frequencies

$$\omega_{\alpha'} = \sqrt{2VP_t(\chi_3 - \chi_2)\cos(2\psi)/(\pi c w_{x'} w_{y'} I_a)}, \tag{6.53a}$$

$$\omega_{\beta'} = \sqrt{2VP_t(\chi_3 - \chi_1)\cos^2(\psi)/(\pi c w_{x'} w_{y'} I_b)}, \tag{6.53b}$$

$$\omega_{\gamma'} = \sqrt{2VP_t(\chi_2 - \chi_1)\sin^2(\psi)/(\pi c w_{x'} w_{y'} I_c)}. \tag{6.53c}$$

The corresponding ground state reads

$$\langle\alpha'\beta'\gamma'|\tilde{\psi}_{000}\rangle \propto e^{-\alpha'^2/(2\tilde{\sigma}_{\alpha'}^2)} e^{-(\beta'-\pi/2)^2/(2\tilde{\sigma}_{\beta'}^2)} e^{-\gamma'^2/(2\tilde{\sigma}_{\gamma'}^2)}, \tag{6.54}$$

with $\tilde{\sigma}_{\alpha'} = \sqrt{\hbar/(I_a\omega_{\alpha'})} = 3.5 \times 10^{-3}$ rad, $\tilde{\sigma}_{\beta'} = \sqrt{\hbar/(I_b\omega_{\beta'})} = 3.4 \times 10^{-3}$ rad and $\tilde{\sigma}_{\gamma'} = \sqrt{\hbar/(I_a\omega_{\gamma'})} = 3.3 \times 10^{-2}$ rad.

Here, we see the advantage of the primed coordinate system especially introduced for the derivation of the initial state. In this system we can expand the potential harmonically and thus write down the initial state.

The particle in the state (6.54) aligns with the $\mathbf{e}'_1$-axis of the primed system. For convenience we now choose the unprimed space-fixed frame in a way that the initial state of the particle is aligned with the new $\mathbf{e}_3$-axis as it has been for the observation of rotational quantum revivals. It is then localized at $\beta = 0$ and I can later use approximations which require small $\beta \ll 1$. For expressing the initial state

(6.54) in the unprimed system we have to find the relation between the primed and unprimed Euler angles. We expand the body-fixed axes $\mathbf{n}_i'(\Omega') = \mathsf{R}(\alpha', \beta', \gamma')\mathbf{e}_i$ around the minimum of the potential energy yielding

$$\begin{aligned}\mathbf{n}_1'(\Omega') \approx &\mathbf{n}_1'(0, \pi/2, 0) + \alpha'\partial_{\alpha'}\mathbf{n}_1'(\Omega')_{|(0,\pi/2,0)} \\ &+ \beta'\partial_{\beta'}\mathbf{n}_1'(\Omega')_{|(0,\pi/2,0)} + \gamma'\partial_{\gamma'}\mathbf{n}_1'(\Omega')_{|(0,\pi/2,0)} \qquad (6.55a) \\ \approx &- \mathbf{e}_3 - (\beta' - \pi/2)\mathbf{e}_1 + \gamma'\mathbf{e}_2,\end{aligned}$$

$$\mathbf{n}_2'(\Omega') \approx \mathbf{e}_2 - \alpha'\mathbf{e}_1 + \gamma'\mathbf{e}_3. \qquad (6.55b)$$

$$\mathbf{n}_3'(\Omega') \approx \mathbf{e}_1 + \alpha'\mathbf{e}_2 - (\beta' - \pi/2)\mathbf{e}_3. \qquad (6.55c)$$

Analogously we obtain the expansion around $\beta = 0$ for the axes $\mathbf{n}_i(\Omega) = \mathsf{R}(\alpha, \beta, \gamma)$,

$$\mathbf{n}_1(\Omega) \approx -\beta\cos\gamma\mathbf{e}_1 + \sin(\alpha+\gamma)\mathbf{e}_2 - \cos(\alpha+\gamma)\mathbf{e}_3, \qquad (6.56a)$$

$$\mathbf{n}_2(\Omega) \approx \beta\sin\gamma\mathbf{e}_1 + \cos(\alpha+\gamma)\mathbf{e}_2 + \sin(\alpha+\gamma)\mathbf{e}_3, \qquad (6.56b)$$

$$\mathbf{n}_3(\Omega) \approx \mathbf{e}_1 + \beta\sin\alpha\mathbf{e}_2 - \beta\cos\alpha\mathbf{e}_3. \qquad (6.56c)$$

By equating $\mathbf{n}_i(\Omega) = \mathbf{n}_i'(\Omega')$ and using the expressions (6.55) and (6.56) one gets the following relation between primed and unprimed Euler angles

$$\alpha' = \beta\sin\alpha, \quad \beta' = \beta\cos\alpha + \frac{\pi}{2}, \quad \gamma' = \sin(\alpha+\gamma). \qquad (6.57)$$

With this we obtain the initial state in the Euler angle representation

$$\langle\alpha\beta\gamma|\tilde{\psi}_{000}\rangle \propto e^{-\beta^2\cos^2\alpha/(2\tilde{\sigma}_{\alpha'}^2)}e^{-\beta^2\sin^2\alpha/(2\tilde{\sigma}_{\beta'}^2)}e^{-\sin^2(\alpha+\gamma)^2/(2\tilde{\sigma}_{\gamma'}^2)} \qquad (6.58)$$

This state is localized around $\beta = 0$ and $(\gamma+\alpha) \ll 1$. However, we have seen before that we get the highest contrast of the interference signal for states with only $k = 0$ occupied. So after cooling the state into the ground state we switch the tweezer laser adiabatically from an ellipsoidally to a linearly polarized laser ($\psi \to 0$). For $\psi = 0$ the tweezer potential does not depend on the angle γ anymore and in the ground state of the new potential only $k = 0$ is occupied. The initial state after adiabatical changing is given by

$$\langle\alpha\beta\gamma|\psi_{000}\rangle \propto e^{-\beta^2\cos^2\alpha/(2\sigma_{\alpha'}^2)}e^{-\beta^2\sin^2\alpha/(2\sigma_{\beta'}^2)} \qquad (6.59)$$

with the new $\sigma_{\alpha'} = 3.24 \times 10^{-3}$ rad and $\sigma_{\beta'} = 3.22 \times 10^{-3}$ rad. Note that for $\sigma_{\alpha'} = \sigma_{\beta'}$ this state becomes α-independent and takes the form of the exemplary initial state (6.2) with $m = k = 0$.

The free time evolution operator of the symmetric rotor is diagonal in the angular momentum basis and we have already calculated the matrix elements of the phase operator in the angular momentum representation. For the numerical simulation of the interference signal the angular momentum basis is therefore the first choice. Thus, we have to expand the initial state (6.59) in the angular momentum representation of

$$\begin{aligned}\langle jmk|\psi_{000}\rangle =&\frac{1}{\sqrt{N}}\sqrt{\frac{2j+1}{8\pi^2}}\int_0^{2\pi}\mathrm{d}\alpha\int_0^{\pi}\mathrm{d}\beta\sin\beta\int_0^{2\pi}\mathrm{d}\gamma\; e^{-im\alpha}d^j_{mk}(\beta)e^{-ik\gamma}\\ &\times e^{-\beta^2\cos^2\alpha/(2\sigma^2_{\alpha'})}e^{-\beta^2\sin^2\alpha/(2\sigma^2_{\beta'})}.\end{aligned} \tag{6.60}$$

Here, I used Wigner d-matrices for the angular representation of the eigenstates of the symmetric rotor $\langle\alpha\beta\gamma|jmk\rangle = e^{im\alpha}d^j_{mk}(\beta)e^{ik\gamma}$. The γ-integration is carried out easily yielding the expected Kronecker δ_{k0}. In a next step, I approximate the small Wigner d-matrix $d^j_{mk}(\beta)$ for small $\beta \ll 1$ by using Bohr-Sommerfeld quantization action-angle variables (see Appendix B)

$$d^j_{mk}(\beta) \approx J_{m-k}\left[\beta\sqrt{\left(j+\frac{1}{2}\right)^2-\left(\frac{m+k}{2}\right)^2}\right]. \tag{6.61}$$

Further, our assumption that $k=0$ also implies $m=0$ because when the symmetry axis of the particle is tightly aligned with the space-fixed $\mathbf{e}_3$-axis, as is here the case, the body-fixed $\mathbf{n}_3$-axis is approximately identical to the $\mathbf{e}_3$-axis. This means that there cannot be any rotations around the space-fixed $\mathbf{e}_3$-axis when there are not any around the symmetry axis. Further we see that $\sigma_{\alpha'} \approx \sigma_{\beta'}$, which means that the initial state depends only weakly on α and is to first order not α-dependent. Also this results in $m=0$. So (6.60) simplifies to

$$\langle jmk|\psi_{000}\rangle =\frac{1}{\sqrt{N}}\sqrt{\frac{2j+1}{8\pi^2}}4\pi^2\delta_{m0}\delta_{k0}\int_0^{\infty}\mathrm{d}\beta\;\beta e^{-\beta^2/(2\sigma^2_{\alpha'})}J_0\left[\beta\left(j+\frac{1}{2}\right)\right]. \tag{6.62}$$

After carrying out the β-integration [85] I obtain

$$\langle jmk|\psi_{000}\rangle = \frac{1}{\sqrt{N}}\sqrt{\frac{2j+1}{8}}4\pi\sigma^2_{\alpha'}\delta_{m0}\delta_{k0}\exp\left[-\frac{\sigma^2_{\alpha'}(j+1/2)^2}{2}\right]. \tag{6.63}$$

With this angular momentum representation of the initial state we can discuss the time evolution of the rotor.

6.4.2. Imprinting the Phase

As mentioned before, I propose to use a linearly polarized laser pulse to imprint the phase. Since the induced relative phase

$$\varphi = \Delta\alpha |E_0|^2 \Delta t / 4\sqrt{2}\hbar \tag{6.64}$$

with $|E_0|^2 = 4P/(\pi w_0^2 \epsilon_0 c)$ depends on the pulse duration Δt and the laser power P. I propose to vary the relative phase by the choice of the laser power P and use a fixed pulse duration.

For imprinting the relative phase I propose to use a laser pulse with a duration of 100 ns, a wavelength of 1550 nm, and laser waist of 30 μm. Note that the suitable pulse duration is limited by the dispersion time scale of the initial state. The pulse duration has to be small in comparison to dispersion so that the orientation of the rotor can be assumed to be constant during the illumination. For the ground state discussed above the dispersion time $1/\kappa$ is of the order of microseconds and a pulse duration of 100 ns seems to be suitable.

6.4.3. Discussion of the Interference Signal

I now discuss the time evolution considering different scenarios. We start with the initial state (6.63) and use the time evolution operator for the symmetric rotor (2.25). Since there are only angular momentum eigenstates with $m = 0$ and $k = 0$ occupied and since the Hamiltonian is diagonal in k and m only the matrix elements $\langle j00|\phi|j'00\rangle$ of the phase operator are required

$$\langle j00|\phi|j'00\rangle = e^{-i\pi|j-j'|/4} e^{-i\varphi/\sqrt{2}} J_{\frac{|j-j'|}{2}}\left(\frac{\varphi}{\sqrt{2}}\right), \tag{6.65}$$

for $j - j'$ even and zero for $j - j'$ odd. which reduces the dimension of the matrices to $j_{\max} \times j_{max}$. The resulting interference signal is shown in Fig. 6.7(a) as a dash-dotted line. The initial state is so tightly aligned ($\langle \cos^2 \beta \rangle = 0.9998$) that the interference signal shows an optimal contrast.

Asymmetry of the Rotor

Now let us consider the asymmetry of the rotor in the way discussed in Sec. 6.3.1. That is only the energy eigenvalues of the symmetric rotor are replaced by the ones for the asymmetric rotor (6.30) while the eigenvectors remain unchanged. In Fig. 6.6 we see the effect of the asymmetry on the interference signal.

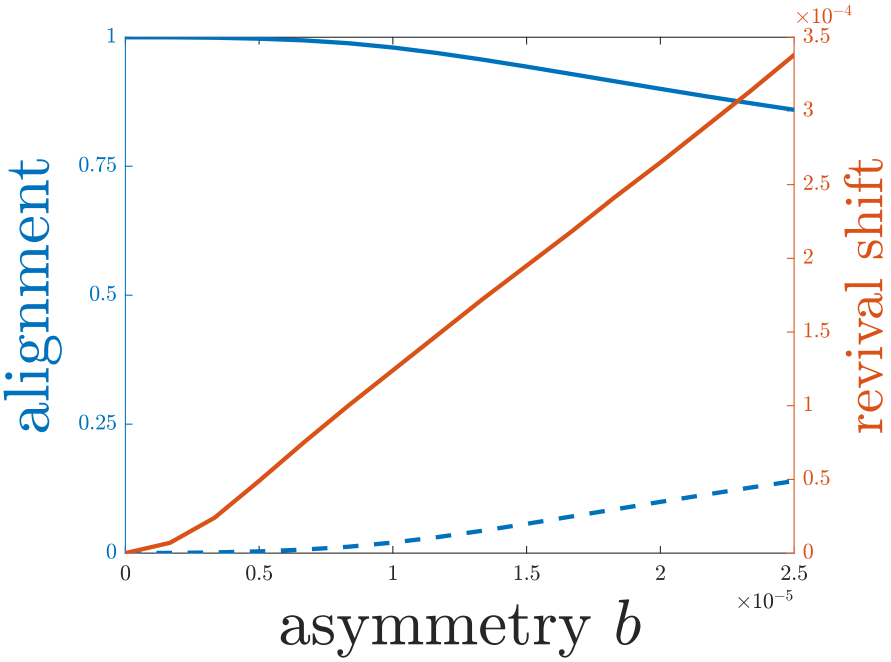

Figure 6.6.: Illustration of the effect of the asymmetry on the time evolution. In orange we see the relative shift of the revival time as a function of the asymmetry parameter b. The blue lines shows the alignment at $t = T_{\text{rev}}$ for a relative phase of $\varphi = 2\pi$ (upper line) and $\varphi = \pi$ (bottom line).

Firstly, we observe a slight shift of the revival time. And second, I illustrate the alignment $\langle\cos^2\beta\rangle$ in dependence of the asymmetry parameter b for the two cases $\varphi = 0$ and $\varphi = \pi$ at the shifted revival time. Note that we have to account for the shift of the revival time for choosing the time for inducing the phase. We see a decrease of the alignment even without an imprinted relative phase. Perfect quantum revivals can therefore only be expected for symmetric rotors. The asymmetry destroys the revivals. For a relative phase of $\varphi = \pi$ we expect an alignment close to zero at the revival time. Here, we observe an increase of the alignment. Thus, the contrast of the interference signal decreases with increasing asymmetry. For the silicon particle introduced in the beginning of this section the asymmetry parameter is $|b| = 2.3 \times 10^{-5}$ with a revival signal for $\varphi = 0$ of $\langle\cos^2\beta\rangle = 0.87$.

Decoherence

In the following, I will take environmental orientational decoherence into account. The dominant sources are thermal emission of photons, scattering of photons of the phase imprinting laser, and collisions with residual gas particles.

In section 4.2.1 I already discussed the emission of photons of silicon nanorods. We have seen that it can be neglected if the trapping laser and in this case also the phase laser has a wavelength of $\lambda = 1550$ nm.

The influence of the phase imprinting laser depends on the pulse duration and the laser power. I propose a duration of $\Delta t = 100$ ns for the pulse, a laser wavelength of $\lambda = 1550$ nm and a laser waist of $w = 30$ μm. With equation (6.64) we can estimate the required laser power to imprint phases up to $\varphi = 2\pi$ and obtain $P = 1.3$ mW. The rate of scattered photons at a particle of volume V as a function of the laser power is given by the Rayleigh scattering rate [30]

$$\Gamma_{\text{Rayleigh}} = \frac{P\chi_c^2 V^2 k^3}{3\pi^2 w_0 c\hbar}. \tag{6.66}$$

The number of photons scattered due to the pulse laser is given by the product of interaction time Δt and the scattering rate Γ_{Rayleigh} and for the highest considered laser power we obtain a number of 1.7×10^{-13} photons. This number is so small that we can neglect the interaction with the pulse laser as a source for environmental decoherence.

The scattering rate Γ_{gas} for collisions with residual gas particles can again be estimated by using (4.41) by replacing the surface of a cylinder by the surface of the ellipsoid. For a gas pressure of $p_{\text{g}} = 5 \times 10^{-9}$ mbar the scattering rate is $\Gamma_{\text{gas}} = 20.7$ Hz. The rate is related to the diffusion constant via $\Gamma_{\text{gas}} = 2D/\hbar$. With this we can run the protocol for Monte Carlo unraveling described in Sec. 6.3.2 with the resulting simulated interference signal represented in Fig. 6.7(a). As we have already seen for the observation of orientational quantum revivals, the collisions with residual gas particles results in a decreasing alignment at the revival time. This is also the main effect we observe for the interference signal. Further, it leads to a greater reduction of the alignment for $\varphi = 2\pi$ compared to the alignment at $\varphi = 0$ than observed without environmental decoherence. But this effect is negligible in comparison to the general reduction at $\varphi = 0$.

Imperfections of the Initial State

So far, we presumed an initial state of the rotor that shows no rotations around its body-fixed $\mathbf{n}_3$-axis, as expressed by the quantum numbers $k = m = 0$. To reach such an initial state one has to first cool the rotational motion of the nanoparticle into the ground state of a 3D orientation dependent potential, and then reduce the ellipticity of the tweezer laser adiabatically to a linear polarization, as described in section 6.4.1. Both are very strong experimental requirements and in the following I discuss the limits of the preparation of the initial state.

For a finite temperature there will always be a residual possibility to be in an excited state and not only in the ground state. The density operator is then given

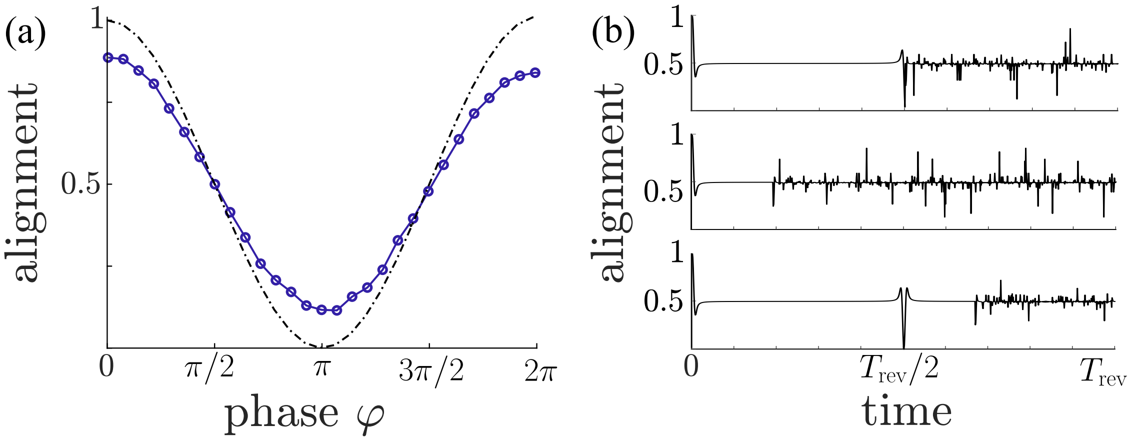

Figure 6.7.: Panel (a) shows the interference signal for the initial state (6.63) without considering environmental decoherence (dashed-dotted line) compared with the interference signal including environmental decoherence due to collisions with residual gas pressure with $p_g = 5 \times 10^{-9}$mbar (blue line). (b) Shows the alignment associated with three exemplary Monte-Carlo trajectories.

by

$$\rho = \frac{1}{Z} \sum_n e^{-E_n/(k_B T)} |\phi_n\rangle\langle\phi_n|. \tag{6.67}$$

For a sufficient small temperature we are still in the deep trapping regime and can still approximate the potential by the product of its harmonically expansions in α', β' and γ'. In addition to the ground state $|\phi_0\rangle = |\tilde{\psi}_{000}\rangle$ we consider the next excited states $|\phi_1\rangle = |\tilde{\psi}_{001}\rangle$,$|\phi_2\rangle = |\tilde{\psi}_{010}\rangle$ and $|\phi_3\rangle = |\tilde{\psi}_{100}\rangle$, which are the product states of ground states in two of the dimensions and the first excited state in the third dimension in the primed system $\{\alpha', \beta', \gamma'\}$. In the rotated system α, β, γ the states before the adiabatical changing read

$$\langle\alpha\beta\gamma|\phi_1\rangle = \sqrt{\frac{1}{N_1}} \sin(\alpha+\gamma)\langle\alpha\beta\gamma|\tilde{\psi}_{000}\rangle, \tag{6.68a}$$

$$\langle\alpha\beta\gamma|\phi_2\rangle = \sqrt{\frac{1}{N_2}} \beta\cos\alpha\langle\alpha\beta\gamma|\tilde{\psi}_{000}\rangle, \tag{6.68b}$$

$$\langle\alpha\beta\gamma|\phi_3\rangle = \sqrt{\frac{1}{N_3}} \beta\sin\alpha\langle\alpha\beta\gamma|\tilde{\psi}_{000}\rangle, \tag{6.68c}$$

with the eigenenergies

$$E_1 = \frac{\hbar}{2}(\omega_\alpha + \omega_\beta + \omega_\gamma) + \hbar\omega_\gamma \tag{6.69a}$$

$$E_2 = \frac{\hbar}{2}(\omega_\alpha + \omega_\beta + \omega_\gamma) + \hbar\omega_\beta \tag{6.69b}$$

$$E_3 = \frac{\hbar}{2}(\omega_\alpha + \omega_\beta + \omega_\gamma) + \hbar\omega_\alpha \tag{6.69c}$$

and the ground state $\langle\alpha\beta\gamma|\tilde{\psi}_{000}\rangle$ given by Eq. (6.58). After adiabatical changing the ellipticity to $\psi = 0$, which implies the ground state, and the factor $\langle\alpha\beta\gamma|\tilde{\psi}_{000}\rangle$ turns into the γ-independent state $\langle\alpha\beta\gamma|\psi_{000}\rangle$ given by (6.59). But the excited state in γ', $|\psi_{001}\rangle$, is γ-dependent and all three of the excited states depend on α even for $\sigma_{\alpha'} = \sigma_{\beta'}$. This implies that a finite number of angular momentum states with $k \neq 0$ and $m \neq 0$ will be occupied. The calculation of their representation in the angular momentum basis is similar to the one of the ground state, see Eq. (6.63). It results in

$$\langle jmk|\psi_{001}\rangle = -i\sqrt{\frac{2j+1}{2N_1}}\pi\sigma_{\alpha'}^2 e^{-\sigma_{\alpha'}^2\left[(j+1/2)^2-1\right]/2}(\delta_{m1}\delta_{k1} - \delta_{m-1}\delta_{k-1}), \tag{6.70a}$$

$$\langle jmk|\psi_{010}\rangle = \sqrt{\frac{2j+1}{2N_2}}\pi\sigma_{\alpha'}^4\sqrt{\left(j+\frac{1}{2}\right)^2 + \frac{m^2}{4}}e^{-\sigma_{\alpha'}^2\left[(j+1/2)^2-m^2/4\right]/2}\left(\delta_{m1} - \delta_{m-1}\right), \tag{6.70b}$$

$$\langle jmk|\psi_{100}\rangle = -i\sqrt{\frac{2j+1}{2N_3}}\pi\sigma_{\alpha'}^4\sqrt{\left(j+\frac{1}{2}\right)^2 + \frac{m^2}{4}}e^{-\sigma_{\alpha'}^2\left[(j+1/2)^2-m^2/4\right]/2}\left(\delta_{m1} + \delta_{m-1}\right). \tag{6.70c}$$

With this we can calculate the interference signal fora state with an exemplary temperature of 100 μK. At this temperature the occupation probability of the ground is around 80%. The interference signal for the corresponding density operator is shown in Fig. 6.8 along with this one of the ground state. We see that it is almost impossible to distinguish both signals. Thus, occupations of the first excited states do not affect the interference signal in a significant way.

But what happens when we cannot change the ellipticity of the tweezer laser adiabatically all the way to $\psi = 0$? Whether a process is adiabetic or not depends on the timescale τ on which the Hamiltonian changes. For an ideal adiabatic process we require $\tau \to \infty$ but in practice it depends on the energy separation of the initial state and the adjacent energy states. The timescale has to be large enough to prevent transitions to other energy states. Thus, to stay in the ground the condition $\tau > 2\pi\hbar/(E_0 - E_1)$ must be fulfilled. The smaller the energy gap between the states the larger must the timescale be.

Optimally, the state stays in the ground state with energy E_0. The state with the next larger eigenenergy is the state ψ_{001} and the energy gap between the two states is $E_0 - E_1 = \hbar\omega_{\gamma'}$. Equation (6.53) connects $\omega_{\gamma'}$ with the ellipticity ψ and we see that $\psi = 0$ implies $\omega_{\gamma'} = 0$. Thus, reaching a γ-independent potential adiabatically

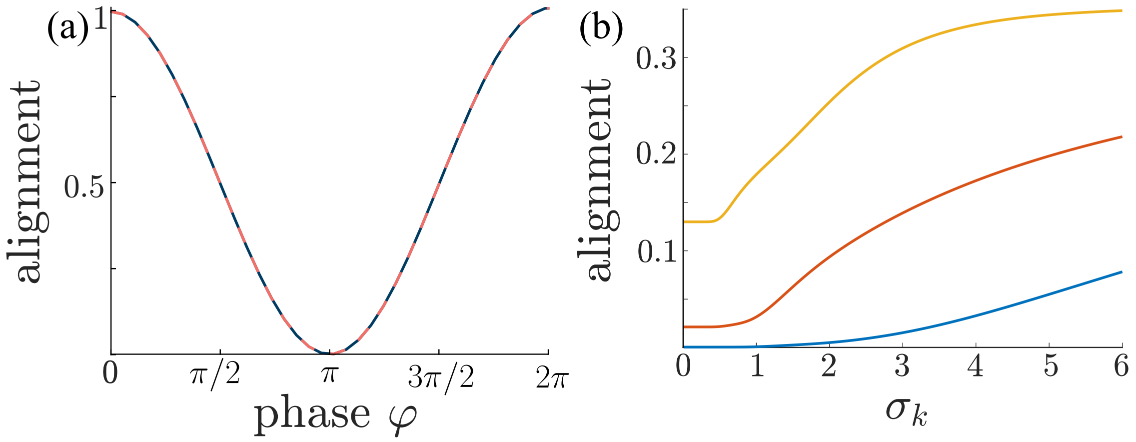

Figure 6.8.: Illustrated in panel (a) is the interference signal for the ground state (6.59) (blue solid line) as the initial state and for an initial density operator (6.67) for a temperature of $T = 100\ \mu$K (red dashed line). (b) shows the anti-alignment at $\varphi = \pi$ for three different angular spreads $\sigma_{\beta'} = 0.1$ (yellow), $\sigma_{\beta'} = 0.03$ (orange) and $\sigma_{\beta'} = 0.003$ (blue) as function of the width σ_k in k.

is in practice impossible. But where is the limit? It is not possible to carry out the switching arbitrarily slowly because the tweezer laser interacts with the particle which leads to recoil heating with the heating rate [33]

$$\xi_q^{\text{rec}} = \gamma_{\text{sc}}\epsilon^2\hbar/(2I_{\omega q})\Delta\chi_q^2\left(1-\sin^2\psi\delta_{q\beta}-\cos^2\psi\delta_{q\gamma}\right), \tag{6.71}$$

with $q \in \{\alpha,\beta,\gamma\}$ and the photon scattering rate $\gamma_{\text{sc}} = \omega k^3 V^2/6\pi V_{\text{c}}$. Here, ω is the tweezer frequency, k the wave number, V the volume of the particle and V_c the mode volume of the tweezer. Further, it depends on the susceptibility anisotropy $\Delta\chi_\alpha = |\chi_\beta - \chi_\gamma|$ ($\Delta\chi_\beta$ and $\Delta\chi_\gamma$ are given by cyclic permutations) and the laser power P_t via $\epsilon^2 = 2P_t k V_c/\pi\hbar\omega w_x w_y$. For further discussion of the initial state we have to keep this heating rate in mind.

Looking at the state (6.59) before switching off the ellipticity adiabatically we see that a finite value for $\sigma_{\gamma'}$ leads to a γ-dependent initial state, where angular momenta $k \neq 0$ are occupied and the state exhibits coherences in k. Since the coherences in k have only a negligible effect on the interference signal we assume a mixture in k with the probability for each k given by

$$p_k = \frac{1}{Z}e^{-k^2/\sigma_k^2}. \tag{6.72}$$

Figure 6.8 illustrates the alignment for $\varphi = \pi$ at $t = T_{\text{rev}}$ in dependence of σ_k for initial states with different angular spreads $\sigma_{\beta'}$. For $\sigma_k = 0$ the alignment for $\varphi = \pi$ is increasing with increasing angular spread $\sigma_{\beta'}$. This is expected because the initial alignment decreases with increasing $\sigma_{\beta'}$. The experimental set up with the parameters given in section 6.4.1, in particular with a tweezer laser power of $P_t = 0.1$ W, has a angular spread of $\sigma_{\beta'} \approx 0.003$. A lower laser power leads to larger angular spread and with this to a lower contrast of the interference signal on the one hand, but on the other hand it reduces the recoil heating.

With increasing σ_k the alignment at $t = T_{\text{rev}}$ for $\varphi = \pi$ increases. Especially for an angular spread of $\sigma_{\beta'} = 0.1$ the alignment rises even for small σ_k. For $\sigma_{\beta'} = 0.03$ values for σ_k up to $\sigma_k = 2$ promise a sufficiently high contrast of the interference signal. For $\sigma_{\beta'} = 0.003$ a spread in k with $\sigma_k = 2$ has almost no effect on the interference signal and for values of σ_k up to $\sigma_k = 6$ the contrast is still high enough.
We therefore know which σ_k have to be reached to control the alignment by inducing relative phases. To estimate how the recoil heating affects the initial state we need the timescale for the adiabatic process. The frequency $\omega_{\gamma'}$ is directly connected with $\sigma_k = \sqrt{I_c \omega_{\gamma'}/2\hbar}$. From $\sigma_k = 2$ it follows that $\tau \ll 3.4 \times 10^{-5}$s. For $\sigma_k = 5$ one obtains $\tau \ll 5.5 \times 10^{-6}$. For $\sigma_k = 2$ and $P_t = 0.1$ which leads to $\sigma_{\beta'} = 0.003$ the heating rate is $\xi = 603.8$ Hz. For an angular spread of $\sigma_{\beta'} = 0.03$ one needs a laser power of only $P_t = 10^{-5}$ W and with this the heating rate reduces to $\xi = 6.1 \times 10^{-2}$ Hz. During the time of the adiabatic process the recoil heating has no significant influence on the initial state and does not lead to excitement of the state to higher k.

To summarize, the ground state with only $k = m = 0$ as I introduced in section 6.4.1 as the initial state is still idealistic and in practice not feasible. But the occupation of the first excited states has no noticeable effect on the interference signal and even with finite values of k with a spread of $\sigma_k = 2$ the interferometric control of a nanorotor's alignment is possible.

Further, I discussed the asymmetry of the nanorparticle and environmental decoherence. Both lead to a decrease of visibility but within an acceptable range. Thus, the experimental observation of the here shown interference signal should be feasible with state-of-the-art techniques.

7. Conclusion and Outlook

In the focus of my thesis were novel superposition tests with massive aspherical nanoparticles exploiting the non-linearity of the rotational dynamics. Further, I used and developed semiclassical methods for the description of rotational quantum mechanics whith thousands angular momentum quanta involved.

In the first part, I presented an experimental interference scheme for probing rotational quantum revivals with aspherical and anisotropic nanoparticles. This scheme contains four important steps. In the first step, the initial state is prepared by trapping and levitating the particle in an optical tweezer and cooling the orientional degrees of freedom by cavity or feedback cooling. In the second phase of the experiment the tweezer laser is turned off, the particle drops and the orientational degrees of freedom evolve freely. At the revival time $T_{\rm rev} = 2\pi I/\hbar$ or an integer multiple thereof the alignment of the nanorotor is measured by recording the light scattered due to a running laser wave. The revival time is very sensitive to the length of the object. Thus, in the last step the particle is recycled by trapping it again in a standing linearly polarized laser wave and moving it to the original position.

I discussed and demonstrated the feasibility of this experimental scheme at the example of double-walled carbon nanotubes with a length of 50 nm and a mass of 1.9×10^5 amu and silicon nanorods with a length of 50 nm as mass of 1.4×10^6 amu. Numerical calculations of the rotational dynamics show that this interference scheme is realizable with state-of-the-art and upcoming techniques of levitated optomechanics. The quantum revivals are observable for temperatures of the orientational motion of below 1 K and in the presence of environmental decoherence due to collisions with residual gas particles at a realistic gas pressure of 5×10^{-9} mbar (5×10^{-10} mbar for silicon nanorods). This experimental scheme represents a macroscopic test of the superposition principle and the quantization of angular momenta. Further, it can test objective collapse models, like for example continuous spontaneous localization [12], which predicts the loss of orientational coherences [89, 90].

Especially for initial states for temperatures beyond 1 mK the numerical diagonalization of the Hamiltonian becomes intractable due to the high number of occupied angular momentum states. However, this problem is solved by a semiclassical approximation of the initial state matrix elements in the angular momentum eigenbasis which allows the free rotational dynamics to be calculated exactly.

The revival signal is very sensitive to static external torques and so this set up opens the door for quantum enhanced ultra-sensitive torque sensing. In the here presented set up external torques on the order of 10^{-30} Nm are observable, which is many magnitudes smaller than in state-of-the art set ups [28, 82].

For discussing the effect of an external torque on the revival signal it is necessary to not only approximate the initial state semiclassically but also the time evolution operator. Here, I used the semiclassical WKB method for planar rotations and the EBK method for linear rotations for an approximation of the rotational time evolution which preserve the revival structure. While for planar rotations the WKB method is expedient, for linear rotations a perturbative method seems to be the suitable solution.

In the last part of this thesis, I presented a Mach-Zender type interferometric scheme for the steering of a nanorotor alignment based on applying a pulsed optical dipole potential during the free time evolution. This scheme is based on rotational quantum revivals and the emergence of superpositions of well-localized orientational wave packets at fractional revival times. The effect is described in an effective eight-dimensional subspace, which is derived by a semiclassical approximation of the free rotational time evolution operator. I discussed deviations of an ideal perfectly aligned linear rigid rotor and their effect on the interference signal. The interference effect is observable even for realistic initial states of a slightly asymmetric particle interacting with its environment.

This interferometric scheme can not only be used for testing orientational superpositions but also to control the field-free alignment of single nanoscale particles. The scheme can be extended by applying several laser pulses at different integer multiples of $T_{\text{rev}}/8$ at smaller fractions of the revival time. It can be used for the preparation of specific orientational superpositions. The control of the alignment enables tests of quantum physics, orientation resolved spectroscopy, and rotation state-resolved collision studies [91, 92] and it may even be applied for processing quantum information [93, 94].

This suggests that there are a lot of interesting applications of rotational quantum dynamics which are challenging on the experimental and the theoretical side.

A. WKB-Approximation of the Time Evolution Operator

We start with the Hamiltonian of a linear rigid rotor and assume additionally $p_\alpha = 0$

$$\begin{aligned}\mathsf{H} =& \frac{\mathsf{p}_\beta^2}{2I} - \frac{\hbar^2}{8I}\left(1 + \frac{1}{\sin^2\beta}\right)\\ =& -\frac{\hbar^2}{2I}\frac{1}{\sin\beta}\partial_\beta(\sin\beta\partial_\beta),\end{aligned} \tag{A.1}$$

where I use the angle representation (2.17) of the canonical momentum operator p_β, and the second term in the first line is the quantum potential. To find the eigenstates $|\phi\rangle$ of the stationary Schrödinger equation

$$\mathsf{H}|\phi = E|\phi\rangle \tag{A.2}$$

we make the ansatz [62]

$$\phi(\alpha) = e^{iS(\beta)/\hbar}, \tag{A.3}$$

and expand $S(\beta)$ in orders of $\hbar$, $S(\beta) = S_0(\beta) + \hbar S_1(\beta)/i + \mathcal{O}(\hbar^2)$. Inserting (A.3) into (A.2) and sorting in orders of $\hbar$ leads to

$$\frac{1}{2I}\left(\partial_\beta S_0(\beta)\right)^2 = E \tag{A.4a}$$

$$-\frac{i\hbar}{2I}\left[\partial_\beta^2 S_0(\beta) + 2[\partial_\beta S_0(\beta))(\partial_\beta S_1(\beta)] - \cot\beta\partial_\beta S_0(\beta)\right] = 0. \tag{A.4b}$$

With the classical canonical momentum $p_\beta(\beta) = \pm\sqrt{2IE}$ we obtain from (A.4) expressions for $S_0(\beta)$ and $S_1(\beta)$

$$S_0(\beta) = \int_0^\beta \mathrm{d}\beta'\ p_\beta(\beta') = \sqrt{2IE}\beta \tag{A.5a}$$

$$S_1(\beta) = -\frac{1}{2}\ln(p_\beta(\beta)) - \frac{1}{2}\ln(|\sin\beta|) + c. \tag{A.5b}$$

Inserting (A.5a) in (A.3) and using the Bohr- Sommerfeld quantization for the energy $E = \hbar^2(j+1/2)/(2I)$ we obtain

$$\begin{aligned}\phi_{\mathrm{WKB}}(\beta) =& \frac{c_1}{\sqrt{\hbar(j+1/2)\sin\beta}} \exp\left[\frac{i}{\hbar}\left(\hbar(j+1/2)\beta + \tilde{c}_1\right)\right] \\ &+ \frac{c_2}{\sqrt{\hbar(j+1/2)\sin\beta}} \exp\left[-\frac{i}{\hbar}\left(\hbar(j+1/2)\beta + \tilde{c}_2\right)\right].\end{aligned} \tag{A.6}$$

To determine the integration constants we compare the WKB eigenstates with the exakt eigenstates of the free Hamiltonian with $m = 0$

$$\langle\alpha\beta|j0\rangle = \sqrt{(2j+1)/(4\pi)}P_j(\cos\beta). \tag{A.7}$$

These exact eigenfunctions are real and so we set $c_1 = c_2$ and $\tilde{c}_1 = \tilde{c}_2$. Further we look at the exact eigenfunction for $\beta = \pi/2$ because we expect the semiclassical eigenfunction matches here best with the exact ones. The Legendre polynomials are zero at $\beta = \pi/2$ for all odd j. For even values of j the eigenfunction at $\beta = \pi/2$ switches between a local maximum for $j = 4n$ with $n \in \mathbb{N}_0$ and a local minimum for $j = 2(2n+1)$ with $n \in \mathbb{N}_0$. To obtain the same behaviour for the WKB eigenfunctions we have to choose $\tilde{c}_1 = \pi/4$. The last remaining constant c_1 is now determined by the normalization of the eigenfuncion. With this we get the result for the WKB eigenfunctions

$$\phi_{\mathrm{WKB}}(\beta) = \frac{2}{\sqrt{2\pi\sin\beta}} \cos\left[\left(j+\frac{1}{2}\right)\beta - \frac{\pi}{4}\right] \tag{A.8}$$

and with this the semiclassical propagator reads

$$\langle\beta|\mathsf{U}(t)|\beta_0\rangle = \frac{1}{\sqrt{\sin\beta\sin\beta_0}}\left[u_c(\beta-\beta_0;t) + u_s(\beta+\beta_0;t)\right] \tag{A.9}$$

with

$$\begin{aligned}u_c(\Delta\beta;t) &= \frac{1}{\pi}\sum_{j\in\mathbb{N}_0} e^{-ij(j+1)\pi t/T_{\mathrm{rev}}} \cos\left[\left(j+\frac{1}{2}\right)\Delta\beta\right] \\ &= \frac{e^{i\Delta\beta/2}}{2\pi}\sum_{k\in\mathbb{Z}} e^{-i\pi k(k+1)\pi t/T_{\mathrm{rev}}} e^{ik\Delta\beta}\end{aligned} \tag{A.10a}$$

$$u_s(\bar{\beta};t) = \frac{1}{\pi}\sum_{j\in\mathbb{N}_0} e^{-ij(j+1)\pi t/T_{\mathrm{rev}}} \sin\left[\left(j+\frac{1}{2}\right)2\bar{\beta}\right] \tag{A.10b}$$

with $\Delta\beta = \beta - \beta_0$ and $\bar{\beta} = (\beta+\beta_0)/2$. Note that one gets the same result by asymptotic expansion of the Legendre polynomials $P_j(\cdot)$ for large j [72].

B. Semiclassical Approximation of Wigner d-matrix

The Wigner d-matrices $d^k_{jm}(\beta)$ are defined by the matrix elements of the rotation operator describing a rotation around the $\mathbf{e}_2$-axis

$$d^j_{mk}(\beta) = \langle jm|e^{-i\beta \mathrm{J}_2}|jk\rangle \tag{B.1}$$

In the limit of $\beta \ll 1$ and $j \ll 1$ we can use Bohr-Sommerfeld approximation method [62] for the semiclassical calculation of the matrix elements. For that we express the space-fixed $\mathbf{J}_2$-component in terms of action-angle variables [62]

$$J_2 = \sqrt{J^2 - M^2}\sin\alpha_M, \tag{B.2}$$

and use the quantization rules $M = \hbar m$ and $J^2 = \hbar^2(j+1/2)^2$. Inserting this into (2.72) for the calculation of semiclassical matrix elements yields

$$\langle jm|e^{-i\beta \mathrm{J}_2}|jk\rangle = \frac{1}{2\pi}\int_0^{2\pi} \mathrm{d}\alpha_m\ e^{i(m-k)\alpha_m} e^{-i\beta\sqrt{(j+1/2)^2-(m+k)^2/4}\sin\alpha_m}. \tag{B.3}$$

By carrying out the α_m-integration we obtain the resulting semiclasscial expression for the Wigner d-matrices

$$d^j_{mk}(\beta) = J_{m-k}\left[\sqrt{\left(j+\frac{1}{2}\right)^2 - \left(\frac{m+k}{2}\right)^2}\beta\right]. \tag{B.4}$$

Danksagung

Ich möchte mich an dieser Stelle bei all denjenigen bedanken, die mich in den letzten Jahren im Rahmen meiner Doktorarbeit unterstützt haben.

Zunächst danke ich Klaus Hornberger für die Möglichkeit an diesem interessanten Thema zu arbeiten, für die ausführlichen Diskussionen und die kompetente und geduldige Betreuung. Mein Dank gilt auch Benjamin, der durch fachliche Unterstützung, neuen Anregungen und konstruktiver Kritik zum Gelingen dieses Projektes beigetragen hat. Bei der gesamten Arbeitsgruppe, bei Björn, Filip, Henning, Jonas, Lukas und Marduk bedanke ich mich für das angenehme Klima in der Arbeitsgruppe, für gemeinsame Grillabende, das Feierabendbier, die Weihnachtsfeiern und den Spaß,den wir gemeinsam während und nach der Arbeit hatten.
Auch meinen Komilitonen während des Bachelor- und Masterstudiums möchte ich für die unvergessliche Zeit danken. Ganz besonders möchte ich mich bei meinen Eltern und Brüdern für Ihre Unterstützung in allen Lebensphasen und insbesondere während meines Studiums und der Dissertation bedanken. Meinem Mann Björn danke ich für seine Geduld in den letzten Wochen vor Abgabe, seine Unterstützung und die vielen Aufmunterungen.

Bibliography

[1] C. Davisson and L. H. Germer, *Diffraction of Electrons by a Crystal of Nickel*, Phys. Rev. **30**, 705–740 (1927).

[2] G. P. Thomson, *Experiments on the Diffraction of Cathode Rays*, Proc. R. Soc London A **117**, 600 (1928).

[3] H. v. J. Halban and P. Preiswerk, *Preuve experimentale de la diffraction de neutrons*, C. R. Acad. Sci. **203** (1936).

[4] O. Carnal and J. Mlynek, *Young's double-slit experiment with atoms: A simple atom interferometer*, Phys. Rev. Lett. **66**, 2689–2692 (1991).

[5] D. W. Keith, C. R. Ekstrom, Q. A. Turchette, and D. E. Pritchard, *An interferometer for atoms*, Phys. Rev. Lett. **66**, 2693–2696 (1991).

[6] E. M. Rasel, M. K. Oberthaler, H. Batelaan, J. Schmiedmayer, and A. Zeilinger, *Atom Wave Interferometry with Diffraction Gratings of Light*, Phys. Rev. Lett. **75**, 2633–2637 (1995).

[7] M. Arndt, O. Nairz, J. Vos-Andreae, C. Keller, G. van der Zouw, and A. Zeilinger, *Wave-particle duality of C_{60} molecules*, Nature **401**, 680–682 (1999).

[8] B. Brezger, L. Hackermüller, S. Uttenthaler, J. Petschinka, M. Arndt, and A. Zeilinger, *Matter-Wave Interferometer for Large Molecules*, Phys. Rev. Lett. **88**, 100404 (2002).

[9] S. Eibenberger, S. Gerlich, M. Arndt, M. Mayor, and J. Tüxen, *Matter–wave interference of particles selected from a molecular library with masses exceeding 10000 amu*, Phys. Chem. Chem. Phys. **15**, 14696–14700 (2013).

[10] Y. Y. Fein, P. Geyer, P. Zwick, F. Kiałka, S. Pedalino, M. Mayor, S. Gerlich, and M. Arndt, *Quantum superposition of molecules beyond 25 kDa*, Nature Physics **15**, 1242–1245 (2019).

[11] M. Arndt and K. Hornberger, *Testing the limits of quantum mechanical superpositions*, Nature Physics **10**, 271–277 (2014).

[12] A. Bassi, K. Lochan, S. Satin, T. P. Singh, and H. Ulbricht, *Models of wave-function collapse, underlying theories, and experimental tests*, Rev. Mod. Phys. **85**, 471–527 (2013).

[13] O. Romero-Isart, A. C. Pflanzer, F. Blaser, R. Kaltenbaek, N. Kiesel, M. Aspelmeyer, and J. I. Cirac, *Large Quantum Superpositions and Interference of Massive Nanometer-Sized Objects*, Phys. Rev. Lett. **107**, 020405 (2011).

[14] J. Bateman, S. Nimmrichter, K. Hornberger, and H. Ulbricht, *Near-field interferometry of a free-falling nanoparticle from a point-like source*, Nature Communications **5**, 4788 (2014).

[15] T. Li, S. Kheifets, and M. G. Raizen, *Millikelvin cooling of an optically trapped microsphere in vacuum*, Nature Physics **7**, 527–530 (2011).

[16] P. F. Barker and M. N. Shneider, *Cavity cooling of an optically trapped nanoparticle*, Phys. Rev. A **81**, 023826 (2010).

[17] T. Seideman, *Revival Structure of Aligned Rotational Wave Packets*, Phys. Rev. Lett. **83**, 4971–4974 (1999).

[18] Y. Ma, K. E. Khosla, B. A. Stickler, and M. S. Kim, *Quantum Persistent Tennis Racket Dynamics of Nanorotors*, Phys. Rev. Lett. **125**, 053604 (2020).

[19] A. Einstein, *Experimental Proof of the Existence of Ampère's Molecular Currents*, in Proc. KNAW **18**, 696 (1915).

[20] S. J. Barnett, *Magnetization by Rotation*, Phys. Rev. **6**, 239–270 (1915).

[21] P. W. Dooley, I. V. Litvinyuk, K. F. Lee, D. M. Rayner, M. Spanner, D. M. Villeneuve, and P. B. Corkum, *Direct imaging of rotational wave-packet dynamics of diatomic molecules*, Phys. Rev. A **68**, 023406 (2003).

[22] M. D. Poulsen, E. Péronne, H. Stapelfeldt, C. Z. Bisgaard, S. S. Viftrup, E. Hamilton, and T. Seideman, *Nonadiabatic alignment of asymmetric top molecules:âRotational revivals*, The Journal of Chemical Physics **121**, 783–791 (2004).

[23] V. Kumarappan, S. S. Viftrup, L. Holmegaard, C. Z. Bisgaard, and H. Stapelfeldt, *Aligning molecules with long or short laser pulses*, Physica Scripta **76**, C63–C68 (2007).

[24] B. Shepperson, A. A. Søndergaard, L. Christiansen, J. Kaczmarczyk, R. E. Zillich, M. Lemeshko, and H. Stapelfeldt, *Laser-Induced Rotation of Iodine Molecules in Helium Nanodroplets: Revivals and Breaking Free*, Phys. Rev. Lett. **118**, 203203 (2017).

[25] S. Kuhn, P. Asenbaum, A. Kosloff, M. Sclafani, B. A. Stickler, S. Nimmrichter, K. Hornberger, O. Cheshnovsky, F. Patolsky, and M. Arndt, *Cavity-Assisted Manipulation of Freely Rotating Silicon Nanorods in High Vacuum*, Nano Lett. **15**, 5604–5608 (2015).

[26] T. M. Hoang, Y. Ma, J. Ahn, J. Bang, F. Robicheaux, Z.-Q. Yin, and T. Li, *Torsional Optomechanics of a Levitated Nonspherical Nanoparticle*, Phys. Rev. Lett. **117**, 123604 (2016).

[27] S. Kuhn, A. Kosloff, B. A. Stickler, F. Patolsky, K. Hornberger, M. Arndt, and J. Millen, *Full rotational control of levitated silicon nanorods*, Optica **4**, 356–360 (2017).

[28] S. Kuhn, B. A. Stickler, A. Kosloff, F. Patolsky, K. Hornberger, M. Arndt, and J. Millen, *Optically driven ultra-stable nanomechanical rotor*, Nature Communications **8**, 1670 (2017).

[29] M. Rashid, M. Toroš, A. Setter, and H. Ulbricht, *Precession Motion in Levitated Optomechanics*, Phys. Rev. Lett. **121**, 253601 (2018).

[30] B. A. Stickler, S. Nimmrichter, L. Martinetz, S. Kuhn, M. Arndt, and K. Hornberger, *Rotranslational cavity cooling of dielectric rods and disks*, Phys. Rev. A **94**, 033818 (2016).

[31] C. Zhong and F. Robicheaux, *Shot-noise-dominant regime for ellipsoidal nanoparticles in a linearly polarized beam*, Phys. Rev. A **95**, 053421 (2017).

[32] H. Rudolph, J. Schäfer, B. A. Stickler, and K. Hornberger, *Theory of nanoparticle cooling by elliptic coherent scattering*, Phys. Rev. A **103**, 043514 (2021).

[33] J. Schäfer, H. Rudolph, K. Hornberger, and B. A. Stickler, *Cooling Nanorotors by Elliptic Coherent Scattering*, Phys. Rev. Lett. **126**, 163603 (2021).

[34] T. Delord, P. Huillery, L. Nicolas, and G. Hétet, *Spin-cooling of the motion of a trapped diamond*, Nature **580**, 56–59 (2020).

[35] J. Bang, T. Seberson, P. Ju, J. Ahn, Z. Xu, X. Gao, F. Robicheaux, and T. Li, *Five-dimensional cooling and nonlinear dynamics of an optically levitated nanodumbbell*, Phys. Rev. Research **2**, 043054 (2020).

[36] F. van der Laan, F. Tebbenjohanns, R. Reimann, J. Vijayan, L. Novotny, and M. Frimmer, *Sub-Kelvin Feedback Cooling and Heating Dynamics of an Optically Levitated Librator*, Phys. Rev. Lett. **127**, 123605 (2021).

[37] U. Delić, M. Reisenbauer, K. Dare, D. Grass, V. Vuletić, N. Kiesel, and M. Aspelmeyer, *Cooling of a levitated nanoparticle to the motional quantum ground state*, Science **367**, 892–895 (2020).

[38] L. Magrini, P. Rosenzweig, C. Bach, A. Deutschmann-Olek, S. G. Hofer, S. Hong, N. Kiesel, A. Kugi, and M. Aspelmeyer, *Real-time optimal quantum control of mechanical motion at room temperature*, Nature **595**, 373–377 (2021).

[39] F. Tebbenjohanns, M. L. Mattana, M. Rossi, M. Frimmer, and L. Novotny, *Quantum control of a nanoparticle optically levitated in cryogenic free space*, Nature **595**, 378–382 (2021).

[40] L. Martinetz, K. Hornberger, and B. A. Stickler, *Gas-induced friction and diffusion of rigid rotors*, Phys. Rev. E **97**, 052112 (2018).

[41] C. Zhong and F. Robicheaux, *Decoherence of rotational degrees of freedom*, Phys. Rev. A **94**, 052109 (2016).

[42] B. A. Stickler, B. Papendell, and K. Hornberger, *Spatio-orientational decoherence of nanoparticles*, Phys. Rev. A **94**, 033828 (2016).

[43] B. Papendell, B. A. Stickler, and K. Hornberger, *Quantum angular momentum diffusion of rigid bodies*, New Journal of Physics **19**, 122001 (2017).

[44] B. A. Stickler, B. Schrinski, and K. Hornberger, *Rotational Friction and Diffusion of Quantum Rotors*, Phys. Rev. Lett. **121**, 040401 (2018).

[45] B. A. Stickler, B. Papendell, S. Kuhn, B. Schrinski, J. Millen, M. Arndt, and K. Hornberger, *Probing macroscopic quantum superpositions with nanorotors*, New J. Phys. **20**, 122001 (2018).

[46] F. Kiałka, B. A. Stickler, and K. Hornberger, *Orbital angular momentum interference of trapped matter waves*, Phys. Rev. Research **2**, 022030 (2020).

[47] M. Spanner, E. A. Shapiro, and M. Ivanov, *Coherent Control of Rotational Wave-Packet Dynamics via Fractional Revivals*, Phys. Rev. Lett. **92**, 093001 (2004).

[48] F. Scheck, *Theoretische Physik 1: Mechanik*, Springer-Lehrbuch, Springer Berlin Heidelberg, 2007.

[49] H. Goldstein, C. Poole, and J. Safko, *Classical Mechanics*, Pearson, 2013.

[50] T. Fischer, *Decoherence of the Orientation State*, Dr. Hut Verlag, 2015.

[51] J. Sakurai and J. Napolitano, *Modern Quantum Mechanics*, Addison-Wesley, 2011.

[52] L. Biedenharn, J. Louck, and P. Carruthers, *Angular Momentum in Quantum Physics: Theory and Application*, Encyclopedia of Mathematics and its Applications, Cambridge University Press, 2009.

[53] B. S. DeWitt, *Point Transformations in Quantum Mechanics*, Phys. Rev. **85**, 653–661 (1952).

[54] B. S. DeWitt, *Dynamical Theory in Curved Spaces. I. A Review of the Classical and Quantum Action Principles*, Rev. Mod. Phys. **29**, 377–397 (1957).

[55] L. Landau and E. Lifshitz, *Quantum Mechanics: Non-Relativistic Theory*, Course of theoretical physics, Elsevier Science, 1991.

[56] E. Wigner, *On the Quantum Correction For Thermodynamic Equilibrium*, Phys. Rev. **40**, 749–759 (1932).

[57] J. E. Moyal, *Quantum mechanics as a statistical theory*, Mathematical Proceedings of the Cambridge Philosophical Society **45**, 99â124 (1949).

[58] T. Fischer, C. Gneiting, and K. Hornberger, *Wigner function for the orientation state*, New J. Phys. **15**, 063004 (2013).

[59] C. Gneiting, T. Fischer, and K. Hornberger, *Quantum phase-space representation for curved configuration spaces*, Phys. Rev. A **88**, 062117 (2013).

[60] J. P. Bizarro, *Weyl-Wigner formalism for rotation-angle and angular-momentum variables in quantum mechanics*, Phys. Rev. A **49**, 3255–3276 (1994).

[61] B. Schrinski, Y. J. Chan, and B. Schrinski, *Thermalization of the Quantum Planar Rotor with external potential*, ArXiv preprint arXiv:.2207.04810 (2022.

[62] M. Child, *Semiclassical Mechanics with Molecular Applications*, Oxford University Press, 2014.

[63] M. Brack and R. Bhaduri, *Semiclassical Physics*, Frontiers in physics, Avalon Publishing, 1997.

[64] H. Breuer and F. Petruccione, *The theory of open quantum systems*, Oxford Univ. Press, Oxford, 2003.

[65] K. Hornberger, *Introduction to Decoherence Theory*, in *Entanglement and Decoherence: Foundations and Modern Trends*, Springer Berlin Heidelberg, 2009.

[66] B. Papendell, *Masterarbeit: Dekohärenz von Orientierungsfreiheitsgraden*, 2014.

[67] K. Hornberger, S. Uttenthaler, B. Brezger, L. Hackermüller, M. Arndt, and A. Zeilinger, *Collisional Decoherence Observed in Matter Wave Interferometry*, Phys. Rev. Lett. **90**, 160401 (2003).

[68] K. Hornberger and B. Vacchini, *Monitoring derivation of the quantum linear Boltzmann equation*, Phys. Rev. A **77**, 022112 (2008).

[69] B. Vacchini and K. Hornberger, *Relaxation dynamics of a quantum Brownian particle in an idealgas*, Eur. Phys. J. Spec. Top. **151**, 50 (2007).

[70] B. Vacchini and K. Hornberger, *Quantum linear Boltzmann equation*, Phys. Rep. **478**, 71–120 (2009).

[71] J. R. Taylor, *Scattering Theory: The Quantum Theory of Nonrelativistic Collisions*, Dover Publications, 2000.

[72] F. W. J. Olver, , D. W. Lozier, R. F. Boisvert, and C. W. Clark, *The NIST Handbook of Mathematical Functions*, Cambridge Univ. Press, 2010.

[73] A. C. Pflanzer, O. Romero-Isart, and J. I. Cirac, *Master-equation approach to optomechanics with arbitrary dielectrics*, Phys. Rev. A **86**, 013802 (2012).

[74] H. Pino, J. Prat-Camps, K. Sinha, B. P. Venkatesh, and O. Romero-Isart, *On-chip quantum interference of a superconducting microsphere*, Quantum Science and Technology **3**, 025001 (2018).

[75] L. Hackermüller, K. Hornberger, B. Brezger, A. Zeilinger, and M. Arndt, *Decoherence of matter waves by thermal emission of radiation*, Nature **427**, 711–714 (2004).

[76] J. D. Jackson, *Classical electrodynamics*, Wiley, 1975.

[77] B. Kozinsky and N. Marzari, *Static Dielectric Properties of Carbon Nanotubes from First Principles*, Phys. Rev. Lett. **96**, 166801 (2006).

[78] K. Liu, J. Deslippe, F. Xiao, R. B. Capaz, X. Hong, S. Aloni, A. Zettl, W. Wang, X. Bai, S. G. Louie, E. Wang, and F. Wang, *An atlas of carbon nanotube optical transitions*, Nature Nanotechnology **7**, 325–329 (2012).

[79] U. J. Kim, X. M. Liu, C. A. Furtado, G. Chen, R. Saito, J. Jiang, M. S. Dresselhaus, and P. C. Eklund, *Infrared-Active Vibrational Modes of Single-Walled Carbon Nanotubes*, Phys. Rev. Lett. **95**, 157402 (2005).

[80] M. Basler, P. Tipler, R. Dohmen, G. Mosca, C. Heinisch, A. Schleitzer, M. Zillgitt, J. Wagner, and C. Kommer, *Physik: für Wissenschaftler und Ingenieure*, Springer Berlin Heidelberg, 2014.

[81] D. Griffiths, *Quantenmechanik: Eine Einführung*, Pearson Deutschland GmbH, 2012.

[82] M. Wu, N. L.-Y. Wu, T. Firdous, F. Fani Sani, J. E. Losby, M. R. Freeman, and P. E. Barclay, *Nanocavity optomechanical torque magnetometry and radiofrequency susceptometry*, Nature Nanotechnology **12**, 127–131 (2017).

[83] B. Schrinski, B. A. Stickler, and K. Hornberger, *Interferometric control of nanorotor alignment*, Phys. Rev. A **1**05, L021502 (2022).

[84] R. G. Littlejohn and L. Yu, *Uniform Semiclassical Approximation for the Wigner 6j-Symbol in Terms of Rotation Matrices*, The Journal of Physical Chemistry A **113**, 14904–14922 (2009).

[85] D. Zwillinger and A. Jeffrey, *Table of Integrals, Series, and Products*, Elsevier Science, 2007.

[86] H. Davis and J. E. Beam, *Perturbation formulas for the energy levels of the slightly asymmetric top*, Journal of Molecular Spectroscopy **6**, 312–318 (1961).

[87] L. Devroye, *Nonuniform random variate generation*, Handbooks in operations research and management science **13**, 83–121 (2006).

[88] A. Pontin, H. Fu, M. Toroš, T. S. Monteiro, and P. F. Barker, *Simultaneous cooling of all six degrees of freedom of an optically levitated nanoparticle by elliptic coherent scattering*, ArXiv preprint arXiv:.2205.10193 (2022).

[89] B. Schrinski, B. A. Stickler, and K. Hornberger, *Collapse-induced orientational localization of rigid rotors*, J. Opt. Soc. Am. B **34**, C1–C7 (2017).

[90] M. Carlesso, M. Paternostro, H. Ulbricht, A. Vinante, and A. Bassi, *Non-interferometric test of the continuous spontaneous localization model based on rotational optomechanics*, New J. of Phys. **20**, 083022 (2018).

[91] C. P. Koch, M. Lemeshko, and D. Sugny, *Quantum control of molecular rotation*, Rev. Mod. Phys. **91**, 035005 (2019).

[92] B. A. Stickler, K. Hornberger, and M. S. Kim, *Quantum rotations of nanoparticles*, Nature Reviews Physics **3**, 589–597 (2021).

[93] V. V. Albert, J. P. Covey, and J. Preskill, *Robust Encoding of a Qubit in a Molecule*, Phys. Rev. X **10**, 031050 (2020).

[94] A. L. Grimsmo, J. Combes, and B. Q. Baragiola, *Quantum Computing with Rotation-Symmetric Bosonic Codes*, Phys. Rev. X **10**, 011058 (2020).

DOI: 10.17185/duepublico/78528
URN: urn:nbn:de:hbz:465-20230705-174716-0